A METHOD FOR ASSESSING THE TRIBOLOGICAL PERFORMANCE OF TOOL AND WORKPIECE INTERACTIONS

A METHOD FOR ASSESSING TRIBOLOGICAL PERFORMANCE OF TOOL AND WORKPIECE INTERACTIONS

By

ALI ALIAKBARI KHOEI, B. Sc.

(McMaster University, Canada)

A Thesis

Submitted to the School of Graduate Studies

in Partial Fulfilment of the Requirements

for the Degree

Master of Applied Science

McMaster University

MASTER OF APPLIED SCIENCE (2019) McMaster University

(Mechanical Engineering) Hamilton, Ontario

TITLE: A METHOD FOR ASSESSING TRIBOLOGICAL PERFORMANCE OF TOOL AND WORKPIECE INTERACTIONS

AUTHOR: Ali Aliakbari Khoei

SUPERVISOR: Dr. Stephen Veldhuis

Department of Mechanical Engineering

McMaster University

NUMBER OF PAGES: xv, 149

Abstract

Friction in machining is a complex phenomenon that can directly affect cutting productivity and product quality. Currently, different coatings are developed for machining applications which can increase tool life in the machining processes. Since performing a real machining test to quantify the friction is expensive and time-consuming, developing a bench scale testing method to simulate the friction in machining can reduce the cost and help researchers and industries select a suitable coating for their specific applications.

The goal of this work was to study the adhesion between the tool and workpiece material under machining conditions by simulating them using a heavy-load high-temperature tribometer. A high normal load was applied to plastically deform the workpiece material. The contact zone was then heated up using a resistance heating method. The normal load should be in the range that can generate a plastic flow on the surface of the workpiece material prior to seizure.

Three groups of in-house coatings were tested to study the effects of coating deposition parameters on the coefficient of friction. The results of these tests showed that the coating with the lowest bias voltage and highest Nitrogen pressure had the best tribological performance.

As a next step, three different commercial coatings were selected. Super duplex stainless steel was chosen as the workpiece material and the tribometer tests were performed. To validate the tribometer results real machining tests and tool wear analysis were performed. AlTiNOS+ WC/C was observed to be a lubricious coating which reduced the cutting force and coefficient of friction during the running-in stage. However, the low

hardness of the coating provided little abrasion resistance and was removed after the first pass. AlTiNOS+ TiB2 demonstrated a good combination of hardness and lubricity associated with improved coating tribological performance as well as

wear resistance.

To my parents, who gave

me the opportunity to learn and live life.

Acknowledgments

I would like to express my gratitude to my thesis supervisor Dr. Veldhuis for his useful suggestions and kind support. Thank you for trusting me during this two-year journey and providing me with such a unique learning opportunity in MMRI.

I give thanks to Dr. German Fox-Rabinovich, Dr. Jose De Paiva and Dr. Abul Arif who provided me with valuable comments regarding coating selection, machining tests and the thesis writing.

Many thanks to the whole MMRI team notably Mr. Terry Wagg, Mr. Brady Semple, Dr. Julia Dosbaeva, Dr. Bipasha Bose and Mr. Simon Oomen-Hurst for sharing their experience and knowledge with me and offering me their technical feedback.

I also want to thank all the MMRI graduate students especially Mr. Jeremy Boyd and Mr. Farhad Molaiekiya for sharing their ideas and their assistance during my studies.

Lastly, the author wishes to acknowledge the support for this research provided by Natural Sciences and Engineering Research Council of Canada (NSERC) under the CANRIMT Strategic Research Network Grant NETGP 479639-15.

Table of Contents

List of Figures

List of Tables

List of all Abbreviations and Symbols

BEC- Backscattered electron composition

BUE- Built-up edge

Co- Cobalt

EDS- Energy dispersive spectroscopy

ISO- International standards organization

MMRI- McMaster manufacturing research institute

Ra- Roughness average

Rq- Root-mean-square average roughness

Sa- Average height of the selected area

SEM- Scanning electron microscopy

WC- Tungsten carbide

COF- Coefficient of friction

σ- Normal stress

τ- Shear stress

A_A- Apparent area of contact

A_r- Real area of contact

φ- Shear angle

r- Chip thickness ratio

ζ- External friction threshold

H- Brinell hardness value

μ- Coefficient of friction

N- Normal load

α- Rake angle

P- Normal force

Q- Tangential force

h- Depth of imprint

r- Imprint diameter

R- Pin diameter

F_P , F_Q- Cutting forces.

F_C- Force in direction of the chip

N_C- Force perpendicular to the chip.

F_S- Force in direction of the shear plane.

N_S- Force perpendicular to the shear plane.

t- Uncut chip thickness

t_c- Chip thickness

b- Width of cut

l- Length of cut

l_c- Tool chip contact length

σ_c- Normal stress on chip

τ_c- Shear stress on chip

V_C– Chip velocity

m- Shear friction factor

k- Shear flow strength of the workpiece material

μ_a- Coefficient of adhesion friction

τ_{Ave}- Average shear stress on the pin tip

M- Reaction torque value

R'- Imprint diameter

HRC- Hardness in Rockwell C

1 Introduction

1.1 Background

Metal cutting is one of the most important manufacturing processes in which unwanted material is being removed from the bulk of metal in the form of chips. In this process, a sharp, hard tool moves relative to a workpiece material creating plastic deformation in the workpiece. The tool shears a layer of the material and following severe plastic deformation, the layer will separate from the bulk material. This process usually occurs under severe conditions. The stresses are usually high 2-3GPa and the temperature can exceed 1000˚C due to severe plastic deformation and high level of friction present in the cutting zone. To better understand the interaction of materials in the cutting zone this research took a tribological based approach.

Tribology is the science of interacting surfaces which are moving relative to each other. Friction, wear and lubrication are the most important phenomena in tribology. As was mentioned, the cutting tool and workpiece material move relative to each other during machining, causing the contact zone between them to wear, which over time leads to tool failure.

1.2 Motivation

Obtaining a deep understanding of the friction in the contact zone and wear mechanisms between the tool and workpiece material is valuable since it may grant the ability to control friction and wear on the tool. Less friction and a longer tool life are two possible direct outcomes of studying the tribological aspects of machining. Longer tool life would decrease tool usage and also reduce machining downtime associated with replacing the tool. As such, the productivity would be raised and the process would be rendered more economically efficient. In addition, less friction on the tool would decrease the tool wear, consequently improving the part quality and surface finish. Moreover, less friction would make it possible to benefit from a higher material removal rate (MRR) during machining, which would also raise productivity. Dry machining and the use of fewer lubricants is the other advantage of friction reduction through tool material selection during machining, in addition to being more environmentally friendly due to reduce refining and disposal issues.

Extensive machining trials performed on expensive materials are generally required to study the tribological behaviour of the material and coating performance during the machining of different workpiece materials. Also, machining by itself doesn't provide detailed information regarding the contact zone between the cutting tool and the chip which has a significant effect on the tool wear mechanism. Therefore, finding a way to quantify and understand the tool-chip interface is very important. The heavy-load high-temperature tribometer at the Mcmaster Manufacturing Research Institute makes it possible to investigate the contact zone between the cutting tool and the workpiece material and quantify the behaviour of each coating in contact with different materials under conditions similar to the machining process.

This thesis provides the background needed to improve the performance of the heavy-load high-temperature tribometer to enable it to obtain a better understanding of what goes on at the contact zone during machining and to measure the coefficient of friction (COF) between pairs of materials. Specifically, assessing the COF being measured by the tribometer test and associating it to the tool performance in machining is the fundamental question addressed in this study. Since friction on the cutting tool is a complex phenomenon, measuring it poses a challenge. Sliding and sticking regions are two different areas on the tool which interact with the workpiece material in completely different ways. Measuring the coefficient of friction between a pair of materials using a heavy-load high-temperature tribometer requires a deep understanding of friction during the machining process as well as the working of the tribometer itself. Measuring material flow within the workpiece material during a tribometer test was one of the main problems with isolating the surface COF values needed to assess a material interaction. This research addresses this by establishing the tribometer parameters, specifically load, needed to measure the COF at the surfaces of the materials under study.

1.3 Research Objective

As mentioned, friction plays an important role in the machining process. Having a deep understanding of the tribological behaviour of cutting tools and coatings with respect to different workpiece materials is thus crucial for researchers since it can directly affect the productivity and efficiency of the machining process. To this end, quantifying the frictional properties of cutting tools under various temperatures is needed to assess their performance during machining. Measuring the coefficient of friction at different temperatures is a means to compare the tribological performance of the coatings and the cutting tools. Quantifying the tool coefficient of friction using a heavy-load high-temperature tribometer is the chief goal of this project. Since friction during machining is complex, it is necessary to define the type of coefficient of friction to be measured. Based on the literature there are two main areas on the cutting tool: the sticking and the sliding regions. The COF measured during machining with a dynamometer is the average COF of both these areas and also includes aspects associated with the cutting edge. The objective of the current study was to develop an express method to model the friction phenomenon that can yield reliable data regarding the machining contact zone. To assess the tribological performance of the coatings, additional tests were performed on different coating pairs and workpiece materials. Measured values of the tribometer were validated with the help of the actual machining process.

The following points briefly describe the research objective:

1. **Investigating the performance of a heavy-load high-temperature tribometer**

To ensure the reliability of the tribometer, the resulting data was compared with benchmark results generated by another researcher [1]. The effects of changing different tribometer testing parameters on the reliability of the results was investigated. In order to explain the effects of the testing parameters on the results the mechanics and physics of the tribometer were studied.

2. **Correlating the machining process to the tribometer test**

Obtaining a clear physical understanding of friction in machining and understanding the role of heat during the process will enable more accurate results to be gained from the tribometer. Tribometer results were then validated using machining tests and process performance analysis was done to analyze the tribological behaviour of the coatings**.**

3. **Perform tribometer tests on different in-house and commercial coatings to evaluate the tribological performance of coatings**

The performance of 3 different coatings were investigated for machining super duplex stainless steel with the corresponding results and behavior being recorded. Additionally, in-house coatings with different deposition parameters and chemical compositions were analyzed and their tribological behaviour under contact with super duplex stainless steel were quantified.

1.4 Organization of thesis

The chapters of this thesis are organized based on research objectives and the studies undertaken. As mentioned before, the primary goal was to understand the contact principles and the friction phenomenon during machining. To this end, chapter 2 presents a review of friction basics and recent work concerning the measurement of friction coefficient in the machining process. Next, the experimental setup and the physics and tribometer mechanics are described. Chapter 4 focuses on experiments performed with the tribometer to find a way to get more precise readings. In chapter 5 the conditions and results of the machining tests are outlined with the results used to validate the measured values from the tribometer. Chapter 6 briefly outlines the conclusions of this study. Chapter 7 provides recommendations for future work and areas for potential improvements that can be made to the system to further improve its performance.

2 Literature Review

2.1 Contact and surface interactions

For two bodies in contact, the interaction between them is defined by the characteristics of the surfaces. Each contact has a mechanical and physical-chemical aspect. The mechanical aspect of the contact encompasses a stress and strain field in the contact zone. Physical and chemical bonding occurs when the materials are in contact [2]. Bodies in contact transfer mechanical stresses, heat and electricity. In addition, contact can generate barrier layers that seal the material and stop its flow [3]. Contact between two surfaces can happen at different scales. An example of a large scale contact is a rail-wheel whereas an Atomic Force Microscopy's pin touching the material's surface takes place at the nano-scale. Surfaces are not perfectly flat. To address this Rabinowics [4] defines roughness as a deviation from the reference point, the distance between regions varies during contact. In the areas which are close to each other atomic forces will be activated and atoms will be in contact. These regions with atomic contacts will be defined as "junctions". The real area of contact (Ar) is the summation of the junctions. The apparent area of contact (Aa) is the total area consisting of the regions in contact as well as regions which are far from each other [4].

2.1.1 Real Area of contact

Since most interactions occur within the real area of contact it is important to first determine its size. Figure 2-1 shows the real and nominal areas of contact.

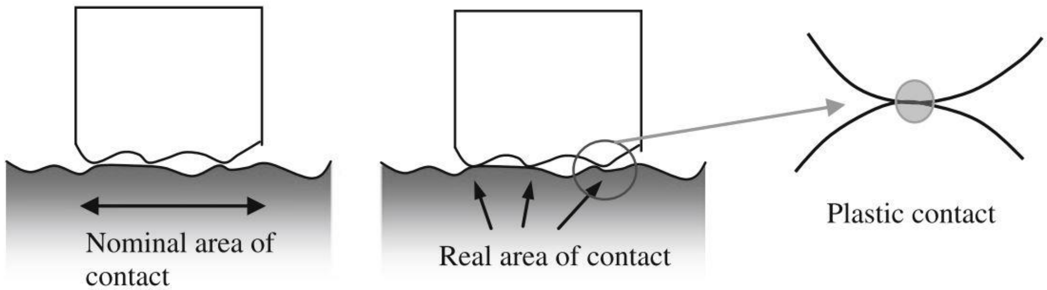

Figure 2-1- The real and nominal area of contact [2]**.**

The real area of contact is the sum of the areas which are in contact:

$$A_r = \sum_{i=1}^{N} A_i \qquad (2\text{-}1)$$

In equation 2-1, N is the number of junctions between the two bodies [2]. When two surfaces are in contact and a normal load is applied, the asperities can be deformed either plastically, elastically or by a mixture of the two. The asperities first begin to deform elastically. The increasing load will deform the asperities plastically and deformation will continue until the real area of contact can balance the normal load.

Rabinovicz [4] reported that the real area of contact is always larger than the ratio of the normal load F_N to the value of Brinell hardness of the softer material [4].

$$A_r \geq \frac{F_N}{H} \qquad (2\text{-}2)$$

In equation 2-2, F_N is the normal force and H is the Brinell hardness value of the material.

It is also mentioned that in the majority of surfaces, A_r is equal to F_N/H. But if we have surfaces which are highly polished and have small asperities, they won't plastically deform when they come in contact with other surfaces and the real area of contact will be greater than F_N/H. Also, if shear forces are added to normal forces the materials will have tangential motion. Therefore, the real area of contact will be greater than the value of $\frac{F_N}{H}$.

The apparent area of contact A_A is the area that can be seen when two surfaces are in contact. In fact, the real area of contact is always a fraction of the apparent area of contact and the following inequality is always true for any kind of contact:

$$0 < \frac{A_r}{A_A} \leq 1 \qquad (2\text{-}3)$$

When two surfaces are in contact under a light load or when they are extremely rough, the ratio of the real contact area to the apparent area is very small. Because surfaces contact in very small areas the stress on the small points is higher than the apparent normal stress. As a result, asperities are deformed and cause the real area of contact to increase. This will reduce the normal stress in the contact zone. If the load is high enough, the ratio of the real area of contact to the apparent area of contact will reach one, which means all the asperities are flattened and seizure has occurred. It this case, the normal load has a minimum effect on the friction. Shaw [5] has divided all friction systems into two general regimes: lightly loaded sliders (LLS) and heavily loaded sliders (HLS). Bowden and Tabor [6] described how two surfaces behave when they are in contact under a heavy load. Their study had two main assumptions. First, it was assumed that the asperities were spherical. Second, that one of the surfaces is softer than the other and the softer asperity will plastically deform. The plastic deformation of the softer asperity will continue until the load is supported by the softer material. Bowden [6] mentioned that increasing the normal load will lead to a uniform compressive stress on the asperity interface, the value of which is about 3 times that of the yield stress of the softer material. This study [6] has shown that the value of the normal stress just below the surface of the softer material is equal to the yield stress. Under this condition, the real area of contact is equal to the apparent area of contact. Bowden and Tabor's study shows that this behaviour is insensitive to the material and the size of the samples. The stress in the interface won't exceed $3\sigma_Y$. Based on this study, the stress is expected to be $3\sigma_Y$ on the interfaces and since many types of engineering materials have a yield stress between 0.3 to 1 GPa, the normal stress in the heavily loaded systems will likely be between 1 to 3 GPa. This interval will be used in calculations concerning the mechanics of the tribometer discussed later in chapter 3. Figure 2-2 shows the results of Bowden and Tabor's study of the interacting surfaces under heavy load.

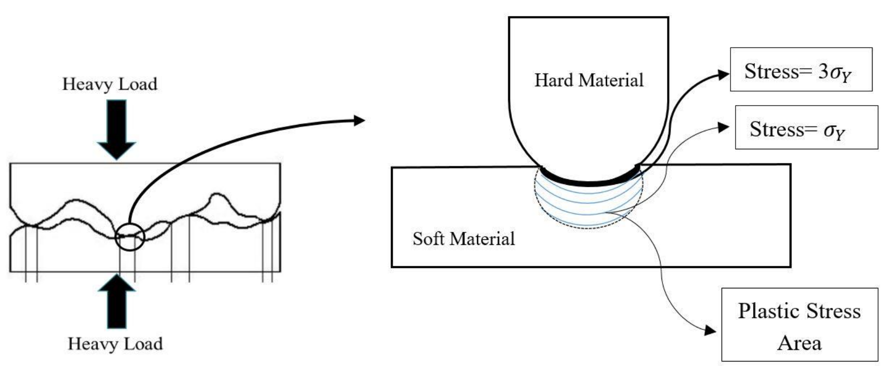

Figure 2-2- Normal stress in the interface of the heavily loaded system.

It is assumed that plastic deformation is taking place on the interface of the contact [4] so the minimum value of the real area of the contact is [4]:

$$A_{R.min} = \frac{F_N}{H} = \frac{F_N}{3\sigma_Y} \qquad (2\text{-}4)$$

In equation 2-4 F_N is the normal load and H is the indentation hardness in Pascal. The material will plastically deform if we apply a normal load equal to the yield stress of the material. Thus, for heavily loaded sliders the minimum ratio of the real area of contact to the apparent area is at least $\frac{1}{3}$:

$$\frac{A_r}{A_A} = \frac{\sigma_Y}{3\sigma_Y} = \frac{1}{3} \qquad (2\text{-}5)$$

Therefore, for any tribological system, if the ratio of the real area of contact to the apparent area is less than $\frac{1}{3}$ the system can be considered as lightly loaded. Tribological systems with the ratio of $\frac{A_r}{A_A}$ more than $\frac{1}{3}$ can be considered as highly loaded. Based on this study, it can be concluded that not all of the heavily loaded systems undergo seizure and internal shear since the plastic flow of the material begins when the ratio of $\frac{A_r}{A_A}$ is $\frac{1}{3}$ but as normal load increases, it approaches 1. When the ratio reaches 1, seizure will occur along with internal shearing of the softer material.

2.2 Friction

Friction is the resistance to tangential motion when two surfaces are under a normal load. There are two types of friction forces: static and dynamic. When two surfaces are moving relative to each other with a given sliding speed the friction force that resists in the opposite direction of the motion is called the dynamic friction force, F_f. Therefore, the ratio of $\frac{F_f}{F_N} = \mu$ is the coefficient of dynamic friction. The friction force which resists the motion prior to the sliding speed is known as the static friction force. Figure 2-3 shows the schematic of contact. μ_s is the coefficient of static friction.

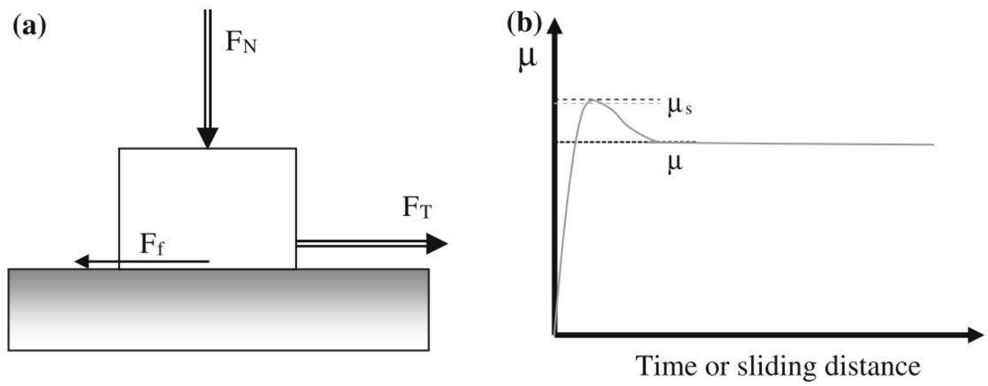

Figure 2-3- Schematic of contact with forces.

When two surfaces are pressed against each other with a normal load, a tensile normal force is needed to separate the surfaces. In fact, adhesive bonds form after the surfaces press together and as a result, a normal load in the other direction is needed to shear the bonds. A coefficient of adhesion is the ratio of the normal tensile force ($F_{N'}$) which is needed to separate the surfaces to the normal load which is applied first.

$$f' = \frac{F_{N'}}{F_N} \tag{2-6}$$

Rabinowicz [4] noted that 90% of the friction force is used in breaking the adhesive bonds between atoms of the two surfaces. The electrical effect, surface asperities and ploughing are other phenomena which play a role in friction force formation. He also noted that oxide layers, surface contamination, a small real area of contact and elastic residual stress on the surface can contribute to avoiding adhesive bond formation. Moreover, shear forces between the two surfaces along with relative motion, would break oxide and contamination layers on the surface of the materials. As a result, the real area of contact would increase and adhesive bonds can be formed [4].

2.2.1 History of contact mechanics and friction

Generally, theories about contact and friction can be divided into four main groups.

The first scientific conception of friction was developed at the end of the seventeenth century when the mechanics of rigid bodies were beginning to be studied. In this theory, researchers assumed that the solids were perfectly rigid and defined friction as a force which emerges from the rubbing of rigid asperities. Friction was just a function of the geometry of the asperities since there was no other parameter that could affect friction due to the assumption of perfect rigidity of the solids [7].

The second group of ideas described friction based on molecular attraction between two surfaces. In fact, they were defining friction as the force needed to break the molecular attraction bond. The molecular theory was first proposed by English physicist Desagulier (1734) [7]. The theory of friction formulated by Bowden and Tabor [6] can be also included in this group. Bowden and Tabor proposed that molecular interactions between surfaces can weld junctions in the contact point and that friction is a force needed to overcome welded junctions between solids [6]. Based on molecular theory, Kuznetsov [8] described friction as the work required to form new surfaces.

The third group of theories characterizes friction as a phenomenon caused by the deformation of a softer material that is penetrated by a harder material [7]. An English physicist Leslie (1801) proposed that friction arises from a wave of deformation in front of penetrating asperities. A German researcher Gumbel came up with a new definition of friction defined as the resistance to motion being produced by the movement of the material in front of the penetrating asperities [7].

The fourth group combined the two theories of friction. Among the scientists in this group, Coulomb (1779) was the first to propose that friction caused by interlocking asperities as well as lifting asperities over each other. Another important theory proposed by Ernst and Merchant [9] in 1940 was the Molecular - Mechanical theory of friction. This theory describes friction as a phenomenon which is caused by the attraction between molecules of the material - adhesion- and interaction and interlocking of asperities on the surface of the material.

Generally, deriving the coefficient of friction depends on three frequently interdependent factors: the pair of materials which are in contact, the design of contact and geometry of the surfaces and the local operating conditions which can change the material and geometry of the contact.

2.2.2 Mechanisms of friction

As mentioned previously, 90% of the friction force comes from adhesive bonds on the contact zone. When a normal load is applied on two surfaces, the atoms of each material interact in the real area of contact. The attraction between these atoms forms adhesion bonds. Adhesion can happen at a low or high temperature. Metals like aluminum can stick to each other even at a low temperature.

The major cause of friction is the resistance of the welded junctions to the motion. However, the abrasion between asperities, the roughness of the surfaces and the electrical effect can change the friction force.

$$F_F = F_{Adhesion} + F_{Abrasion} + F_{Roughness} + F_{Electrical} \tag{2-7}$$

Roughness and abrasion terms can be effective during contact of very rough surfaces or materials which have hard inclusions.

The earliest concept of friction between two sliding surfaces was characterized by adhesion between the asperities of the surfaces. Bowden & Tabor [6], who developed this idea, proposed that when two asperities are pressed against each other, they will weld together as a result of adhesion between the two surfaces. Tangential movement of the surfaces will break the adhesion bonds, causing friction in the interface due to the shear strength of the material. Bowden and Tabor [6] also added that harder asperities can penetrate the softer ones and cause plastic deformation by making grooves in the softer surface. The second idea that they introduced was ploughing, which can create resistance to the motion and cause frictional force. The adhesion theory proposed by Bowden and Tabor suffered from a set of drawbacks [10] such as:

- Surface roughness was not considered in the adhesion theory.
- Experimental results are not confirming the theoretical results.
- The adhesion cannot be observed when the normal load is removed.

To address the limitations of existing adhesion theory Rabinowicz [4] suggested considering the roughness angle of the surfaces and radius of the asperities.

Kragelsky [7] developed a molecular - mechanical theory. In his book, he used the word “molecular” to describe the adhesion between the surfaces. The word “mechanical” stands for the plastic deformation of material during the contact. He explained that friction has a dual nature and in addition to the adhesion, friction can arise from the shearing of material under the surface.

Other researchers focused more on the effect of plastic deformation in friction. Green [11] investigated the effect of asperity plastic deformation on the friction. His work was extended by Edward and Halling [12]. They proposed that plastic deformation of asperities causes resistance to motion and the work which is needed to deform the asperities is equal to the resistant force of motion for a certain distance.

Later on, Heilmann and Rigney [13] developed expressions for the coefficient of friction which depended on mechanical properties and microstructural parameters of materials. They proposed an energy-based model based on the assumption that the frictional work is equal to the work of the plastic deformation during a steady-state sliding test [12].

2.2.3 Sliding friction

The nature and the causes of friction were discussed with friction described as a force which resists tangential motion. However, it’s necessary to understand the difference between two situations. The first situation is when the forces are insufficient to cause motion. The second is when the forces are sufficient to cause sliding motion between two surfaces.

Figure 2-4 shows the schematic of the load on a surface with small force T. If small force T is applied, the motion won't occur. In this case, the friction force at the contact zone between two surfaces would be equal to T in the opposite direction. If the force T decreases, the friction force also would decrease.

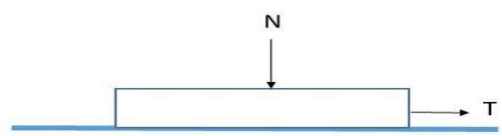

Figure 2-4- Schematic for a normal load on the surface with small tangential force T.

The next situation prevails when the force T is big enough to move the weight. In this case, the mass of material would move in the direction of the T and the value of the friction force would be less than T.

There are three rules to determine the friction force as a function of the applied load, the size of the area of the contact and the sliding velocity:

1- The friction force F is the function of the normal load N. The coefficient of friction (μ) is the parameter which relates these two together:

$$F = \mu N \qquad (2\text{-}8)$$

2- The size of the materials doesn't alter the friction force. In fact, the coefficient of friction is the same for a pair of materials and surfaces with the same material but different sizes.

3- The friction force is independent of the sliding velocity (v). Literature shows that the first two laws clearly apply in most cases. However, there are some exceptions but those exceptions are in extreme cases. But for the third law, it has been shown that the static friction coefficient is a function of time of contact and the kinetic friction coefficient generally has a positive slope at a slow sliding speed and negative slope at a high sliding speed. The magnitudes of these slopes are very small and reveal that the coefficient of friction changes by only a few percent during sliding. Figure 2-5 shows the positive slope in the low sliding speed and the negative slope in the high sliding speed for the two pairs of materials.

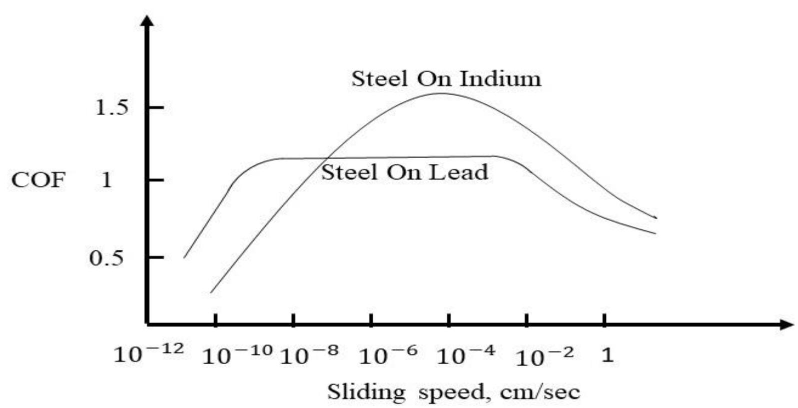

Figure 2-5- Friction- velocity graph with the positive slope in the low speed and negative slope at the high speed[3]**.**

2.2.4 The dual nature of friction

As stated before, contact between two surfaces occurs at several points and the total area engaged is termed as the real area of contact. In addition to the asperities which are in contact, the material that is close to the asperities would be affected by interactions of the asperities. Breaking junctions and making new contacts will deform the material that is under the contact points. Therefore, the material usually deviates from its initial condition. Friction bonds are contact points which form, persist and become destroyed under the action of normal and tangential loads [7]. To analyze friction, it's necessary to understand the difference between three successive stages:

1- The formation of frictional bonds due to surface interaction.

2- The existence of frictional bonds which can be distinguished by changes on the contacting surfaces. Sliding will generate temperature and deformation on the surfaces and therefore, the contacting surfaces will change.

3- The destruction of the friction bonds which will damage the surface.

Based on the aforementioned details regarding friction bonds, it can be concluded that friction has a dual, molecular - mechanical nature. Interaction between adhesive bonds caused by molecular attraction force is defined as a molecular part of friction. Bulk deformation because of the effect of the temperature and interaction between welded junctions is known as the mechanical aspect of friction. Because the surfaces are wavy and rough and the mechanical properties of the material are inhomogeneous, the harder material will penetrate to the softer material. The tangential displacement of the harder material in the softer material will deform the underlying surface.

2.2.5 Departures from conditions of plastic displacement

Plastic deformation happens when material flows around the asperities without separating from the bulk [7]. When a hard spherical tip presses against a disk material, the movement of the material relative to the indenter will gradually slow down and the material will shear or pile up around the indenter. If the pin is pressed against the disk and moved in the tangential direction, there would be a deformed element, E, on the pin tip which will experience the normal force, P, and the tangential force Q. The normal reaction force N will be perpendicular to the surface of the element and frictional force will be μN. Figure 2-6 shows the schematic view of the indenter and the element [7].

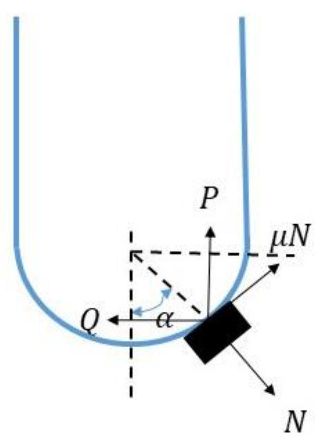

Figure 2-6- Forces for an element on the pin tip.

In order to obtain equilibrium on the deformed element, the following must be true:

$$\mu N = Q \cos\alpha - P \sin\alpha \qquad (2\text{-}9)$$

$$N = Q \sin\alpha + P \cos\alpha \qquad (2\text{-}10)$$

If the tangential friction force is greater than the other forces in the tangential direction, there would be no movement of the element relative to the indenter. As a result, the element would stick to the pin tip and movement will either stop or the material will pile up around the imprint [7]. The following equation describes this situation:

$$\mu N > Q \cos\alpha - P \sin\alpha \qquad (2\text{-}11)$$

To determine the condition of seizure, it's necessary to define the depth of penetration and find the relation between the forces. Figure 2-7 shows the depth of penetration (h) of a spherical indenter, sphere diameter (R) and indentation diameter(r).

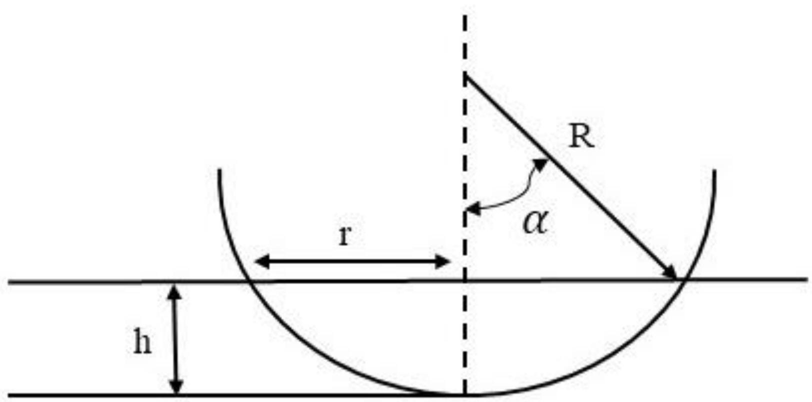

Figure 2-7- Schematic of a pin penetrating to a disk.

Based on Figure 2-7, the depth of penetration can be calculated using the diameter of the sphere:

$$h = R(1 - \cos\alpha) \qquad (2\text{-}12)$$

Dividing equations (2-10) and (2-11) will result in equation (2-14):

$$\tan\alpha = \frac{Q - \mu P}{\mu Q + P} \qquad (2\text{-}13)$$

Kragelsky [7] proposed that relative movement will cease when the following inequality is governing the tribological system:

$$h > R\,(1 - \cos\alpha) \qquad 2\text{-}14)$$

This means the material is plastically deformed and piled up in front of the pin.

From mathematics we know:

$$\cos\alpha = \frac{1}{\sqrt{1 + tan^2\alpha}}$$

Using equations 2-14 and 2-15 and substituting these two:

$$h > R\,(1 - \frac{\mu Q + P}{\sqrt{(Q^2 + P^2)(1 + \mu^2)}}) \qquad (2\text{-}15)$$

Equation (2-16) relates the depth of penetration corresponding to the tribo-system's transition to the shear and seizure stage [7]. The depth of penetration depends on the normal load, the shear force, pin geometry and the molecular friction between the two surfaces. Since the material will shear under the aforementioned conditions, the stress on the element will be equal to the yield stress of the material (σ_Y). As a result $P = C_1\sigma_s$ and $Q = C_2\sigma_s$. $C_1\ and\ C_2$ are a function of the pin geometry and the work-hardening of the material.

Putting the coefficients in equation 2-16:

$$h > R\left(1 - \frac{\mu C_2 + C_1}{\sqrt{\left({C_1}^2 + {C_2}^2\right)(1 + \mu^2)}}\right) \tag{2-16}$$

If the indenter is very flat and the pin tip is part of a very big sphere, then the h/r ratio will be close to 0. Therefore, μ will be a number very close to 1.

2.3 Metal cutting principles

Metal cutting is one of the most important processes in manufacturing. Removing materials in the shape of chips makes up the final part of machining. In fact, the workpiece material plastically shears during machining. Generally, plastic deformation occurs in three major areas: The primary shear zone on the shear plane of the workpiece material, the secondary shear zone on the chip and rake interface, and the third area which has plastic deformation on the flank face of the tool. This area is called the rubbing zone [5]. Figure 2-8 shows the different areas during the machining process.

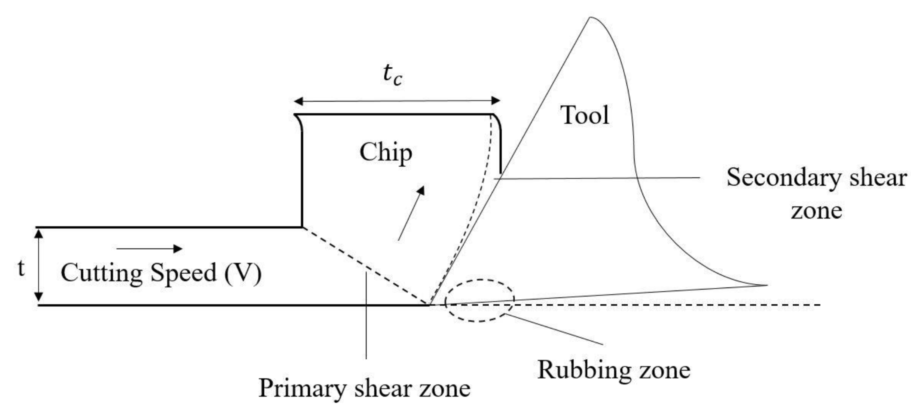

Figure 2-8- Deformation areas in the cutting process.

2.3.1 Forces and stresses in machining

Merchant (1945) proposed a force model for the metal cutting process which is widely being used. He assumed that the workpiece material shears along the plane with the angle of φ from the surface of the workpiece. In this model, the chip slides over the rake face with constant friction. This model is based on the vertical and horizontal forces which are experimentally obtained from the machining process. Figure 2-9 illustrates forces acting on the cutting tool, the chip and the shear plane [5].

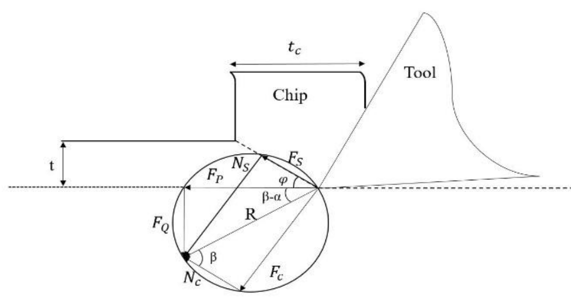

Figure 2-9- Forces acting on the hip and shear plan.

The forces on the tool face and shear angle are separated as shown in the following figure. Figure (a) shows the forces acting on the shear plane of the workpiece material (Fs and Ns) as well as the forces measured with a dynamometer (Fp and Fq) and the resultant force R’. figure (b) shows the forces on the tool face (Fc and Nc) with Fp and Fq repeated and R added to provide a reference between the two regions.

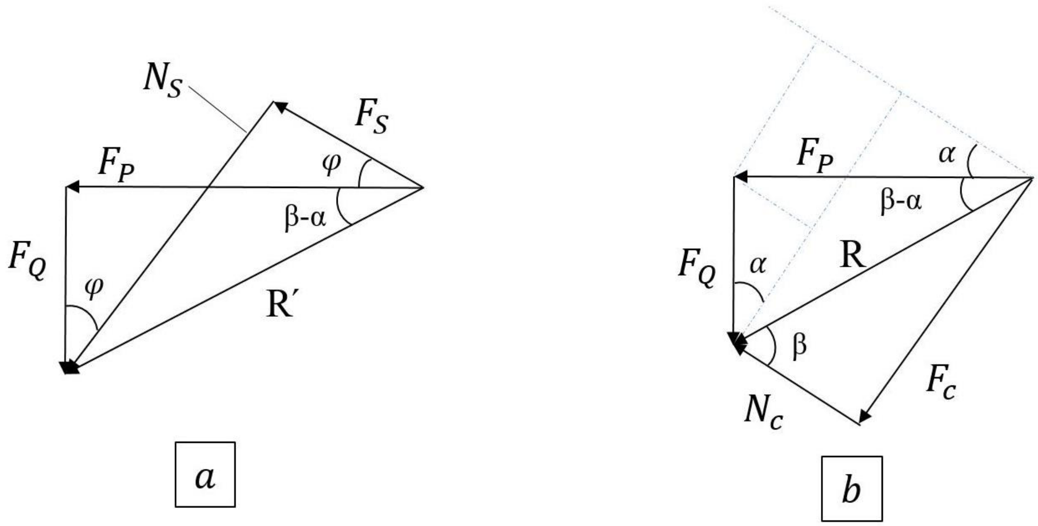

Figure 2-10- Forces acting on the a) shear plane, b) tool face.

Where:

- F_P and F_Q are cutting forces.
- F_C and N_C are forces in the direction and perpendicular to the chip.
- F_S and N_S are forces in the direction and perpendicular to the shear plane.
- φ is the shear angle.
- α is the rake angle of the tool.
- $R = R'$

From Figure 2-10 (a):

$$F_S = F_P \cos\varphi - F_Q \sin\varphi \tag{2-17}$$

$$N_S = F_Q \cos\varphi + F_P \sin\varphi = F_S \tan(\varphi + \beta - \alpha) \tag{2-18}$$

From Figure 2-10 (b):

$$F_C = F_P \sin\alpha + F_Q \cos\alpha \quad (2\text{-}19)$$

$$N_C = F_P \cos\varphi - F_Q \sin\varphi \quad (2\text{-}20)$$

In this model Merchant assumed that the coefficient of friction is constant along with the tool and it can be calculated from the forces on the tool face (b);

$$\mu = tan\,\beta = \frac{F_C}{N_C} = \frac{F_P \sin\alpha + F_Q \cos\alpha}{F_P \cos\alpha - F_Q \sin\alpha} \quad (2\text{-}21)$$

The chip thickness ratio (r) is the ratio of the uncut (t) to cut (t_C) chip thickness. Since the volume of the cut material is constant and the density of the material is not changing:

$$tbl = t_c b_c l_c \quad (2\text{-}22)$$

where t is the uncut chip thickness, b is the width of cut and l represents the length of cut. The letter C was used to correspond the parameters to the chip. Since the width of the chip is the same as the width of the workpiece material:

$$\frac{t}{t_c} = \frac{l_c}{l} = r \quad (2\text{-}23)$$

With the help of a geometrical calculation, the shear angle can be obtained from the following expression[5]:

$$\tan\varphi = \frac{r\cos\alpha}{1 - r\sin\alpha} \quad (2\text{-}24)$$

Also, the relative velocity of the chip to the tool can be calculated from the chip thickness ratio:

$$V_c = rV \quad (2\text{-}25)$$

Where V_c is the chip velocity, V is the cutting velocity and r is the chip thickness ratio.

As for the stresses on the rake face of the tool, Zorev [15] explained how the shear and normal stress changes on the tool tip. In the Zorev model, the rake face of the tool is divided into two main regions: the sticking zone which is closer to the tool tip and the sliding zone further from the tool tip. The stress distribution is different in these two zones. Figure 2-11 shows the normal and shear distributions on the rake face.

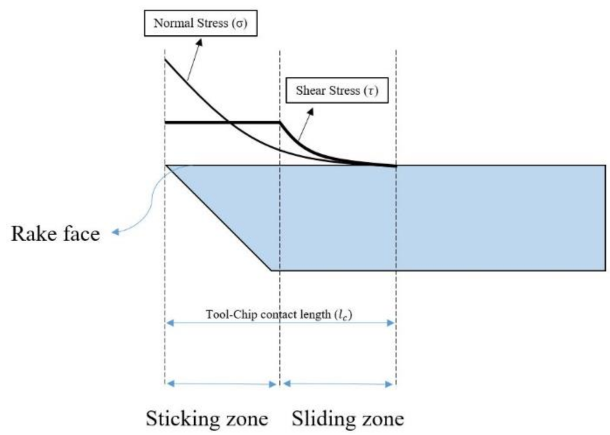

Figure 2-11- Stress distribution on the rake face.

As can be seen in Figure 2-11, normal and shear stresses are maximum on the tool tip. Further, from the tip, the normal stress decreases until reaching zero at the end of the tool-chip contact length. The shear stress is maximum and constant along the sticking zone and the value of shear stress is equal to the shear flow stress of the material. Shaw [5] mentioned that the combination of high normal and shear stress along with high temperature will cause the workpiece material to stick on the surface of the tool and workpiece material will plastically deform within the bulk.

2.3.2 Friction in machining

A review of all the models of frictional interactions helps to illustrate the interactions between the tool and the chip on the rake face.

As brought up earlier, Zorev developed a model of the average coefficient of friction on the tool face. Equation (2-21) yields the average coefficient of friction. Based on Zorev sticking-sliding models, the normal stress is maximum at the tool tip and drops to zero at the end of the tool-chip contact length. The distribution of the normal load on the tool face can be calculated using the following equation:

$$\sigma_c = \sigma_{c.max}\left(\frac{x}{l_c}\right)^n \qquad (2\text{-}26)$$

Where l_c is tool chip contact length, x is the distance from the chip separation point and n is an exponent parameter [16].

However, the relationship between normal and shear stress can be defined in the sliding zone using the Coulomb friction law based on the classic interpretation of friction:

$$\tau_c = \mu\sigma_c \qquad (2\text{-}27)$$

Since the ratio of the real contact area to the apparent contact area is very small in the sliding region, the Coulomb friction law can be used. However, this ratio for the sticking zone is very high and it reaches 1 close to the tool tip.

In 1988 Trent [17][18][19] published three papers in which the seizure phenomenon in machining was clearly illustrated. The reason for seizure in the sticking zone were explained, and a model for the movement of workpiece material over the tool face as well as one for the temperature distribution in machining were proposed [20][18][19].

Trent pointed out that severe conditions in the contact zone such as high stresses and temperatures and absence of interface barriers between the tool and workpiece material will cause seizure of the chip on the tool surface[20]. The velocity of the chip in the sliding region (V_c) can be derived from equation (2-25). However, the situation in the sticking zone is completely different. The velocity of the chip in the interface with the tool is zero [20]. Since the chip bulk velocity is V_c, there is a gradient of velocity on the chip from the tool face to the top surface of the chip. Due to high normal stress, the real area of contact on the tool and chip interface approaches the apparent area of contact. When the real area becomes equal to the apparent area seizure occurs and the surface of the chip sticks to the tool surface. An increasing load and the presence of shear will plastically deform the chip material. The chip sticks to the tool at the interface and the velocity is zero in that layer. Different layers of the chip thickness have different velocities ranging from zero to V_c. The following graph illustrates the velocity gradients within the chip thickness[5].

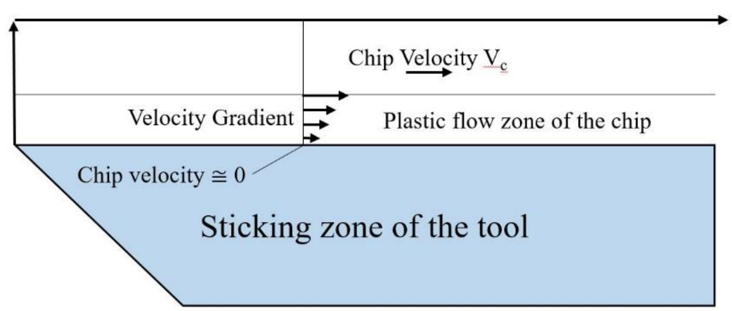

Figure 2-12- Chip velocity gradient in the sticking zone.

Trent mentioned that seizure and plastic deformation in the sticking zone can affect machining performance. At lower cutting speeds it can cause the formation of an adhered layer of strain hardened chip material, known as a built-up-edge (BUE) [19]. However, higher cutting speeds will generate more heat and higher temperatures on the tool face which will make material softening the dominant mechanism in the cutting process. Material softening will change the nature of the contact zone and instead of built-up-edge material, a thin layer of secondary shear zone "flow zone" will be in the contact zone [20]. It was also observed that the behavior of the flow zone can be very similar to that of very viscous liquid materials.

Shear stress on the interface is a fraction of the shear strength of the workpiece material which is calculated accordingly:

$$\tau = mk \tag{2-28}$$

where τ is the interfacial shear stress, m is the shear friction factor and k is the shear flow strength of the workpiece material. The value of m varies from 0.1 to 0.9 and if m=1.0 then the real area of contact is equal to the apparent area of contact resulting in seizure.

To assess friction stress, Shirakashi and Usui [21] used a split tool and perform machining tests on α-brass, pure aluminum, and S15C low carbon steel. They fitted a line on the data from their experiments and proposed an equation for the friction stress on the tool:

$$\tau_f = k(1 - e^{\frac{-\mu\sigma_n}{k}}) \tag{2-29}$$

where τ_f is the friction stress and σ_n is the normal stress on the tool face.

Based on the molecular-mechanical model of friction, friction consists of two main components. Molecular adhesion and plastic deformation directly affect the coefficient of friction[22]. Therefore:

$$\mu = \mu_a + \mu_m \tag{2-30}$$

Grzesik [23] applied the molecular-mechanical theory to calculate the shear strength of the local adhesive bonds and he derived μ_a and μ_m in machining. He mentioned that the shear strength of the adhesive bonds can be calculated using the following equation[23]:

$$\tau_a = 0.34\, L\rho \ln\left(\frac{\theta_m}{\theta}\right) \tag{2-31}$$

where: ρ is the density of the material, L is the specific heat of melting, θ_m is the melting point of the material and θ is the cutting temperature.

Therefore, the adhesion coefficient of friction is the ratio of the shear strength of the junction at the interface to the yield stress of the plastically deformed material:

$$\mu_a = \frac{\tau_a}{\sigma_Y} \tag{2-32}$$

Where τ_a is the shear stress at the interface and σ_Y is the yield stress of the deformed material. σ_Y can be calculated from the stress-strain curves.

To obtain the deformation term of the coefficient of friction Grzesik used Lee and Shaffer's model to derive the shear angle:

$$\varphi = \frac{\pi}{4} - \beta + \alpha \tag{2-33}$$

In this equation, φ is the shear angle, β is the friction angle and α is the rake angle of the tool.

The proposed expression for the plastic deformation of the coefficient of friction is [23]:

$$\mu_m = \tan^{-1}\beta = \tan^{-1}(\frac{\pi}{4} - \varphi + \alpha) \quad (2\text{-}34)$$

Zhou (2014) proposed a model with a transition zone in addition to the sticking and sliding zone. In it every region's performance was modeled separately and the local and global friction in the cutting process were calculated based on the thermomechanical analytical model. The analytical model results were compared and verified by experimental results. In this model the shear strain rate of the chip in different regions was used to calculate the chip velocity in all the zones. Finally, the friction in all regions was determined. The following graph shows Zhou's proposed model for different areas on the cutting edge [24].

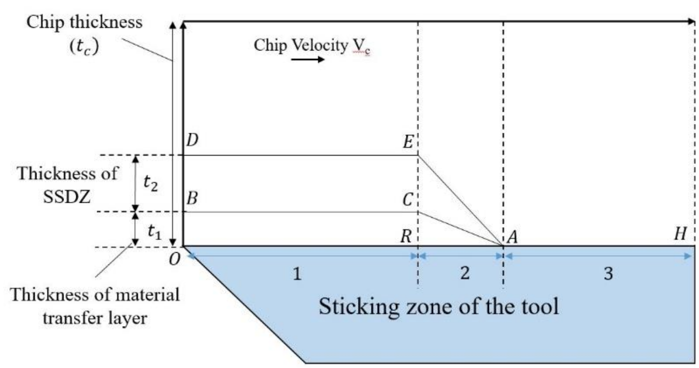

Figure 2-13- Sticking, transition and sticking zone in Zhou's model.

In this figure, the area bounded by ORAH is the tool-chip contacting interface and BCA is the cutting interface where the actual cutting is taking place. DEA defines the boundary of the secondary shear zone and t_2 shows the thickness of the secondary shear zone (SSDZ). BCARO illustrates the material transfer area and t_1 represents the thickness of this area. The material transfer layer is a thin layer of the chip between the interface in contact with the tool-chip contacting interface (ORAH) and the cutting interface (BCA). The velocity in this layer increases gradually until it reaches the chip velocity. This model can calculate the local and global shear strain, velocity, and the coefficient of friction.

2.4 Experimental approaches to quantify friction in machining

Generally, there are three different methods that can be used to quantify machining friction in [16]:

- Performing an actual machining test where the coefficient of friction is calculated from the machining forces.
- Using a conventional tribometer with light loads
- Using special tribometers which are specially designed to simulate machining conditions.

Use of cutting forces to determine the friction is a simple approach common in turning and milling processes. Cutting forces can be measured with a dynamometer and by analyzing the chips and tool-chip contact surface, the coefficient of friction can be obtained. This approach yields the average coefficient of friction along the cutting tool. However, as mentioned before because of changes in the normal and shear stress and temperature along the cutting zone local friction varies substantially. This method can’t determine the coefficient of friction for the sliding and sticking regions separately. One way to solve this problem is by using a split tool, but it is expensive and time consuming to set up the required machine and prepare the tool and workpiece material [16].

In the second approach, researchers used a conventional tribometer to evaluate the friction in machining. It was reported earlier that the tool always interacts with a fresh surface under very high stresses and temperatures. Unfortunately, conventional tribometers are not capable of duplicating the same tribological conditions experienced in machining. In a conventional tribometer like a pin-on-disk test, the pin does not encounter a fresh surface during the test and the normal and shear stress on the pin-tip are not in the range of machining stresses [16].

The third approach is to simulate the machining conditions on a tribometer. A group of researchers used a pin right after a cutting tool while they were cutting a tube of material. Olsson et al. [25] used this method to evaluate the coefficient of friction between high-speed steel (HSS) and a quenched and tempered steel AISI 4340. In his setup, a pin made of HSS was rubbed against a fresh surface of AISI 4340 with the same sliding speed and surface temperature. However, the problem with this setup was that the contact pressure between the pin and the workpiece material was about 15 MPa which was far away from the stresses present when machining AISI 4340 steel. Other researchers tried to overcome this problem and increase the contact pressure up to 3GPa [26]. But due to the work which is needed to set up the machine as well as machining expenses this approach is not widely being used in studies. Additionally, conducting tests with high sliding speeds is not possible because of the instability of the setup.

Claudin et al. installed a setup on a lathe machine in which a cylindrical pin rubs against the surface of a cylinder while it is rotating. The feed rate of the pin is very high and in this test it is rubbing a fresh surface in each test. In order to simulate machining conditions, a fresh surface should be generated on the workpiece by the cutting tool after each test to have a contact on a new and clean surface[27].

Biksa (2010) [28] developed a bench-scale tribometer in MMRI, a heavy-load high-temperature tribometer that can apply loads of up to 2000N and reach temperatures close to 900˚C. In this tribometer, a hard pin which represents a cutting tool is pressed against a disk that is made of the same material as the workpiece. The coefficient of friction is calculated based on the measured torque and the area of the contact. To assess the performance of the MMRI's tribometer, the components and mechanics of this tribometer must be known. In chapter 3, the mechanics of the heavy-load high-temperature tribometer will be discussed in detail.

3 Physics and mechanics of the heavy-load high-temperature tribometer

3.1 General view and operation of the MMRI tribometer

Friction in metal cutting is a complex process in which two surfaces interact under high stresses and elevated temperatures. To help with the experimental study of this phenomenon, testing conditions need to be as close as possible to the machining conditions. The MMRI heavy-load high-temperature tribometer was developed by Nanovea to generate conditions that simulate contact and friction in machining. Biksa (2010) [28] and Boyd (2012) [29] introduced some fundamental changes in hardware and software to a tribometer to improve its accuracy and ease of use. This part will describe the operation of the latest version of the MMRI tribometer. The following image shows the general view of the tribometer.

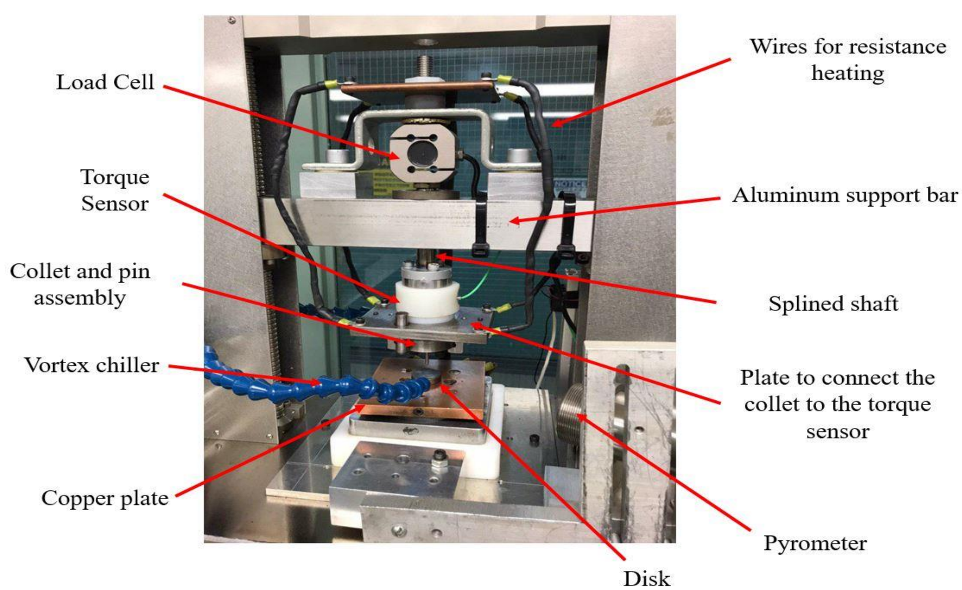

Figure 3-1- Overview of the MMRI tribometer.

In this tribometer, a pin made of the tool material is mounted in a collet, which in turn is aligned with a Kistler reaction torque sensor. A flat disk made of the workpiece material is placed on a copper plate, which is then connected to the spindle.

Since the pin and the disk are aligned the reaction torque will be very small. Therefore, a very precise and high-resolution reaction torque sensor is chosen. A Kistler Model 9329A torque sensor can measure torques in the range of +/-1 Nm with 0.000005 Nm resolution. A Kistler type 5010 charge amplifier is used to change the output signal from the piezoelectric (Coulomb) to a voltage reading. Temperatures higher than 80 ˚C may damage the sensor thus the sensor is isolated by a low thermally conductive material and cool air is blown over the region. The torque sensor is screwed to a mounting flange and the flange is press fit to a splined shaft to allow for linear up and down motion while restricting rotation.

The Nanovea supplied strain gauge based load cell is threaded to the other side of the splined shaft. The load cell can be used for loads between 0-3000N. The control system can control a+/-3N load in the range of 2000N [28]. The splined shaft is connected to the aluminum support bar and can freely move up and down with the support bar. The support bar is connected to a lead screw, which in turn is connected to a DC motor which drives the motion that generates the normal load.

The copper sample mounting plate can be rotated by a DC motor connected to the spindle under the plate. This way, the disk will be rotated around the spindle axis while the pin is stationary. Then, the torque required to rotate the pin on the disk is measured with the reaction torque sensor.

The pin disk interface is being heated up using the electrical resistance heating method. In this method, a welder with a maximum of 200 A is used to generate the current. The welder is carefully connected to the tribometer with large diameter cables and contacts to ensure that the highest resistance point is at the pin and disk contact point. The pin and disk are part of an electrical circuit and the current generated by the welder passes through the pin and disk, heating up the interface. The temperature is measured using an infrared pyrometer. The two-colour Optris CTlayser pyrometer with model number of LT-CF2 emits two beams which converge at a distance of 15 cm from the pyrometer to measure the temperature[28]. This pyrometer is capable of measuring temperatures in the range of -40 to 975 ˚C. The accuracy of the pyrometer is +/-1 ˚C and the resolution is 0.1 ˚C. Since the pyrometer's beam cannot reach the interface surface of the pin and disk, the temperature is being measured on the pin about 1 mm above the contact point. This means that the temperature measured is not at the contact point. There is no other simple way to measure the temperature at the interface without unduly effecting the interaction.

Two separate PID controllers are used to control the applied load and spindle speed as well as the current which is drawn to the pin/disk interface.

To perform a test with the MMRI tribometer, the disks should be ground and polished. The surfaces of the disks should be parallel. The pin should be mounted in the collet and aligned with the center of the spindle. The misalignment of the pin can't exceed 20 microns. The surface of the pin and disk need to be cleaned with ethanol to remove any oil contaminating the surface. Following the pin and disk preparation, each test is performed in the following sequence:

- Preload: The pin comes down to load the disk to the selected pre-load value. This is the first contact of the pin and disk and needs to reach a steady load on the interface. The preload duration is 30 seconds and the PID controllers try to keep the applied load in the range of -/+10 N around the preload set point.
- Heating: The DC welder begins generating the current and heats up the interface. The measured temperature increases until it reaches the set point. Heating up the interface will cause some fluctuation in the normal load as the material plastically deforms under the load and temperature. The controller adjusts the cross arm position while it tries to maintain the specified load. The heating will continue until the end of the test and the controller will keep the temperature in the range of -/+10˚C of that selected using the data collected by the pyrometer 1mm from the contact zone.
- Full load: The full load can be the same or different as the preload. While the full load is being applied, the temperature is maintained at the selected range.
- Spindle rotation: The spindle starts to rotate at the selected speed. The reaction torque is measured using a Kistler torque sensor and the normal load and temperature are in the specified range. The spindle rotates with a selected speed (Usually 2 RPM).

- End of the test: In this step, the load and heating system deactivate and the pin is retracted about 20 mm above the disk. All the data from the load cell, reaction torque sensor and pyrometer are saved.
- Data analysis and COF calculation: The average of the normal load and the torque in the last 30 seconds and the measured temperatures are saved after the test. The imprint size of the pin on the disk is then measured using an Alicona 3D measurement microscope. Using an average value of the normal load, torque and imprint diameter, the coefficient of friction can be calculated.

3.2 Physics and mechanics of the MMRI tribometer

The mechanics of the contact between the pin and disk should be investigated in detail to obtain a deep understanding of tribometer performance. In this part, the mechanics of the contact and stress distribution on the interface are studied in detail. The following section describes the operation of the tribometer.

3.2.1 Brinell and modified Brinell hardness test

In machining, there is a plastic flow of workpiece material in the contact zone and normal stress is in the range of 1-3 GPa. A Brinell hardness test generates high stresses on the interface, which will cause plastic deformation in the softer material. These basic characteristics of the Brinell test make it a good candidate to mimic the friction associated with machining.

In the Brinell test, the pin is composed of tungsten carbide whereas the workpiece is made of a softer material that is mounted perpendicular to the loading direction. In this test, the pin is loaded against the disk under a heavy load and after plastically deforming the surface, contact hardness can be calculated from a measurement of the area. Brinell hardness is the amount of normal load per unit area of the contact. The load is usually recorded in kilograms and area of the contact in square millimetres.

The contact is plastic-elastic contact with the normal stress maximum at the center of the pin and decreasing at the sides of the pin [5]. There is an area of plastically deformed workpiece material under the interface that is supported by an elastically deformed area of the workpiece material.

Based on ASTM (#E10-08), the Brinell hardness is derived from the following equation:

$$H = \frac{F}{A} = \frac{F}{\pi D h} \tag{3-1}$$

Where F is the normal load, D is the imprint diameter and h is the imprint height.

Based on the aforementioned ASTM standard, imprint diameter should be measured on the reference plane of the disk in at least 2 different places and the average value should be reported. The white light laser interferometer and 3D scan are the best methods to minimize the error in the imprint diameter's measurement.

It's not easy to measure the height of the imprint (h) with an optical microscope. However, it is possible to calculate the area of the contact using basic geometry without the need to obtain an accurate reading of the imprint's height. The following statement yields the value of the Brinell hardness without the height of the imprint needing to be specified [28]:

$$H = \frac{F}{A} = \frac{2F}{\pi D(D - \sqrt{D^2 - d^2})} \tag{3-2}$$

where d is the imprint diameter and D is the diameter of the pin.

Tribologists developed a modified Brinell hardness test to study friction in the interface under high stresses. In this test, after the specimen is loaded with a hard pin under a Brinell test condition, the pin or disk will rotate around the axis of the indenter. The coefficient of friction can then be computed from the recorded reaction torque caused by the interaction of the pin and disk. External heating can also be used to heat up the contact zone.

Shaw conducted a comprehensive study on the modified Brinell test. He used a hard ball and tried to simulate the seizure condition under a heavy load [30]. Other researchers followed up on Shaw's study and tried to measure friction under the high plastic flow of the workpiece material where the apparent area of the contact was not the same as the real area.

Shaw proposed three general regimes of friction which depend on the ratio of the real area to the apparent area of contact. Figure 3-2 illustrates three regimes of friction proposed by Shaw [30]. Region I is for lightly loaded sliders in which the coefficient of friction can be derived using classic friction theory. In this region friction is the ratio of the tangential force to the normal force.

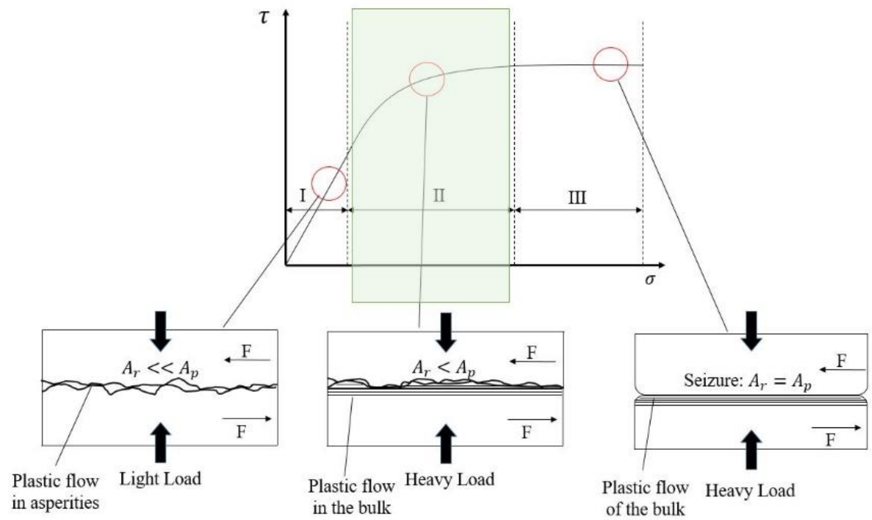

Figure 3-2- The three regimes of contact in solid friction.

Region III is for a condition in which the surfaces are heavily loaded. In this case, the real area of the contact is equal to the apparent area. Plastic deformation then occurs under the surface of the softer material. In this case, the shear on the interface is not a function of the normal stress and increasing normal stress does not change the shear stress. This case represents a complete seizure condition and will generate shear in the bulk material.

Region II is the intermediate area in which the bulk is plastically deformed but the ratio of the real to the apparent area of contact is less than 1. In this case, seizure does not occur, but the normal load deforms the bulk material. The normal stress on the interface is greater than the yield stress of the material. Based on equation (2-4) and (2-5), the minimum ratio of the real area to the apparent area of the contact is $\frac{1}{3}$ and the maximum normal stress will be less than $3\sigma_y$. Since the condition of this area has the greatest similarity to that of machining, it poses a major interest in this research. To quantify the machining friction, it's necessary to know the degree of plastic deformation in the specimen during external friction. In fact, the normal load will generate plastic deformation in the workpiece material and the rotation will shear the interface.

Shuster [31] used another setup to simulate machining friction. Shuster's setup works based on a modified Brinell test. However, his setup is capable of performing tests at high temperatures up to 1000 ˚C. The normal load can be increased to 5000 N, which can generate normal stresses in the range of 1-3 GPa. The pin is then rotated relative to the two disks perpendicular to the pin tip. The speed of rotation is 1 RPM and the machine can measure the coefficient of friction at different temperatures.

3.2.2 Shear and normal stress in MMRI tribometer

The MMRI tribometer works based on the principles of a modified Brinell test. Although similar to Shuster's design, there are some differences in the MMRI tribometer. To measure the coefficient of friction with the MMRI tribometer, both the distribution of the stresses on the interface and the method of COF computation need to be known.

To calculate the COF on the surface of the contact, it is assumed that each point on the contact surface experiences normal and shear stresses. The average value of the frictional shear stress of the interface is perpendicular to the normal load (F_n) and represented by τ_{ave}. If an infinitesimal area of contact is assumed on the interface the following equation can be written as:

$$dF_F = \tau_{ave} d_A \qquad (3\text{-}3)$$

The purpose of this expression is to calculate the average shear stress (τ_{ave}) and normal stress of the interface. Since a hemispherical pin tip is used in this test, the easiest way to calculate stresses is with a spherical coordinate system. The following image shows the spherical coordinate system used in the heavy load tribometer.

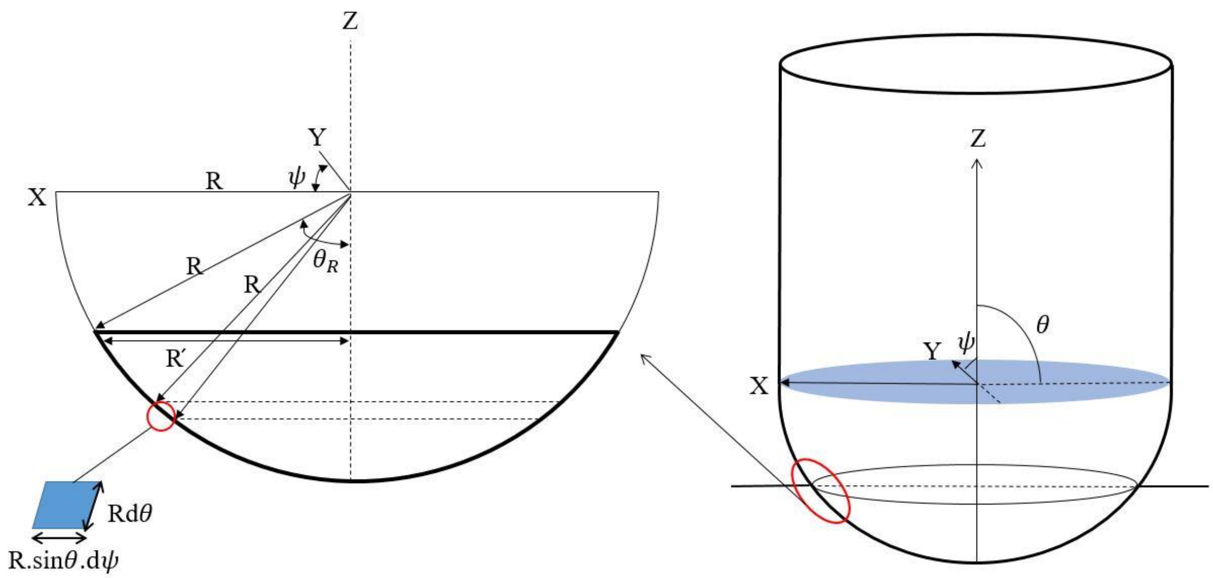

Figure 3-3- A spherical coordinate system for the modified Brinell hardness test.

In this image, R is the pin radius, R' is the indentation radius and dA is the infinitesimal area of the contact. Based on this figure for any point on the interface:

$$R' = R \sin\theta \qquad (3\text{-}4)$$

$$dA = Rd\theta R \sin\theta \, d\psi = R^2 \sin\theta \, d\psi d\theta \qquad (3\text{-}5)$$

In equation (3-4) the integration of θ from 0 to θ_R and ψ from 0 to 2π will cover the entire contact surface.

From basic mechanics, it is known that the moment (M) can be calculated using the force and the distance from the rotation axis (R'):

$$dM = R' \, dF \tag{3-6}$$

where F is the frictional shear force on the infinitesimal area of the contact.

From equations (3-3), (3-5) and (3-6) the moment can be obtained from the following equation:

$$dM = R' \tau_{Ave} \, dA = R' R^2 \tau_{Ave} \sin\theta \, d\psi d\theta \tag{3-7}$$

The total moment on the interface is given by the integration of θ and ψ over the following intervals:

$$M = \int_0^{\theta_R} \int_0^{2\pi} R' R^2 \tau_{Ave} \sin\theta \, d\psi d\theta = \int_0^{\theta_R} \int_0^{2\pi} R^3 \tau_{Ave} sin^2\theta d\psi d\theta \tag{3-8}$$

$$M = \pi R^3 \tau_{Ave} (\theta_R - \sin\theta_R \cos\theta_R) \tag{3-9}$$

At small angles, the following holds:

$$\sin\theta \approx \theta \tag{3-10}$$

Therefore, equation (3-8) can be written as follows:

$$M \approx 2\pi R^3 \tau_{Ave} \int_0^{\theta_R} \theta^2 d\theta \tag{3-11}$$

$$M \approx 2\pi R^3 \tau_{Ave} \frac{{\theta_R}^3}{3} \tag{3-12}$$

Using equation 3-10:

$$\frac{R'}{R} = \sin\theta \approx \theta \tag{3-13}$$

Then equation 3-13 can be used in equation 3-12. The total moment would be:

$$M \approx \frac{2}{3}\pi R'^3 \tau_{Ave} \tag{3-14}$$

If the spindle rotates with a constant speed and the contact reaches the steady state condition the moment (M) will be equal to the reaction torque value given by the torque sensor. Therefore, the average frictional shear stress is:

$$\tau_{Ave} = \frac{3M}{2\pi R'^3} \tag{3-15}$$

Where M is the value which is given by the torque sensor and R' is the imprint diameter [28].

To calculate the average normal stress on the interface, the projected area of contact is used:

$$\sigma = \frac{F_N}{\pi R'^2} \tag{3-16}$$

As was discussed before, the coefficient of friction is the ratio of the shear stress to normal stress, thus:

$$\mu = \frac{\tau_{ave}}{\sigma} = \frac{\frac{3M}{2\pi R'^3}}{\frac{F_N}{\pi R'^2}} = \frac{3M}{2F_N R'} \tag{3-17}$$

3.2.3 Separating external friction and internal shear when operating the MMRI tribometer

As was mentioned previously in this chapter, the MMRI tribometer operates based on a modified Brinell hardness test. The aim of the tribometer is to measure the adhesion between two surfaces under a heavy load while it rotates. As explained in Figure 3-2, region II is the area of interest for this research since it is a source of plastic deformation in the bulk material while avoiding complete seizure. The ratio of the real area to the apparent area of contact should be greater than $\frac{1}{3}$ to be outside of the region I, which is for lightly loaded sliders.

To avoid seizure and obtain the conditions in region II a certain range of normal loads and temperatures should be selected for each workpiece material under study. Choosing to light of a load will not plastically deform the disk and cause the contact interaction to be in region I. Selecting a very high load will cause a seizure in the contact point, which is not the aim of this study. Therefore, a certain range of normal loads can be selected to operate the heavy-load high-temperature tribometer. A combination of normal load and temperature can cause material softening and negative gradient of mechanical properties from the surface to the bulk. As explained in part 2.2.5, this can generate shear in the bulk material which would not show the friction between the pin and disk.

Based on equation (2-14), Fox-Rabinovich [31] proposed a criteria for heavily loaded sliders (HLS) in which the threshold of external friction was defined. It was assumed that plastic strain in the workpiece material would render external friction impossible. Therefore, the interface will be under external friction condition in the following inequality:

$$\zeta = \frac{h}{r} + \frac{\tau}{\sigma} < 0.5 \qquad (3\text{-}18)$$

In which ζ is the external friction threshold, h is the depth of the imprint, r is the radius of the imprint and $\tau . \sigma$ are shear and normal stresses.

If the mentioned inequality is satisfied then the interaction is limited to external friction and the shear stress (τ) shows the stress required to yield adhesive bonds between the pin and disk. In the case of internal shear, the shear stress represents the shear of the layers of the softer material within the bulk of the specimen. In this condition, the reaction torque signal does not reach the steady state and is increasing over time.

Based on the literature and experiments which were conducted using heavy-load high-temperature tribometer it is known that the relative penetration ratio (h/r) is in the range of 0.03-0.15 for different materials [31]. Therefore, the aforementioned inequality can be written as follow:

$$\frac{\tau}{\sigma} < 0.47\text{-}0.38 \qquad (3\text{-}19)$$

As a result, it can be roughly concluded that to have external friction the measured coefficient of friction should be less than 0.5. However, this can be different for each pair of pin and disk and should be investigated for each test. The following figure shows the coefficient of friction values for tests which are performed under different conditions. The image distinguishes between the tests which are performed in internal shear and external friction conditions.

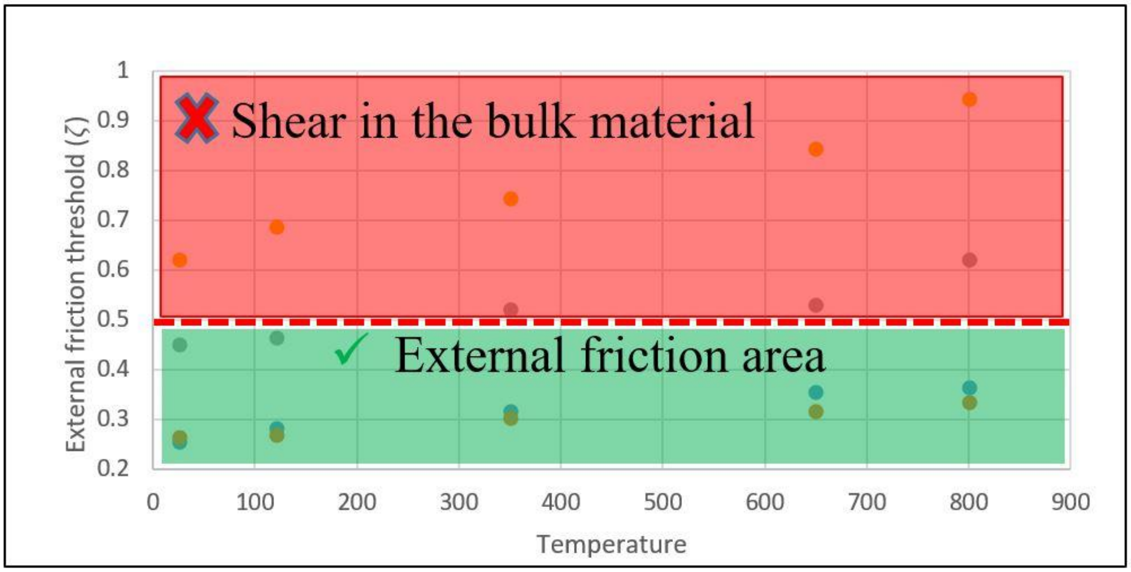

Figure 3-4- Sample results to distinguish between the external friction and shear in the bulk material.

To satisfy equation (3-18), it is necessary to select the right value of the normal load for the test. This load should be high enough to generate plastic deformation on the surface of the disk. However, the normal load should not cause seizure.

In order to find the proper range for the normal load, conducting 3 preliminary tests is suggested prior to running the original test to see which normal load generates the desirable normal stress (about $2\sigma_Y$) instead of seizure and internal shear based on equation (3-18).

According to the aforementioned paragraphs concerning MMRI tribometer mechanics, a summary can be drawn using the following points:

- The MMRI tribometer is designed to mimic the cutting conditions at the tool/workpiece interface. It works based on the modified Brinell hardness test to generate plastic deformation on the contact area while at the same time avoiding seizure. This machine is designed to provide the contact conditions in region II of Figure 3-2 and measure the coefficient of adhesion between a rigid tool and plastically deformed workpiece material.

- The coefficient of friction is measured using the normal load, the value of the moment and the diameter of the imprint. Equation (3-17) is used to calculate the coefficient of friction.
- An external friction condition is crucial to perform this test. Thus, the external friction threshold (ζ) should be satisfied for each test.
- Three preliminary tests are recommended to be carried out before the tribometer is used to measure the COF. These test involve finding the appropriate normal load to be inputted into the tribometer. The load should be about two times higher than the yield strength of the softer material. Also, the test results should satisfy the external friction threshold (ζ).

4 Development of Experimental Procedures

The tests were designed to investigate the effects of input variables (such as pin tip diameter, applied normal load and duration, applied temperature and heating dwell time) on the output parameters (such as reaction torque signal, measured temperature, shear stress, normal stress and coefficient of friction (COF)). This chapter will explain the limitations of the tribometer and try to address these drawbacks by linking the physics and mechanics of the bench-scale tribometer to experimentally obtained results.

4.1 Performance of the tribometer

Based on the objectives of this thesis, the first step is understanding the performance of the tribometer to precisely measure the COF and obtain results that confirm the machining process.

ASTM B265 [32] Grade 5 titanium alloy Ti-6Al-4V in the form of disks was used for the repeat the tests. Table 4-1 shows the chemical composition of the alloy.

Table 4-1- Chemical composition of Ti64 disks

Element	**Al**	**V**	**N**	**C**	**H**	**Fe**	**O**	**Residuals, each/total**
Weight Max %	5.5-6.75	3.4-4.5	0.05	0.08	0.015	0.4	0.2	0.1< <0.4

Based on the ASTM B265 Physical and mechanical properties of Ti-6Al-4V are shown in Table 4-2.

Table 4-2- Physical and mechanical properties of Ti64[32]

Property	**Value**
Density	4.43 g/cc
Tensile Strength	895 MPa
Yield Strength	828 MPa
Elongation %	10 %
Reduction of Area %	20 %
Thermal Conductivity	7.3 W/mK
Specific Heat Capacity	580 J/kgK
Modulus of Elasticity, tension	110 GPa
Hardness, Rockwell C	37 HRC

Uncoated WC with a 6 % cobalt binder pin was used for the tribometer tests. The grain size was 0.8 Micron with a hardness of 92.5 Rockwell C. All the tests were performed from the start using pins with a tip diameter of 3 mm pin. A normal load of 1000 N was selected and tests were carried out at 21, 150, 400, 600, 750, 850˚C. The COF values was compared with the benchmark results. A gap existed between two sets of data, and further tests were designed based on this gap to repeat the published results on the tribometer and find the relationship between input parameters, actual conditions in the contact zone and the resultant COF predictions.

To measure the coefficient of friction, average torque values from the torque signal (the last 30 seconds of each test) were used. Figure 4-1 shows torque signal drifts for two tests using titanium disks and WC pins with the same normal load at two different temperatures (21˚C and 850˚C).

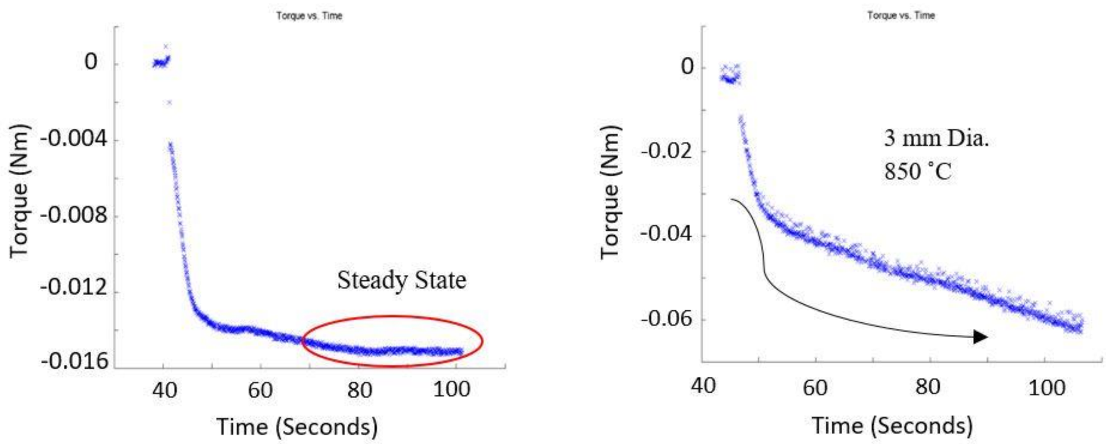

Figure 4-1- Torque signal drift for room and high-temperature tests.

The results for titanium samples show that torque signals for temperatures greater than 400˚C do not reach a steady state condition, which means that torque values keep increasing and the average of the last 30 seconds is not representative of the true torque average value in the tribometer test.

The reason for this phenomenon is that at high temperatures, heat flows to the bulk of the material and softening of the material then takes place. Therefore, the mechanical properties of the material are reduced. As a result, imposing the normal load and rotating the disk would cause shearing from an area far from the interface. In fact, what is being measured in this case is the shear of the bulk material. In fact, plastic deformation of the work piece material would affect COF results. Fox-Rabinovich [31] noted that the seizure phenomenon can happen in Heavy Load Tribo-Systems (HLTS), meaning that external friction transforms into internal shear of the bulk material. Equation (3-18) defines the external friction threshold factor (ζ) [31].

It appears that for each pair of coating and workpiece material, the choice of a specific testing parameters such as normal load can help restrict external friction to the contact zone. The following ideas specify a means to solely measure the external friction in the contact zone (as opposed to a mixture of shear in the bulk material and external friction).

4.1.1 Influence of the pin tip Diameter on the Torque Signal Behavior

Previously, pins with 3 mm diameter were used in the tribometer tests. Pins had a balled tip hemisphere with the 3 mm diameter. The effect of the pin tip diameter on the torque signal drift was put under investigation. A different pin tip diameter can change the normal and shear stresses on the pin tip and as a result, cause transition from shear in bulk material to external friction.

Three different diameters on the pin tips were designed and provided. Pins with 3, 6 and 10 mm tip diameter were selected. Figure 4-2 shows 3D images of the pins with different pin diameters. All the pins had a 3 mm diameter but the diameter of the pin tips was selected as 3, 6 and10 mm. Increasing the pin tip diameter would make the tip flatter.

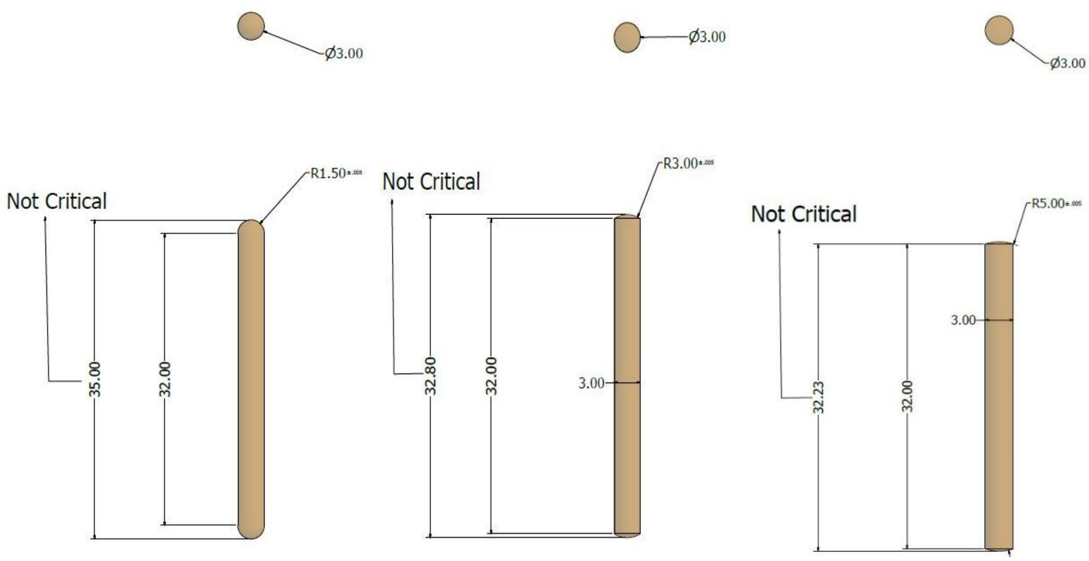

Figure 4-2- 3D drawings of the pins.

Tests were performed under the following conditions: Normal load=1000N, Temperatures: 21, 150, 400, 600, 750, 850˚C. Figure 4-3 shows the COF for the pins with different diameters.

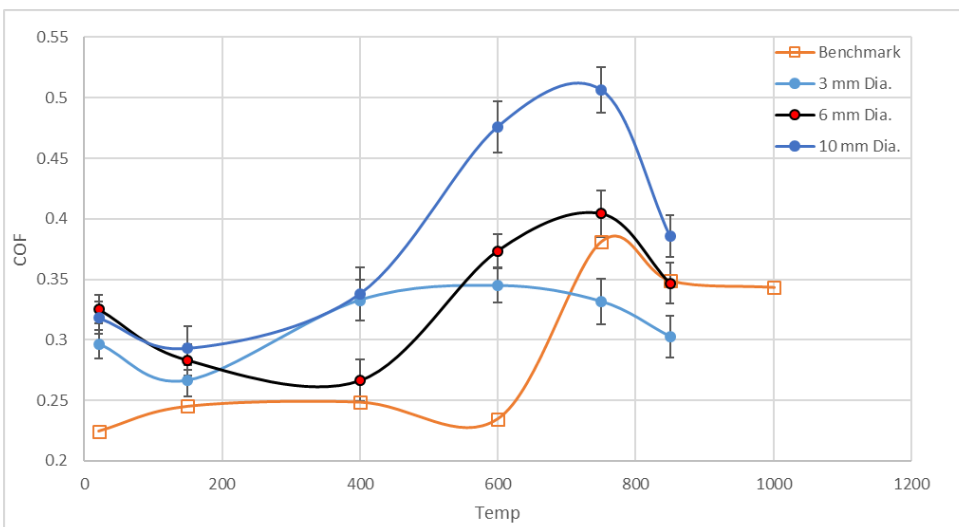

Figure 4-3- COF of pins with different diameters Vs. Ti-64.

Results show that the pin with a tip hemisphere of 6 mm has the closest coefficient of friction values to the benchmark. This pin follows the trend of the benchmark pin but show greater values and needs to be shifted down and right in the graph. The maximum difference between the two graphs occurs at 400 ˚C. Focusing on normal and shear stresses at all temperatures will help to obtain a better understanding of the coefficient of friction results. Figure 4-4 shows normal and shear stresses for pins with 3, 6 and 10mm tip diameter.

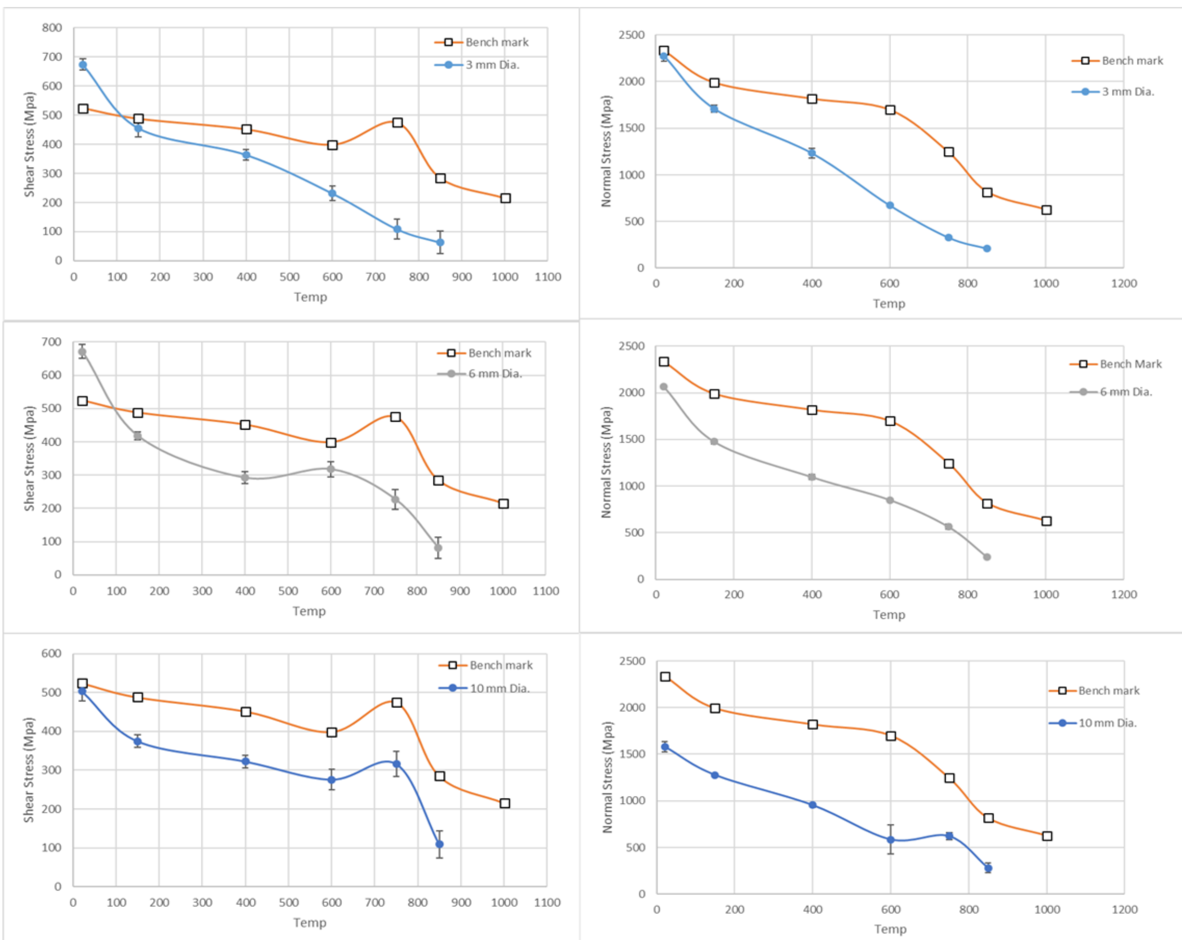

Figure 4-4- Normal and shear stress for WC pins Vs. Ti64 disks.

Graphs show that increasing the pin tip diameter decreases the normal stress, due to a greater projected area in the pins with the greater tip diameter. Shear stress in the 6mm pin has the same trend as the benchmark, but the measured values are less, especially for the high-temperature tests. To analyze shear stress, it is necessary to investigate the effects of heat on the interaction, as well as on the torque signals.

Figure 4-5 shows the torque signal for all the pins at 21˚C and 850˚C. Based on this data the torque signal does not reach the steady state value at high temperatures.

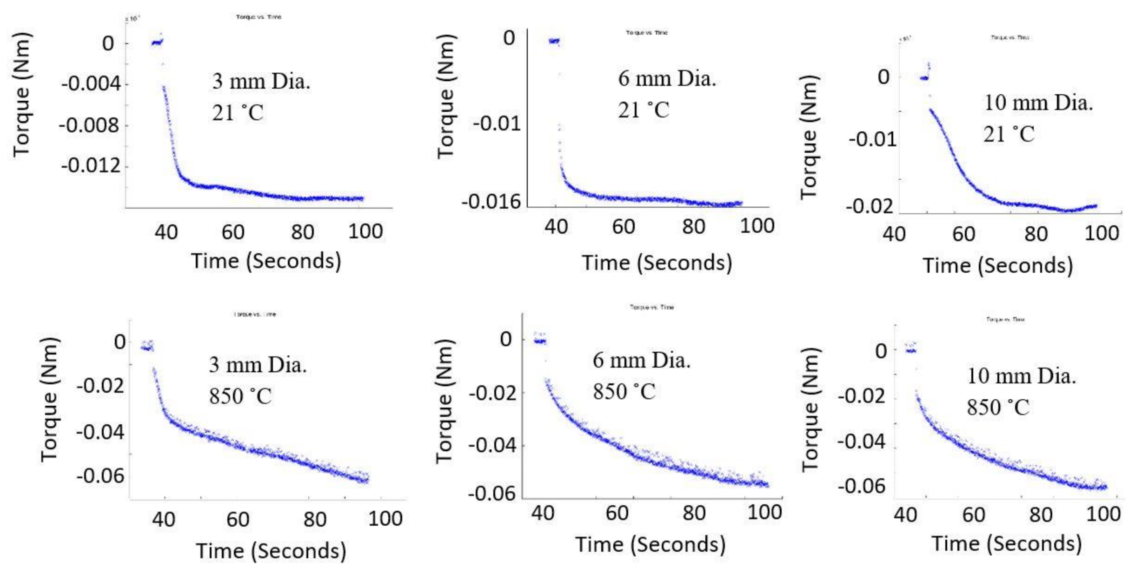

Figure 4-5- Torque signal for different pin diameters in 21 and 850˚C.

It can be seen that tests conducted at high temperature will cause material softening and shear in the bulk material. It can be gleaned from the graph that the pin with 6 mm tip shows a more stable torque signal at 850˚C. In fact, doing tests with 6mm pins changes the normal stress values. Based on this result it is then concluded that lower normal stresses can transfer shear of the bulk material to external friction mode.

Temperature was measured with a pyrometer. Since it's not possible to reach the contact area the temperature is being measured about one millimetre above the contact point. As a result, the measured temperature is lower than the actual temperature in the contact point. This will shift the measured temperature to the left in the graphs. More research is suggested in this area to model the temperature gradient on the pin such that a correction factor for the measured temperature on the pin tip can be found.

In conclusion, it appears that the 6mm pin is in better accord with the benchmark results as it generates a more favourable normal stress. The 10 mm pin has COF values that are not close to the benchmark result. Future testing will work to generate the desired stress state associated with the 6mm diameter pin.

4.1.2 Influence of Heating Dwell Time on the Torque Signal Behavior

The previous study has shown that the pin with the 6mm tip performs better in the tribometer tests, but still, there is a gap between the MMRI tribometer and the benchmark results. Further tests and analysis are needed to clarify this gap and obtain more accurate results.

Heat transfer from the surface to the bulk of the material would cause material softening and consequently, material shearing in areas far from the surface. Another idea for avoiding this phenomenon is to decrease the heating dwell time on the surface of the disk. Previously, after connecting the electrical current, 10 seconds was given to the system to reach the target temperature. This time was enough for the heat to transfer through the material and increase the temperature in its bulk, thereby creating the conditions for material flow underneath the surface. Figure 4-6 shows the sequences of the stages occurring in a tribometer test.

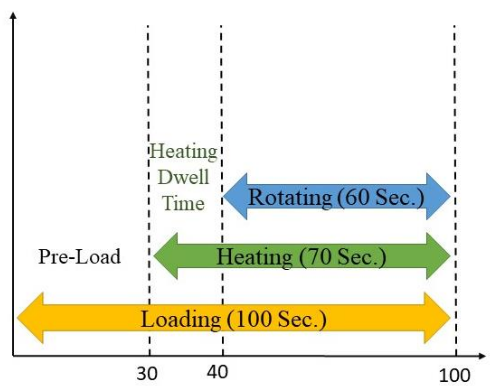

Figure 4-6- Sequences of stages in a tribometer test.

The test begins by pre-loading the tribometer for 30 seconds. The contact point is heated up by resistance heating. When the current is applied to the system, the contact point will heat up for 10 seconds without any rotation which is called the heating dwell time. Rotation will commence for 60 seconds following the heating dwell time. Each test thus takes 100 seconds in total to complete.

This study investigated heating up the disk with and without the normal dwell time of 10 seconds. The tests were done at 550, 650 and 850˚C. Temperatures more than 400 ˚C were chosen since reaching steady state torque signals with Ti64 disks is usually hard at temperatures greater than that amount. The normal force was 1000N and the rotation time 60 seconds. To complete the previous study a pin tip diameter of 6mm was chosen for this sets of tests.

Figure **4-7** shows torque signals for the 6mm diameter pin at three different temperatures with 10 and 0 seconds of dwell time. Torque signals illustrate the effect of the heat duration (10s) on the tests.

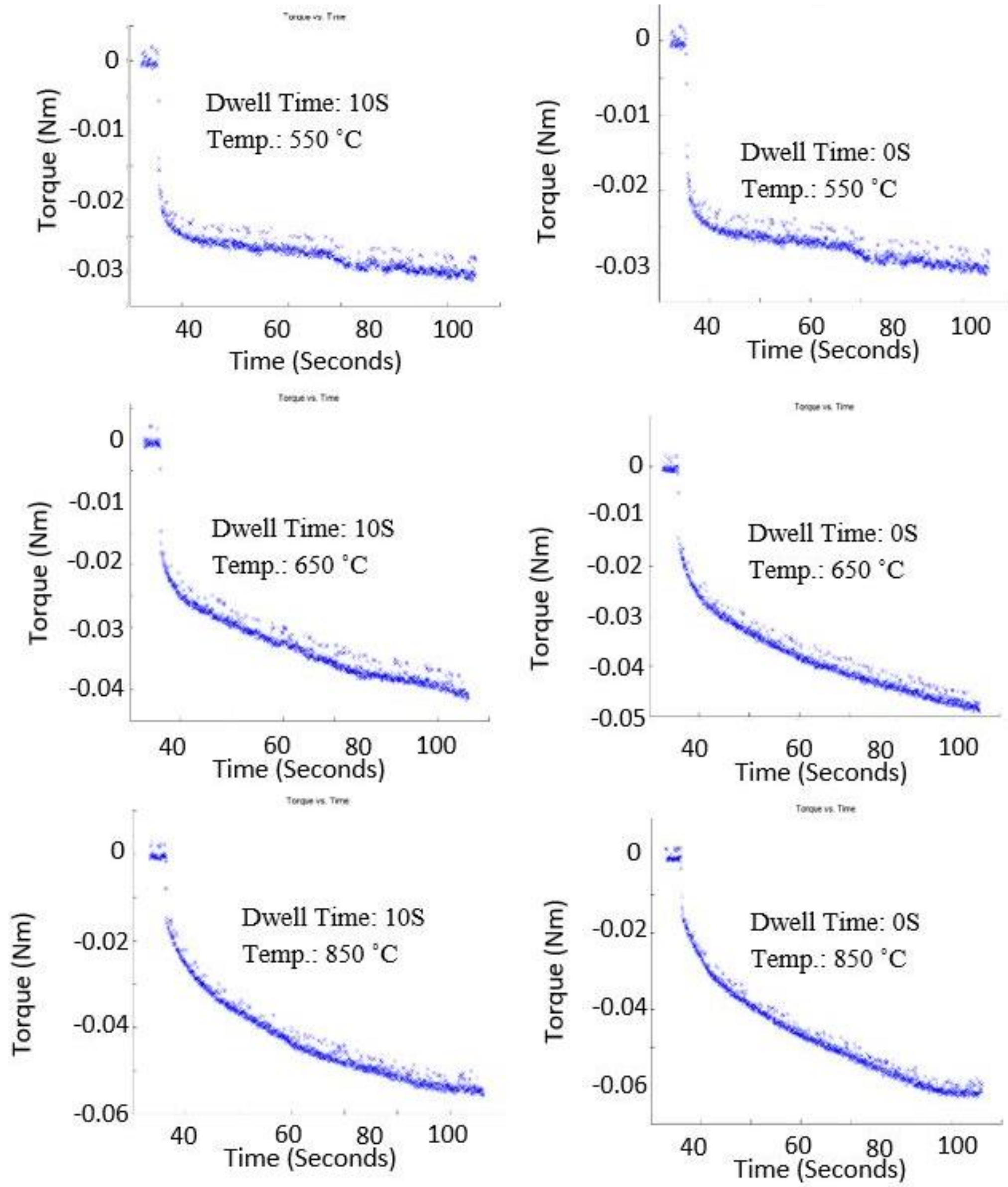

Figure 4-7- **Torque signal of tribometer tests with 10 and 0 seconds of heating duration.**

It can be seen that reducing the heating dwell time does not significantly alter the slope of the torque signals. The rotation of the disk continues for 30 seconds after heating began. As a result, the time is enough for heat to transfer to the material.

Figure 4-8 illustrates that the temperature is reaching the steady state about 20 seconds after the connection of the electrical current. From the point where the temperature reaches a steady state condition, the test continues for 30 seconds, which is enough time for the heat to transfer to the material and cause it to soften.

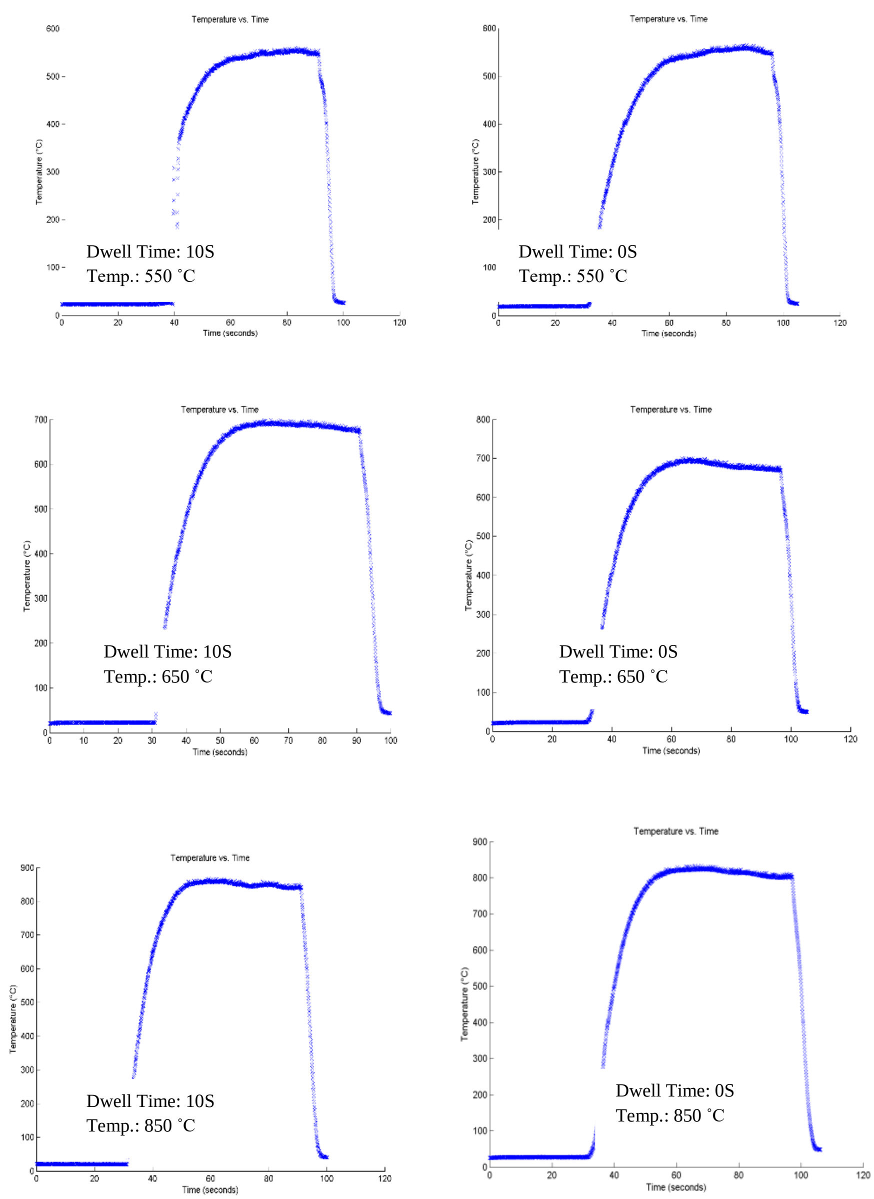

Figure 4-8- Temperature Vs. Time for heating dwell time of 0, 10S.

In conclusion, the heating dwell time was not observed to affect the torque signal because heating time is long enough to alter the friction mechanism. Heating duration does not change the temperature that can be reached in the contact zone during the test but it can impact the measured temperature as time is needed for the heat to transfer up the pin to the region measured by the pyrometer.

4.1.3 Influence of changing the order of tests parameters (Load, Rotation, Heating) on Torque Signal Behavior

As mentioned before the tribometer test was performed in the following order:

1- Imposing the normal load

2- Connecting the electrical current (heating)

3- Rotating

Since heating began prior to the rotation, the combination of imposing the normal load and heating up the disk could produce adhesion bonds between the pin tip and the disk. In addition, the heat would reduce the mechanical strength of the material. Therefore, rotating the disk would cause material flow within the bulk and the adhesion bonds will stick a layer of material to the pin tip.

Changing the test order can be useful to avoid adhesion of the softer material to the pin tip. In this part, the test order was altered to see whether a steady state torque signal could be reached. The new tests were done in this order:

1- Imposing normal load

2- Rotating

3- Heating

Tests were performed under the same normal load and at the same temperatures as the previous tests. Pins with 6mm tip were chosen and Ti64 disks were used for these tests.

Figure 4-9 shows the torque signal for tests which rotated before heating. The normal load was 1000N and the tests were done at 21, 550 and 650 ˚C.

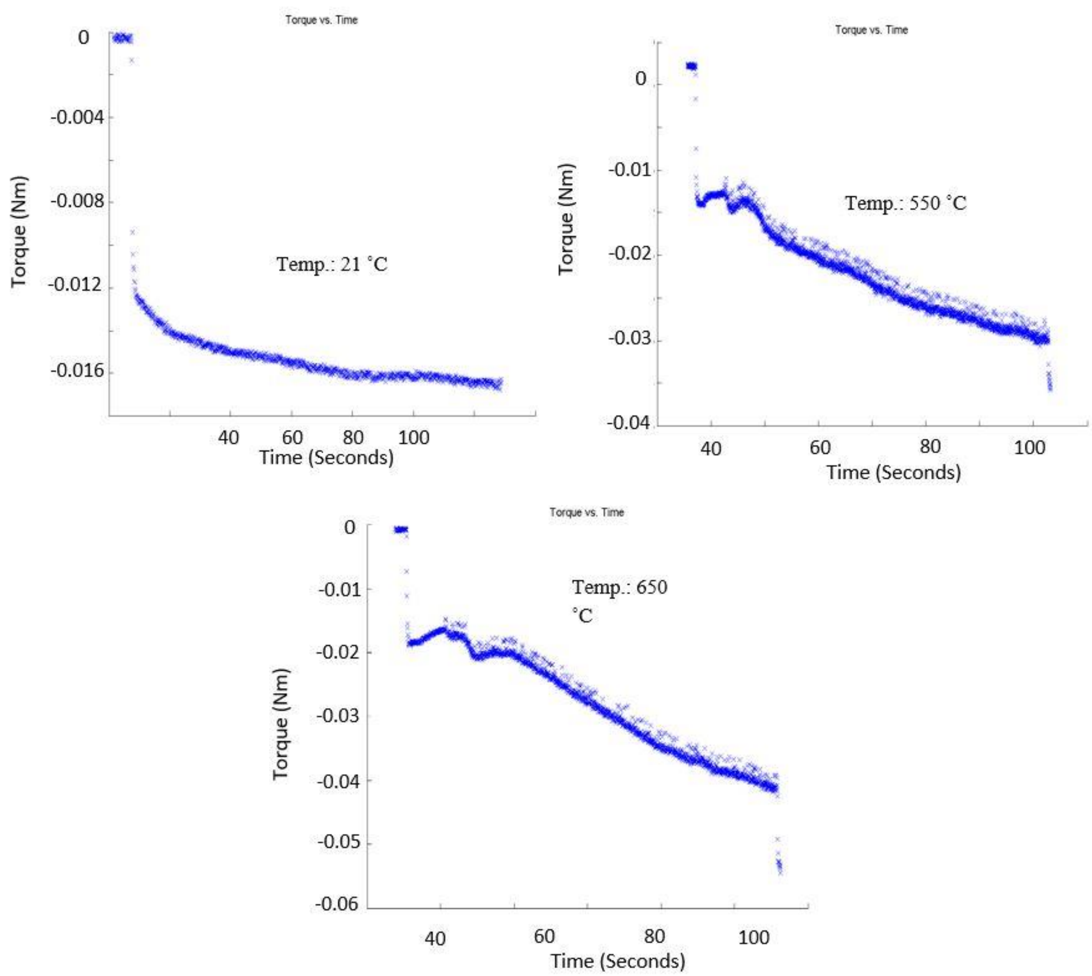

Figure 4-9- Torque signal for the test with rotation before heating.

The figures do not show any improvement in the results. Moreover, it seems changing the testing order has adverse effects on the torque signal drift. Figure 4-10 illustrates the temperature changes during the time at 21, 550 and 650˚C. If heating follows rotation, the temperature can't reach the desirable level quick enough. In fact, the torque signal is being recorded in a part of the test while the temperature has not yet reached its final value. Therefore, when using this sequence, the torque signal can't reach the steady state condition.

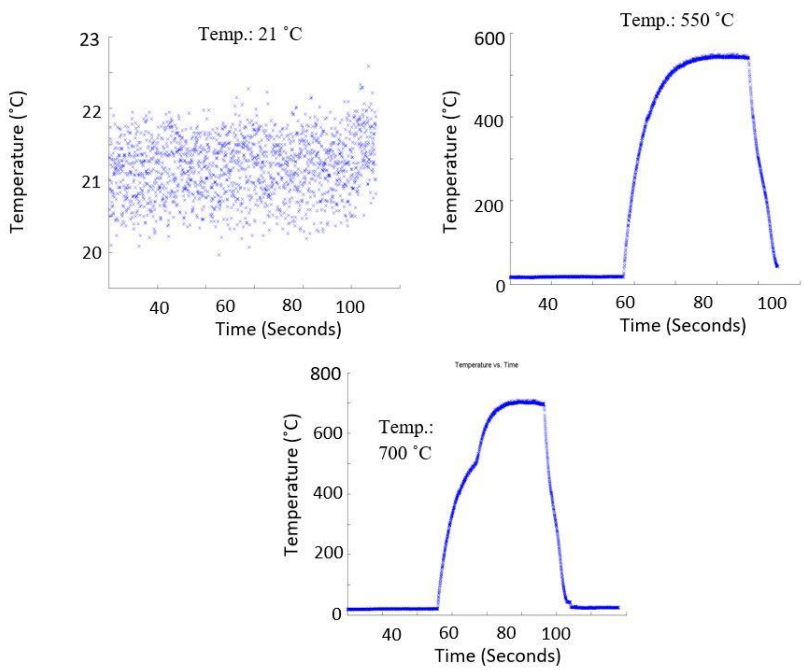

Figure 4-10- Temperature Vs. time for changed test orders at 21, 550 and 650 ˚C.

It conclusion it can't be said that changing the order of the tests improves the results in any way. Conducting the tests in the previous order is thus recommended to avoid temperature fluctuation and to quickly reach the desired temperature.

4.2 Effect of coating deposition time on the measured COF tribometer

WC pins with 6% Cobalt were selected for this study. All the pins have a 3mm diameter but two different geometries were chosen for the pin tips. The first batch of the pins has a tip diameter of 3mm and a tip diameter for the other batch is 6mm. Figure 4-11 shows the schematic of the pins. Two different coatings were applied on the pins. Coating A has 50% of Aluminum and 50% Titanium. The deposition time for the coating was 25 minutes. Coating B has the same chemical composition but a deposition time of 75 minutes. In this study, the tribological performance of listed coatings is compared with the uncoated WC pins. The disks are made of Super Duplex Stainless Steel_ UNS S32750. The diameter of the disks is 3 cm and the thickness of all the disks is 1cm. Table 4-3 shows the pins and coatings used in this study.

Table 4-3- Coatings and pins for the study

	Pin Code	Rod Dia.	Tip Dia.	Chemical composition	Deposition time
Uncoated	UP3	3mm	3mm	NA	NA
	UP6	3mm	6mm	NA	NA
Coated	5525.3	3mm	3mm	50% Ti, 50% Al	25 minutes
	5525.6	3mm	6mm	50% Ti, 50% Al	25 minutes
	5575.3	3mm	3mm	50% Ti, 50% Al	75 minutes
	5575.6	3mm	6mm	50% Ti, 50% Al	75 minutes

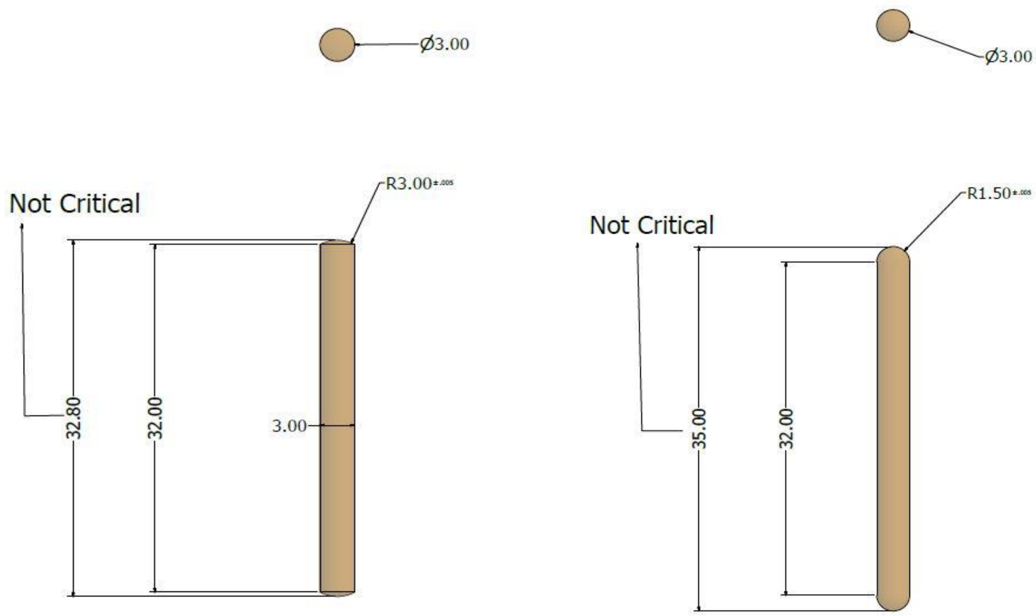

Figure 4-11- Schematic view of the pins.

To perform the tests, the disks were polished with SiC sandpaper. The pins were aligned in the collet with the axis of sample rotation and the pin tips were cleaned with ethanol. A 1000N normal load was chosen and a preload was applied for 30 seconds. Five different temperatures were selected: Room temperature, 120˚C, 350˚C, 650˚C, and 800˚C. The welder began to function following the preload and resistance heating caused the contact zone to heat up. Afterwards, the stage began to rotate at a speed of 2 RPM. The reaction torque sensor records the torque in the contact zone. The rotation time is 60 seconds. Then, the pin was retracted. Each test was repeated 3 times. The imprint size was measured using a 3D measurement microscope (Alicona) and the coefficient of friction was calculated using the normal and shear stresses.

Based on the ASTM standard of Brinell testing (ASTM # E10- 08), the print diameter has to be measured in at least two different locations with the average value reported. Due to the applied heavy-load and high-temperature, a layer of build up or pile up deformed material will form around the imprint of the pin when the pin is imposed against the disk. The diameter of the imprint must be measured on the reference plane of the disk. The optical microscope will show the top view of the imprint and will overestimate the diameter since it's measuring the diameter along the deformed lips. Figure 4-12 shows the 3D image of the imprint and its cross section.

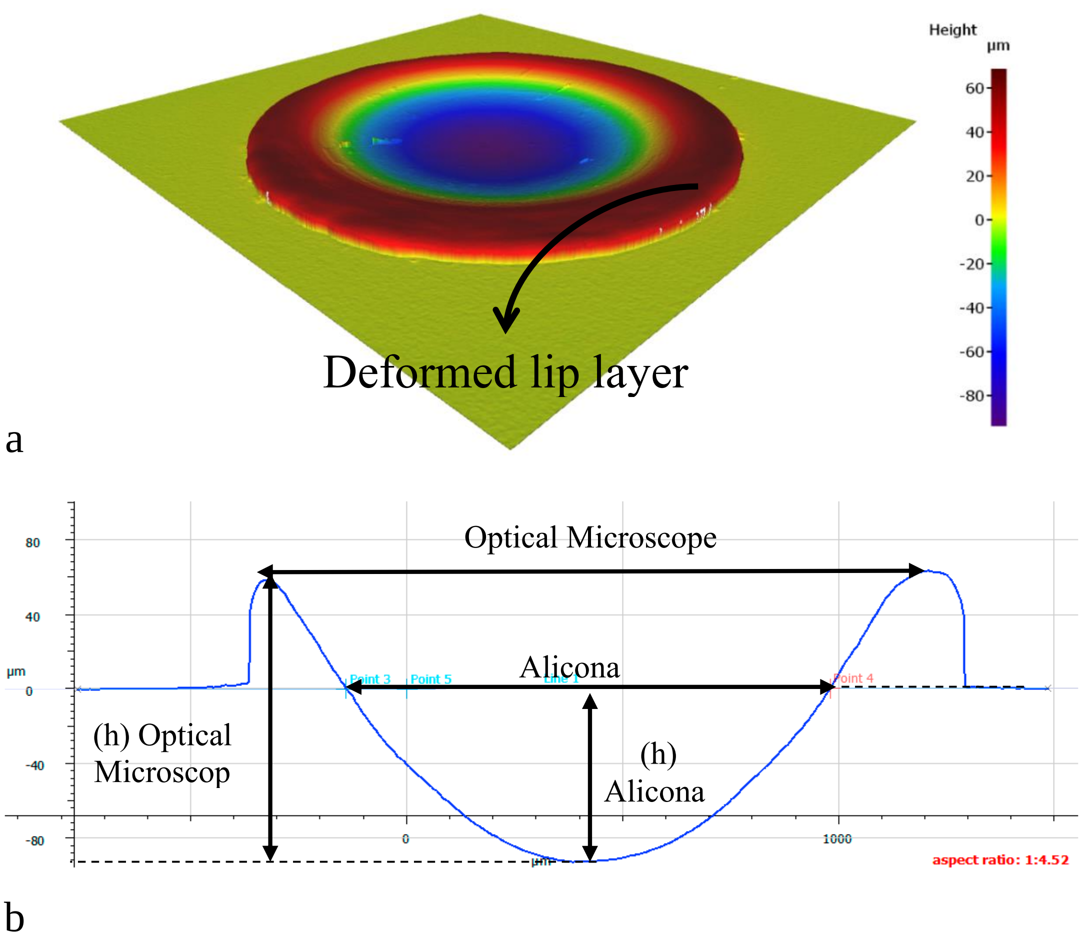

Figure 4-12- a) 3D figure of the imprint b) Cross section of the imprint.

It can be seen that there is a significant difference between the diameter measured with the optical microscope and the one measured by Alicona. At high-temperature tests that result in a thick layer of the pile up, the error for the measurement is around 25%. Another parameter that must be measured is the height of the imprint. In the height (h) measurement, the same error will occur under an optical microscope. To avoid all these errors, the imprints were measured using a high-resolution 3D measurement microscope (Alicona). Figure 4-12 describes the scanning of the imprints and the measurement of the diameter and the height.

The roughness of the coated and uncoated pins was measured with the Alicona 3D microscope. All the pin tips were scanned and the roughness on the flat surfaces was measured after removing the hemispherical form of the tips. Figure 4-13 shows the scanned tip and the flat surface for the roughness measurement of the 6mm tip. Table 4-4 presents Ra results for coated and uncoated 3mm pins.

Table 4-4- Roughness values for the tip of coated and uncoated pins

Pin	Roughness
Uncoated	0.524631μm
5525 (50%Al 50%Ti, Deposition time: 25Minutes)	0.801158μm
5575 (50%Al 50%Ti, Deposition time: 75Minutes)	0.752197μm

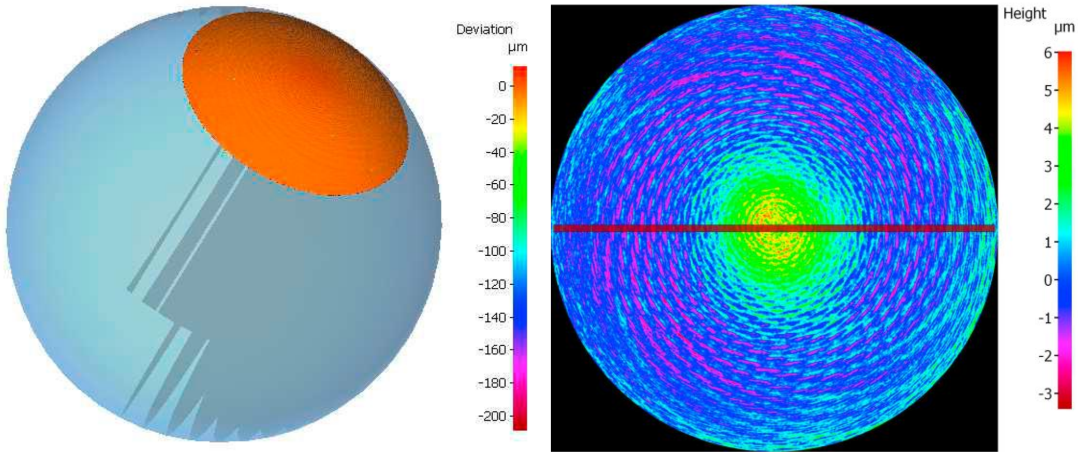

Figure 4-13- Scanned pin tip and the flat form removed surface for roughness measurement.

After the tests were carried out, imprints on the disks were studied under a scanning electron microscope (SEM). The reason was to analyze wear mechanisms and to look for any adhered material or coating delamination. Figure 4-14 shows Back-scattered and Secondary images of imprints for a 6mm coated pin (50%Al 50%Ti, Deposition time: 75 Minutes) at the room and high temperatures. Secondary images show more topology of the surface and can clarify the wear mechanisms in greater detail. However, BSE images showed greater chemical composition contrast, which can help determine the different elements present in the contact zone.

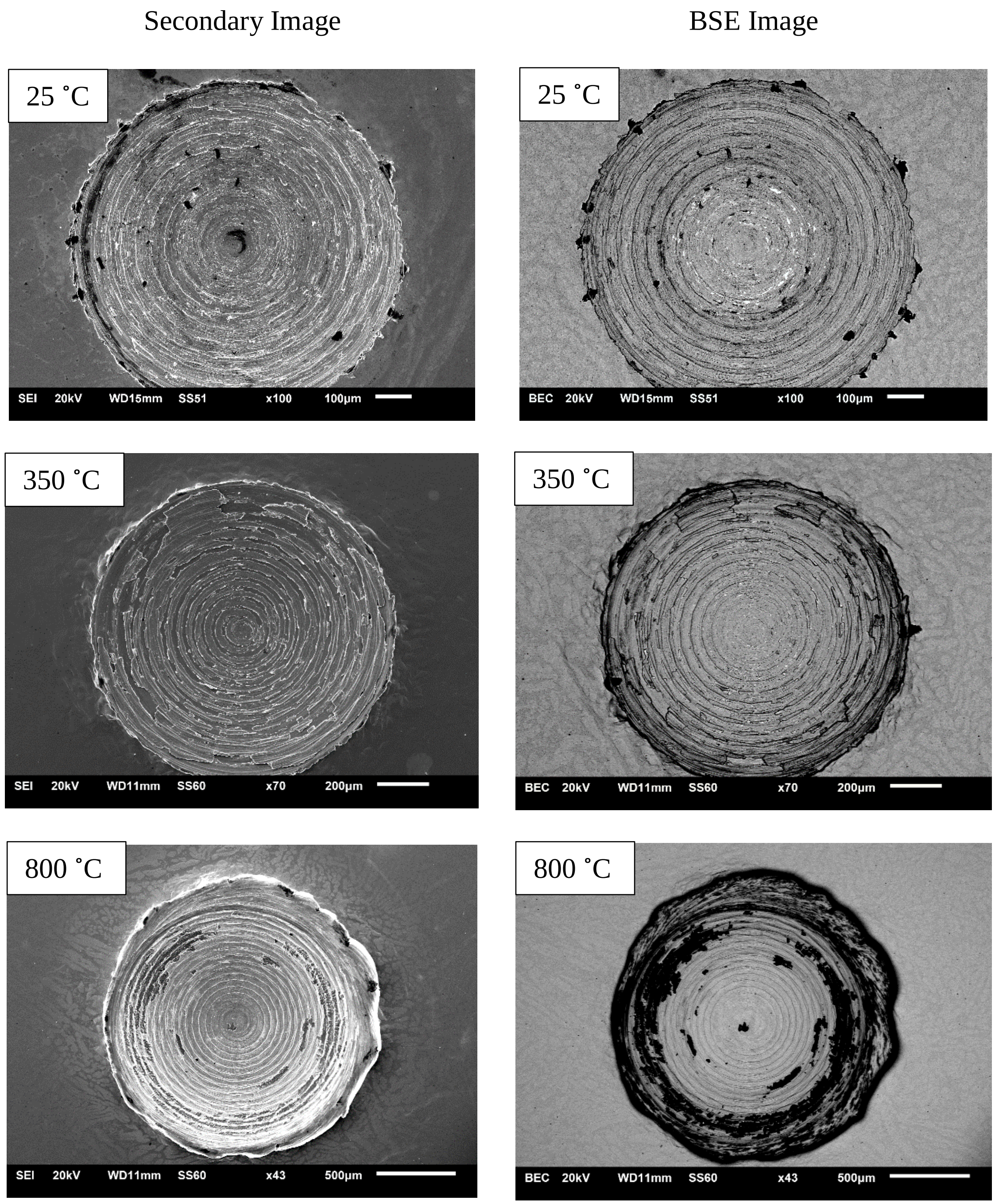

Figure 4-14- SE and BSE images for the coated pin (50% Al, 50% Ti, deposition time:70 minutes).

Following the tests, the raw data was imported into MATLAB and the imprint size was given as an input to compute the normal and shear stresses. The COF value was then calculated based on the normal and shear stress values.

The following graphs shown in Figure 4-15 show the values of the coefficient of friction for the uncoated and coated pins.

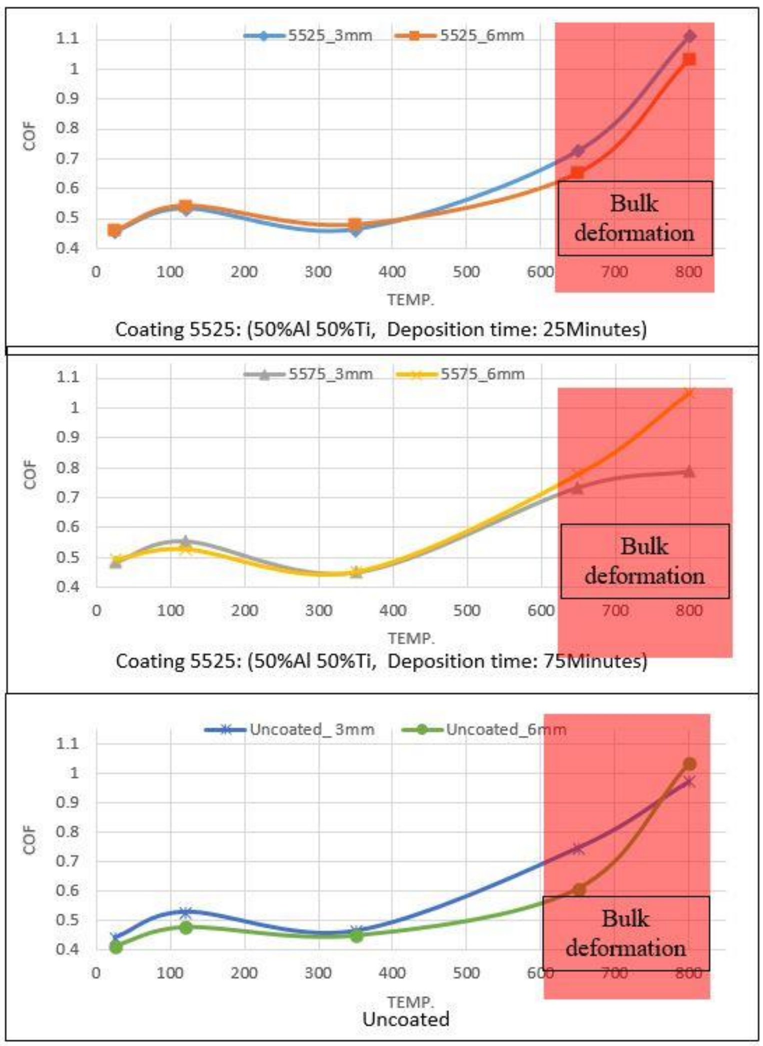

Figure 4-15- Coefficient of friction of coated and uncoated pins with different pin diameters.

To properly compare the pins and coatings it is necessary to compare the normal and shear stresses. Figure 4-16 shows the normal and shear stresses for the coated and uncoated pins with different pin diameters.

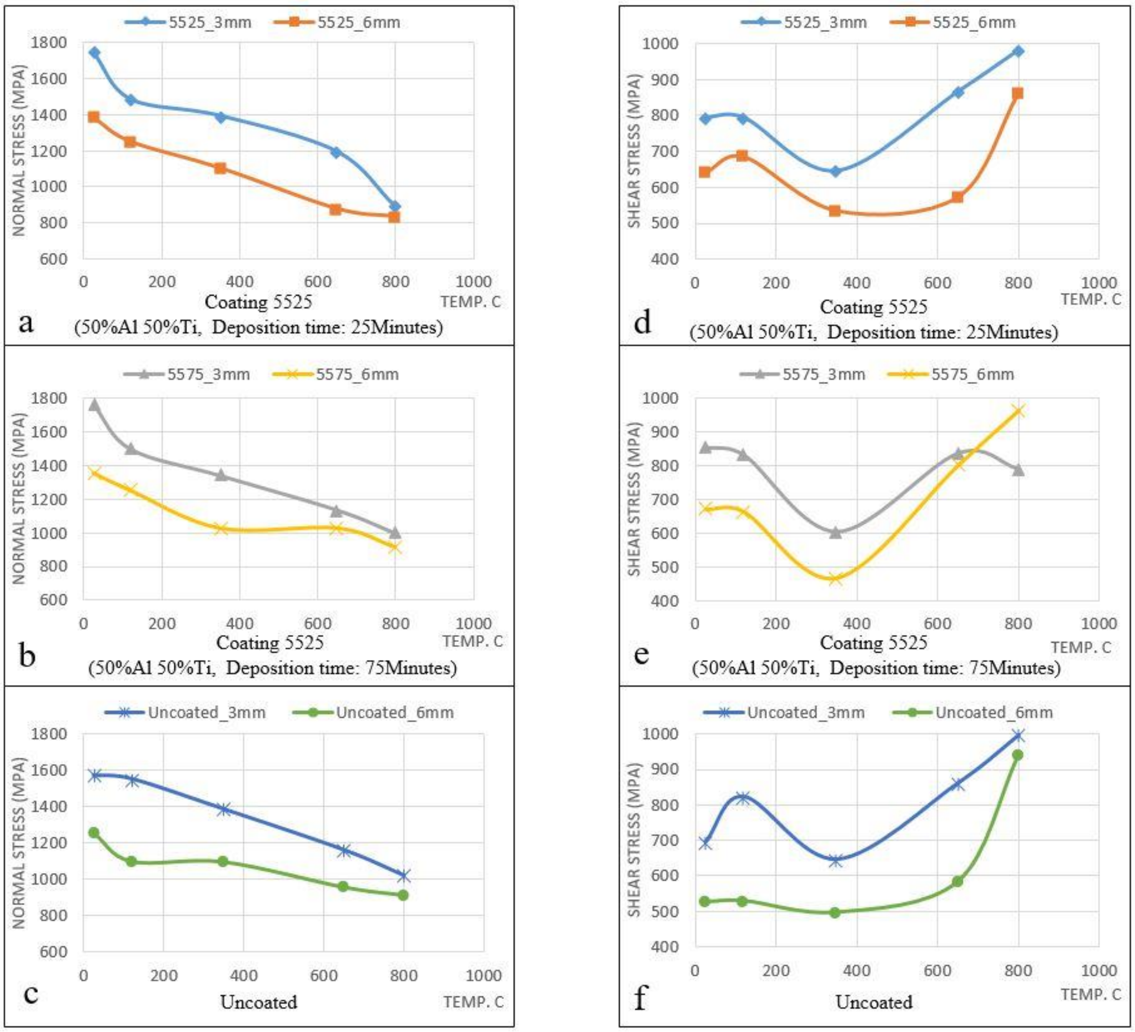

Figure 4-16- Normal and shear stresses for coated and uncoated pins with different pin diameters.

This figure shows the normal and shear stresses for coated and uncoated pins under testing temperatures. In all cases, increasing the temperature results in lower normal stress.

A higher temperature will decrease the material’s yield strength and as a result, more material will deform under the same normal load, which will lead a greater imprint diameter. The same normal load and a bigger area will reduce the normal stress at high-temperature tests. To analyze the change in the normal and the shear stresses, it is necessary to observe the change in the imprint diameter of the different pin tips. Figure 4-17 depicts the change of the imprint diameter under the testing temperatures. Increasing the diameter will result in a lower normal stress.

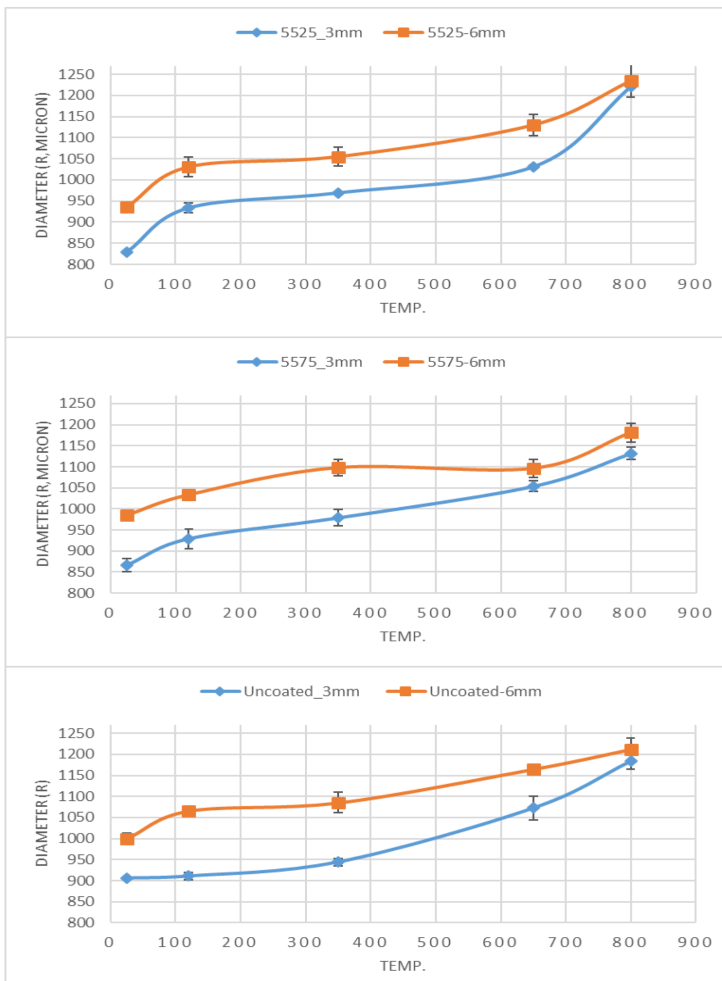

Figure 4-17- Diameter of imprints for different pin tip diameters.

However, the shear stress is more complicated. To understand the changes in the shear stresses it is important to see the reaction torque (M) variation and changes in the imprint diameters. Figure 4-18 shows changes for the torque reaction at different temperatures.

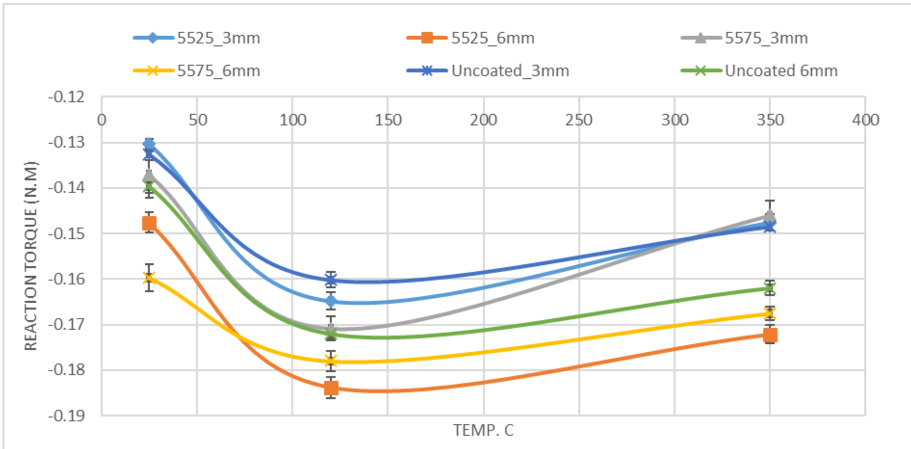

Figure 4-18- Reaction torque values for uncoated and coated pins.

As can be seen in figure 4-18 from room temperature to 300˚C the absolute value of the torque increased. The imprint diameter of all pins increased as well. Based on equation (3-15) the shear stress is the function of the third power of the imprint diameter. The combined effects of the third power of the diameter and the torque value will keep the shear constant or will increase it in some cases. From 300˚C to 500˚C the absolute values of the reaction torque decrease slightly. The smaller torque values and bigger imprint diameters in all cases caused a reduction in the shear stress values and coefficient of friction. For the last two tests at 650˚C and 800˚C increasing temperature will generate a negative gradient of the mechanical properties in the disk. Therefore, under the heavy load, plastic deformation of the workpiece material can happen. As mentioned in chapter 3 in the case of bulk plastic deformation the measured reaction torque is caused by the shear between layers of the material. Thus this value does not isolate the external friction between the pin and the disk that we are interested in measuring. This behaviour is a function of the material properties at that temperature. This is happening for all uncoated and coated pins at high-temperatures. Based on the external friction threshold (ζ) [31] in equation (3-18) the transition to plastic deformation of the bulk will happen if the mentioned inequality is not satisfied.

Therefore, the external friction threshold was checked for all the tests using the measured imprint height (h) and imprint diameter (r). Figure 4-15 determines the tests which were performed under the bulk shear condition. As mentioned before, a welder was used to generate the current and heat up the contact point with a resistance heating method. These results show that the heating system can't generate localized heat on the contact point and that passing a current through the bulk material as well as heat conductivity in the disk, would cause material softening and shear in the bulk material under high temperature. Figure 4-16 shows that Shear stress values at temperatures higher than 350˚C increased drastically, which is more evidence that shows the shear of the bulk material is occurring.

Figure 4-16 also reveals that pins with a tip diameter of 3 mm experience higher normal and shear stress. This is due to the geometry of the pins. When both pins are penetrating to the flat surface with the same normal load, the pins with the 3 mm tip are delving deeper into the material however, the imprint has a smaller diameter. In fact, using the same normal load for the same pins will deform the same volume of the disk material. The pin with the

3 mm tip diameter will push the material deeper but will deform the material less in the radial direction. However, the pin with the 6 mm tip diameter will deform material more in the radial direction rather than going into the depth of material. This is a result of the geometry of the pin. It is possible to quantify geometrical characteristics of the pin by defining the relative penetration ratio as the ratio of height to diameter of the imprint (h/r). This parameter can change the stress distribution and guide the selection of the pin geometry. Figure 4-19 illustrates the relative penetration for the uncoated and coated pins with a 3mm and 6mm tip diameter, respectively.

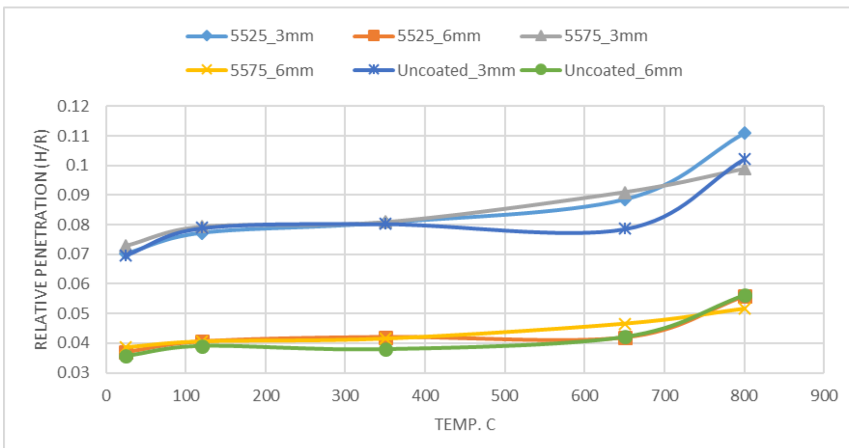

Figure 4-19- Relative penetration for the coated and uncoated pin.

It can be seen that all the pins with the same pin tip diameter have almost the same (h/r) ratio. Generally, pins with a 3mm pin tip diameter have a higher (h/r) ratio since in these pins, the tip is a complete hemisphere. However, the pins with a 6mm tip diameter show a smaller relative penetration ratio because their tip is part of a larger sphere. As a result, the 6 mm pins are flatter and when they penetrate, they deform the material less in the depth direction. Having less (h/r) ratio for 6 mm pins will generate a larger projected area and therefore, the normal and shear stresses will be lower in the 6 mm diameter pins.

There is just one exception in the performed tests. Figure 4-16 (e) shows that from 650˚C onward, the shear stress for the 6 mm pin is getting close to the shear stress of the 3mm pin and then at 800 ˚C shear stress of the 6 mm pin is greater than that of the 3 mm pin. To investigate the cause of this, the imprint on the disk was studied under a scanning electron microscope (SEM) and EDS analysis was conducted to investigate the presence of elements. Figure 4-14 shows the Secondary and Back-scattered image of the imprint for the test conducted at 800˚C with a 6mm coated pin. The black layer in the imprint is not from the workpiece material. EDS analysis illustrates that the black area contains Aluminum and Titanium. In fact, the coating detached and adhered to the disk due to the harsh conditions of that test. This will cause more shear during the test, increasing both the shear stress and the coefficient of friction and not provide the COF value of interest.

To understand the change in COF using coated pins it is necessary to observe and compare COF values for pins with the same diameter in separate graphs. Figure 4-20 compares the coefficient of friction of uncoated and coated pins with different diameters.

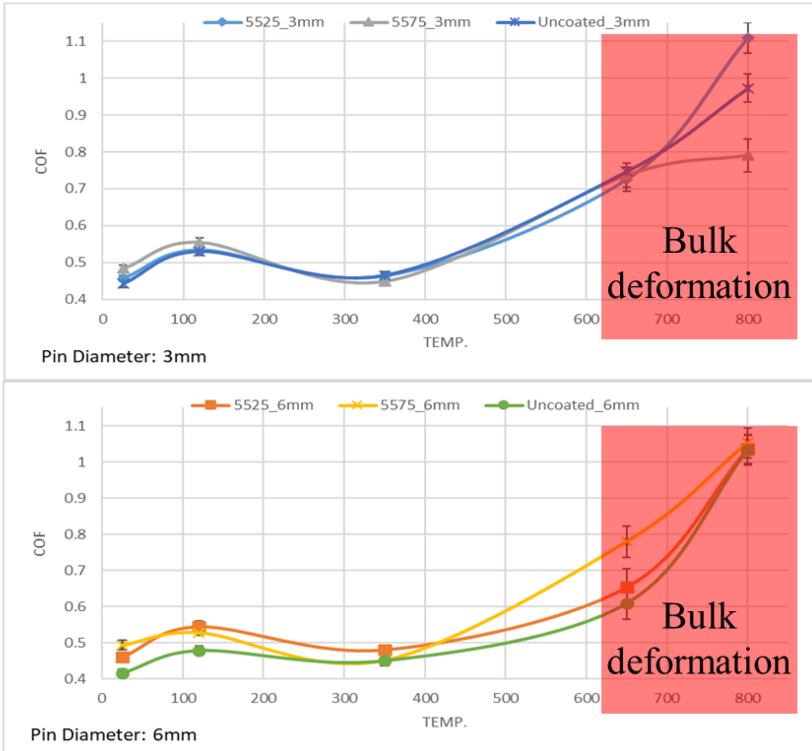

Figure 4-20- Coefficient of Friction for pin diameter 3mm and 6mm.

This figure shows the coefficient of friction of the coated and uncoated pins of 3 mm and 6 mm tip diameters in one graph. Neither coating significantly decreased the COF. In fact, in some cases, the coatings increased the COF of the pins. The reasons for that are as follows. First of all, neither aluminum nor titanium coatings have lubricious effects, and as such, a lower COF value was not expected. In addition, the roughness of the coatings can affect the friction force. Table 4-4 shows roughness values of the coatings and the uncoated pins. It can be seen that both coatings have higher roughness. Generally, the coated pins have a higher roughness than the uncoated pin. Out of the two coatings, the one with the lower deposition time (5525) shows a higher roughness. This will result in the coated pin having more abrasive wear and ploughing during the tribometer tests and as a result the average coefficient of friction of the coated pins will increase. In industrial practice, tools are not being put in use immediately after coating deposition. All tools undergo a post-treatment process to reach acceptable roughness. Therefore, it is recommended all the pins should be polished with a 800 grit SiC sandpaper prior to the tests. Future comparisons of coated and uncoated pins should be carried out by polishing coated pins using a 800 grit SiC sandpaper under a 10 N normal load and a speed of 400 rpm.

4.3 Effect of the substrate bias voltage and Nitrogen pressure on the measured coefficient of friction of the coatings

Changing coating the deposition parameters such as deposition time, substrate bias voltage and reactive gas pressure can affect the mechanical and tribological properties of a coating. In this section, the effect of coating deposition parameters on the coefficient of friction is investigated.

WC pins with 6% Cobalt were used in this study. From previous studies, it was concluded that the pin with a 6 mm tip diameter has better performance in terms of shear and normal stress. Therefore, the pins with 6mm tip diameter were chosen. Ti-Al-N coatings with different deposition parameters were applied on the pins. All coatings have the same chemical composition of 40% titanium and 60% of Aluminum. Deposition time for all the coatings was the same. Low, medium and high bias voltage and Nitrogen pressure was applied during the deposition process. The following table shows the name, chemical composition and deposition parameters of each coating.

Table 4-5- PVD Coatings deposition parameters

Coating code	Ti	Al	Bias Voltage	Nitrogen Pressure
4684_10	40	60	Medium	Low
4684_25	40	60	Medium	Medium
4684_30	40	60	Low	High
4684_70	40	60	Medium	High
4684_110	40	60	High	High

Mechanical and morphological properties of the coatings are not intrinsic properties of the materials. Principles of materials engineering state that all the properties are influenced by grains growth, grain boundaries and flaws within the coating. Therefore, coating deposition parameters can change the microstructure of the deposited material and as a result affect the mechanical properties, deposition rate and structure of the coatings. To obtain a better understanding of the coating tribological behaviour, it is necessary to characterize and evaluate coating properties. The following table illustrates thickness, mechanical properties and roughness of the mentioned coatings:

Table 4-6- Properties of the deposited coatings[33]

	Coating Code	Thickness (µm)	Hardness (Gpa)	Elastic Modulus (Gpa)	Surface Roughness Sa (nm)
Bias Voltage	4684_30	5.27±0.06	30.1±2.4	521.5±75.2	238±4
	4684_70	8.96±0.14	33.3±3.0	446.3±53.9	281±11
	4684_110	8.28±0.15	33.6±2.0	433.0±30.1	307±10
N2 Pressure	4684_10	6.20±0.11	36.7±2.8	467.0±47.6	247±3
	4684_25	8.71±0.19	35.4±2.6	453.6±43.3	256±5
	4684_70	8.96±0.14	33.3±3.0	446.3±53.9	281±11

Increasing substrate bias voltage will cause ions to hit the surface with more energy and penetrate deeper into the thin film. As a result, vacancies in the thin film will be filled by the high energy ions. Therefore, the packing density of the coating will improve and this will decrease the coating thickness [34]. However, in the deposited coatings thickness increased as bias voltage went from low to medium. This can be attributed to the high intrinsic energy of the ions even at a low bias voltage [35]. The deposited coating would be dense enough even at the low bias voltage. Further increasing the voltage will increase the thickness of the coating. A further rise in the bias voltage from the medium to high voltage will accelerate densification in the coating which results in a slightly reduced thickness per hour of coating time.

As mentioned, the coating with the low bias voltage has a fairly high packing density and thus also a high hardness. Increasing the bias voltage will increase the packing density and preferred crystal orientation (100) which will further increase the hardness [34].

Roughness is also a function of the substrate bias voltage. A higher bias voltage will generate ions with higher energy. The collision of ions with higher energy will generate a higher local temperature and energy density on the film surface. Nucleation of grains will accelerate within the coating due to the higher energy density. On the other hand, collision of high energy ions with the substrate will increase the average substrate temperature [36]. When the temperature is high on the surface of the substrate, the grain will grow in size and make the surface rougher. The deposited coatings confirm this hypothesis. Increasing the substrate bias voltage from the low to high bias voltage generated higher roughness in the coatings.

Table 4-6 shows as the Nitrogen pressure in the coating deposition process grows, the coating becomes thicker. Having a higher Nitrogen pressure will reduce the mean free path for the ions since they will collide more frequently with the Nitrogen atoms. As a result, ions will have less energy at a higher Nitrogen pressure, which will increase the deposition rate and the thickness of the coating [37] while at the same time, reducing its hardness. However, higher nitrogen pressure has adverse effects on the roughness of the coating. Table 4-6 illustrates that increasing the nitrogen pressure will increase the roughness of the coatings.

Heavy-Load High-Temperature Tribometer tests were conducted to assess tribological behaviour of coatings in contact with super duplex stainless steel disks. All disks were polished using SiC abrasive papers up to 1200 grit. As was recommended in the previous section, all coated pins were polished with a 800 grit SiC sand paper under 10 N normal load and 400 RPM speed. This procedure ensures that the roughness of the coatings would not affect their tribological characteristics.

A normal load of 700 N was chosen for the tests. For each coating the coefficient of friction was measured at five different temperatures: 24˚C, 150˚C, 350 ˚C, 550˚C and 700˚C. Temperature readings were taken 1 mm higher than the contact point with a pyrometer. A pre-load of 700 N was applied and after 30 seconds, the welder began to transfer the current into the system. There was a 10 second heating dwell time to reach the temperature. Afterwards, the stage began to rotate with a speed of 2 RPM for 60 seconds. The torque signal was recorded once preload was applied. Shear stress was calculated from the average of the torque signal of the last 30 seconds of the tests. Based on the ASTM standard of Brinell testing (ASTM # E10-08) the imprint diameter was measured using an Alicona 3D microscope. Normal stress was given by the normal load and the projected area of the contact. The COF was calculated using the normal and shear stress during the tests.

Figure 4-21 shows the COF, shear stresses and normal stresses for the coatings which were deposited with different bias voltages at the same nitrogen pressure. Also, all the values were compared with the uncoated pin.

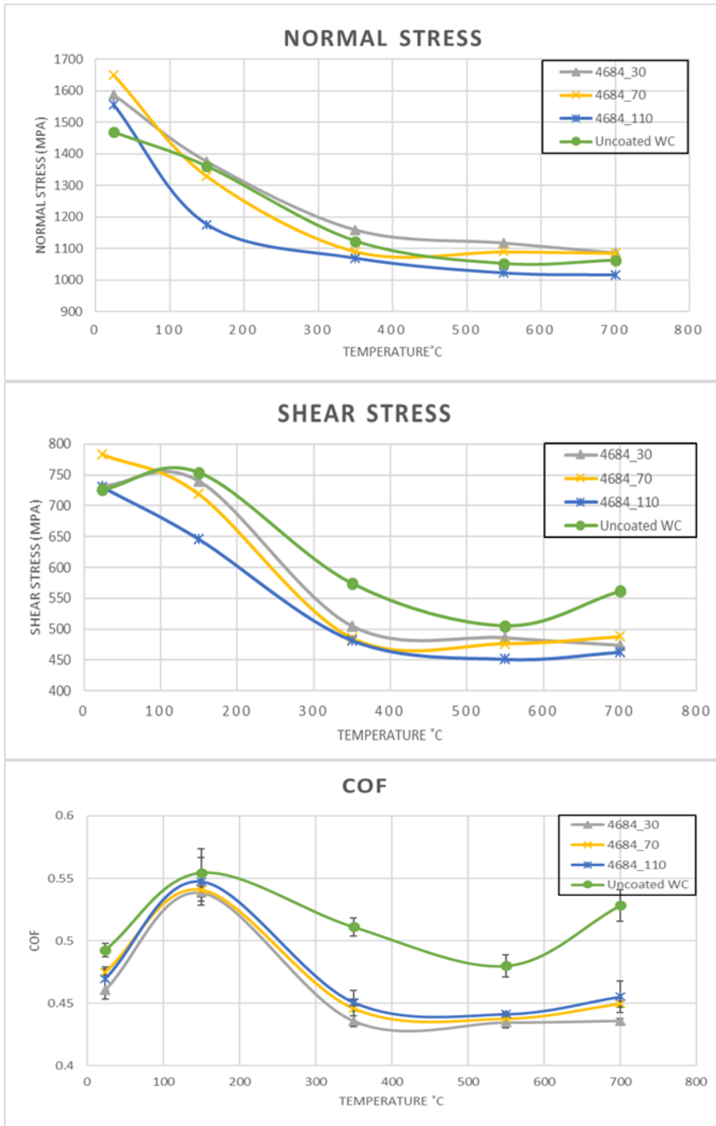

Figure 4-21- Effect of substrate bias voltage on normal stress, shear stress and coefficient of friction of deposited coatings.

First, all the COF values checked with the external friction threshold (ζ) to make sure that the tests satisfy the external friction condition. COF results show that all the tests conducted in the external friction condition. The coefficient of friction values are shown in the column graph, illustrating the improvement of tribological performance in each coating. Figure 4-22 shows the improvement of the tribological performance of each coating.

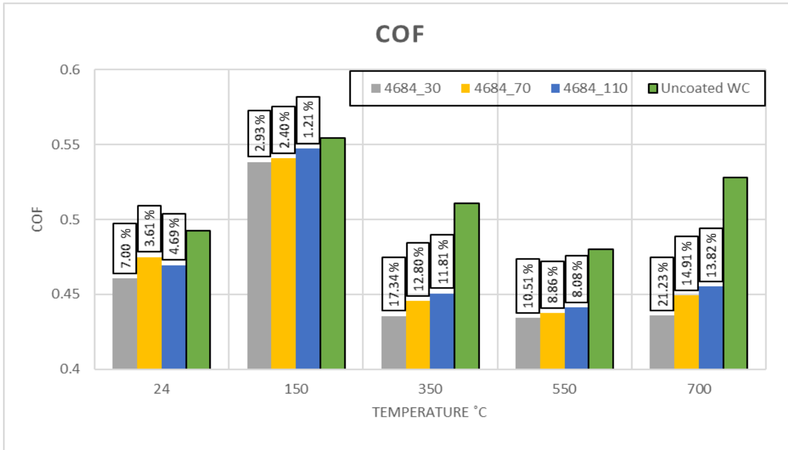

Figure 4-22- Coefficient of friction of coatings deposited with different bias voltage.

All coatings exhibit superior tribological performance than the uncoated pin. Increasing the temperature up to 150˚C caused a slight reduction in the coefficient of friction value for all the pins. As the temperature keeps increasing, the coefficient of friction continues to drop. However, the reduction of the COF is more significant in the coated samples. Figure 4-22 shows that the coefficient of friction significantly dropped in the coated pins at temperatures greater than 350˚C. The number in the box shows the percentage of COF reduction in each coating. At the highest temperature (700˚C) 4684_30 has the maximum reduction of COF and consequently the best tribological performance in this test.

Tribological behaviour of the coatings can be illustrated by shear and normal stress in each tribometer test. As it can be seen in Figure 4-21, increasing the temperature up to 150˚C causes the shear stress in all the pins to rise. This is due to the strengthening of the adhesion bonds between the pin and the workpiece material. However, shear stress for the coated pin increases less than the uncoated WC pin due to its less adhesion to the disk. At this temperature, the material would be softer and as a result, a larger imprint diameter will be generated at the same normal load. This will decrease the normal stress in all the pins at the given temperature. Higher shear stresses along with the lower normal stresses will cause a higher coefficient of friction in all pins. Since the adhesion of the steel is stronger to the uncoated WC than that of the AlTiN coating, the uncoated pin has a greater COF from the beginning.

Upon further increase, the temperature will form oxide layers on the top of the hard coatings [38]. The Aluminum oxide layers at higher temperatures will reduce the contact between the steel and the pin. In fact, the uncoated WC pin has direct contact with the surface of the steel, which will increase adhesion and shear stress in the tests. Scanning electron microscopy (SEM) and Energy-dispersive X-ray spectroscopy (EDS) was conducted to analyze the pin tips after each test. Figure 4-23 shows the SEM images of the 4684-110 pin tip. SEM images show plastic deformation in the 4684-110V coating. This can cause ploughing during friction and increase the COF. Additionally, there are some cracks on the surface of the coating which can come apart and cause delamination. In the Back-scattered image (left side) white areas show the presence of the adhered materials (steel) on the surface of the pin. Map analysis of the area confirms elements of the steel adhering on the pin tip. This coating has less adhered material and more crack and deformation on the surface.

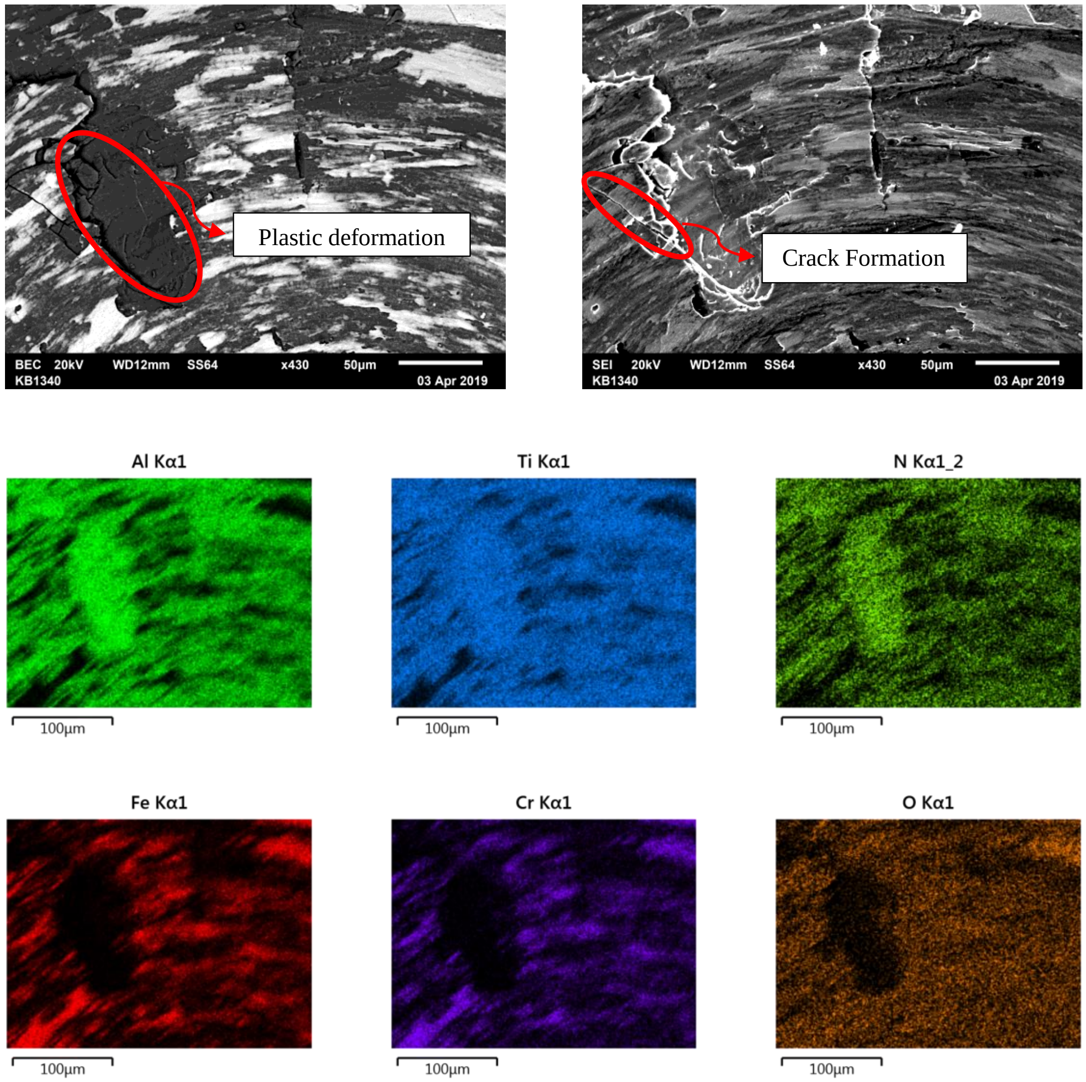

Figure 4-23- Back-scattered image, SE image and EDS analysis of the pin tip of 4684_110V.

As mentioned earlier, tribometer tests were carried out to observe the effect of nitrogen pressure during deposition on the tribological behaviour of the coating. Figure 4-24 shows the normal stress, shear stress and coefficient of friction for the coated and uncoated pins.

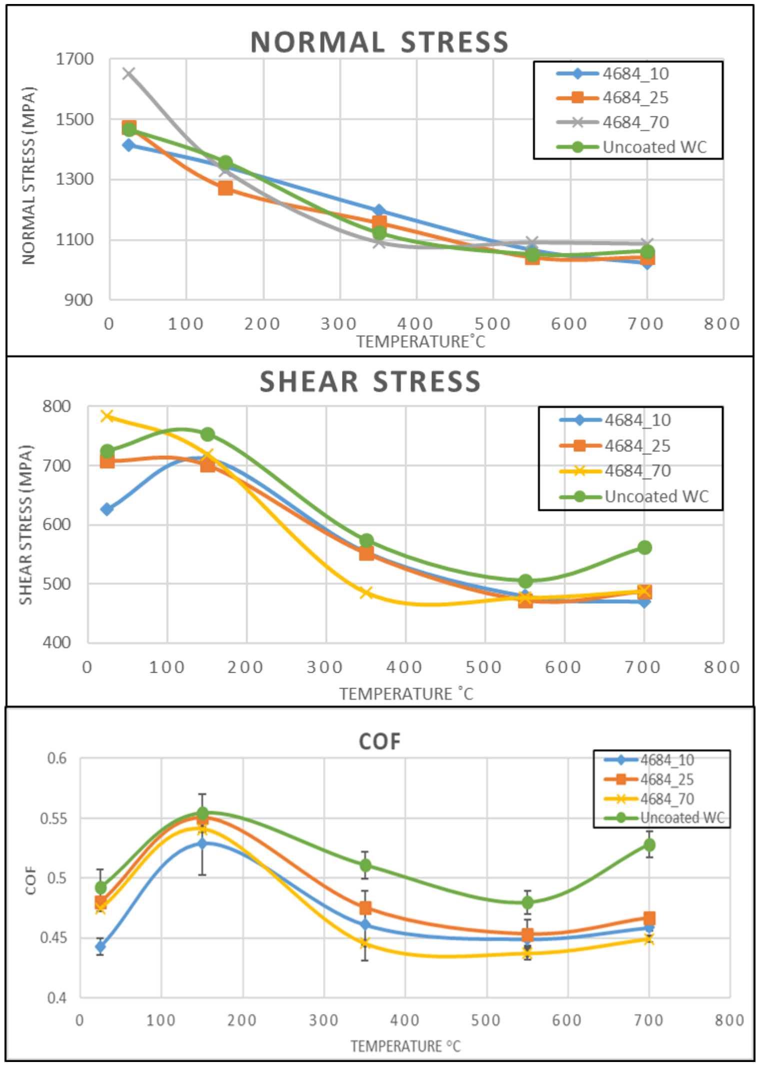

Figure 4-24- Effect of Nitrogen pressure on normal stress, shear stress and coefficient of friction of deposited coatings.

External friction threshold (ζ) was checked for the tests. All the tests were conducted in the external friction condition. The COF values in the tests are plotted in the column figure. The percentage reduction of COF over the uncoated tool is also included in the figure to highlight the tribological behaviour of the coated pins with the uncoated ones.

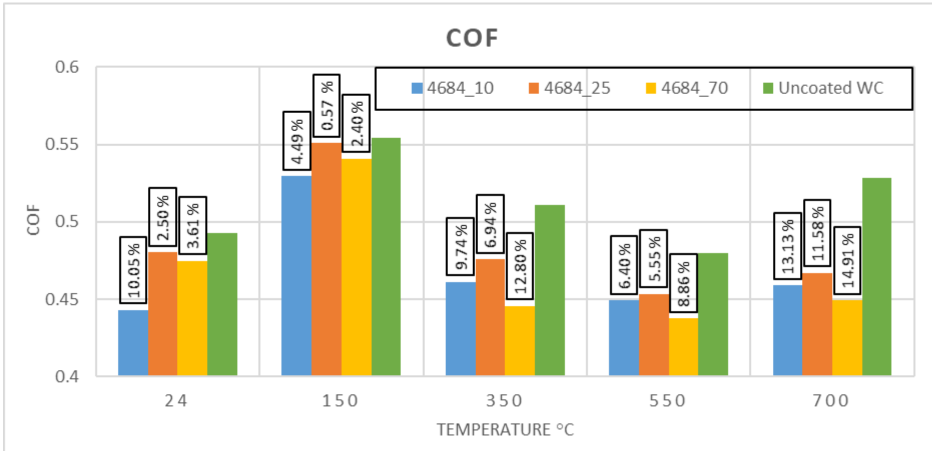

Figure 4-25- Coefficient of friction of coatings deposited with different Nitrogen pressure.

Figure 4-25 shows that the maximum improvement of the tribological performance of the coatings is 4684_70 at high-temperature tests. It amounts to a reduction of about 15% at 700 ˚C compared to the uncoated pin. 4684_ 10 is the next best performing coating in the tests.

As can be seen in Table 4-6, nitrogen pressure also changes the properties of the coatings. Figure 4-24 shows that coated samples have a smaller coefficient of friction than the uncoated pin, especially at high temperatures, which was explained earlier. It's noteworthy to mention that hot hardness retention at high temperatures can also help to improve tribological behaviour and reduce friction under high-temperature tests. In Figure 4-24 the coating deposited at the highest nitrogen pressure has a better tribological performance at high temperature. The effect of roughness is negligible in this test because all the pins were polished before the test was performed.

The 4684_25 coating has the worst performance out of all tested. SEM and EDS analysis was carried out to assess why. Figure 4-26 presents the center of the pin tip. The coating plastically deformed at the center of the tip due to high normal load and in some areas tungsten carbide became exposed to the air. The back-scattered image (left side) shows WC as a bright and shiny colour between the black coating. Moreover, EDS analysis confirms the presence of WC. Layers of adhered steel are present further from the center, toward the pin tip edges. Map image of the pin clearly illustrates the presence of Fe and Cr, which are elements of the steel, as well as oxygen signals due to the oxidation of steel and aluminum on the surface.

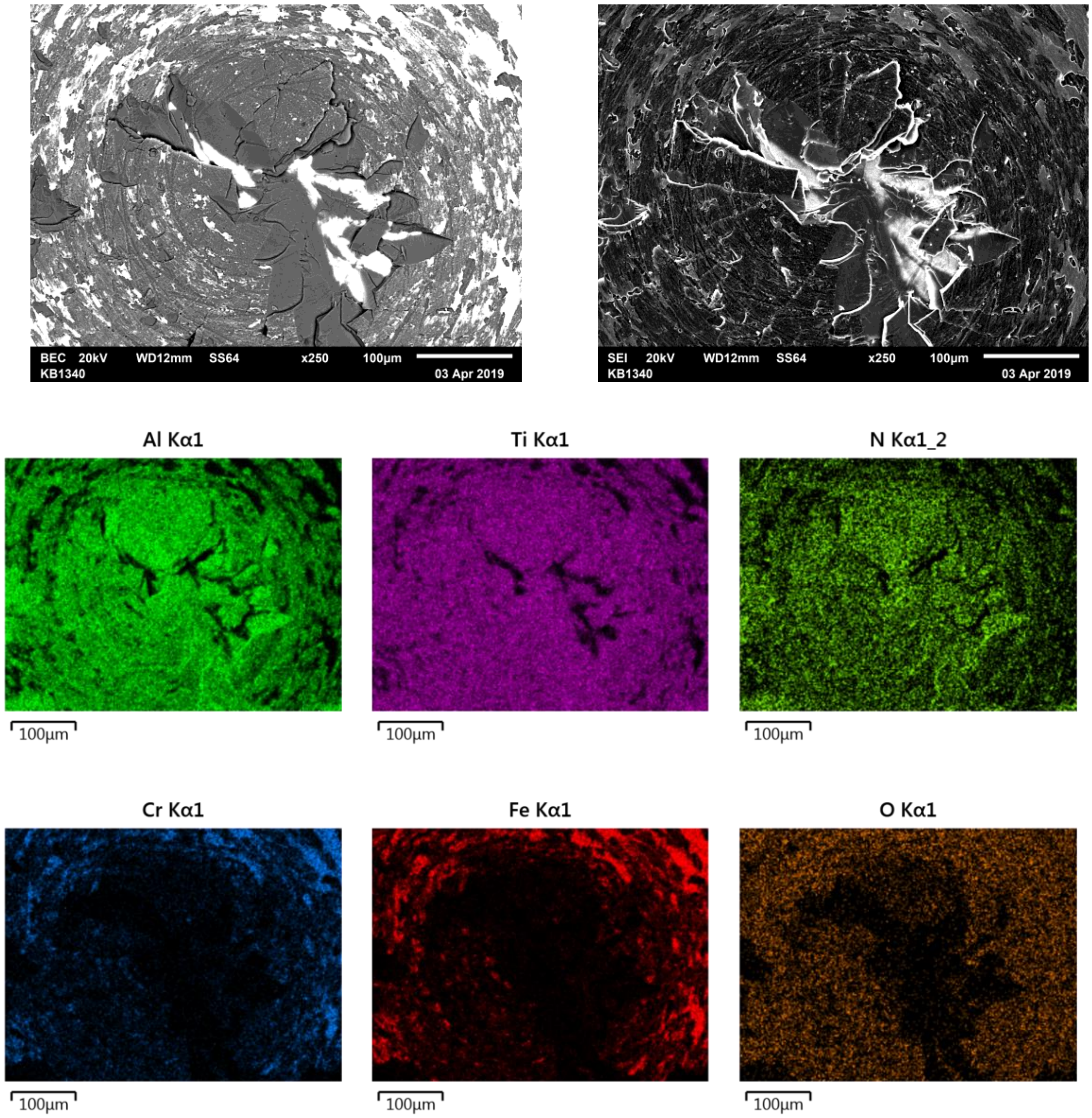

Figure 4-26- SEM and Map analysis of 4684-25.

The effect of bias voltage and nitrogen pressure on the coating's coefficient of friction can be indicated by the COF changes of all the coatings in Figure 4-27.

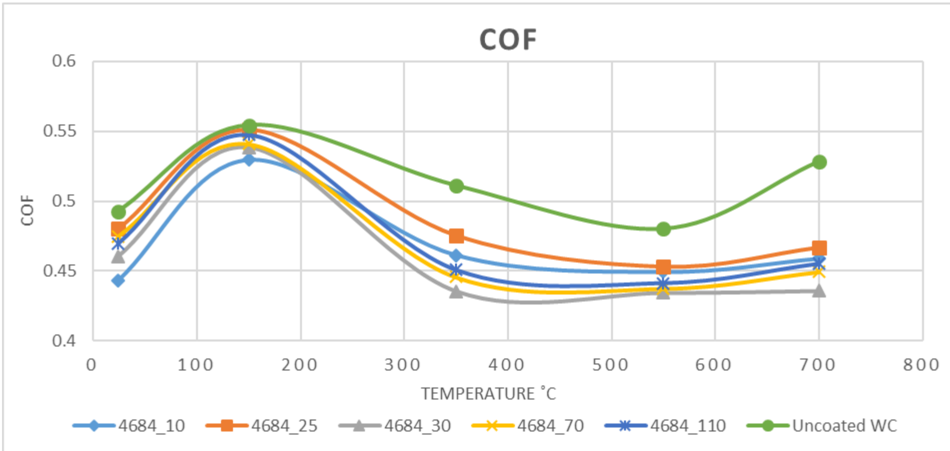

Figure 4-27- Effect of the substrate bias voltage and Nitrogen pressure on COF values.

This graph shows that Al-Ti-N coatings improved the COF value, especially at high temperatures thanks to the formation of a protective a Al2O3 layer [38]. All the coatings deposited at the same nitrogen pressure (highest pressure) performed better than the coatings which were deposited at a lower Nitrogen pressure (low and medium). The 4684-30 coating was observed to have the best tribological performance. This coating has a minimum thickness between all the coatings. The lower thickness of this coating results in a smaller imprint diameter and as a consequence, a higher normal stress. As such, the coefficient of friction will be smaller. More bias voltage on the substrate will increase the titanium content in the coating. 4684_30 has less titanium and more aluminum. A greater amount of aluminum will help the coating to retain its hardness at a high temperature. More aluminum will generate a continuous layer of Al2O3, which will protect the coating from the oxidation [38].

In conclusion, it should be mentioned that increasing the nitrogen pressure will decrease the coefficient of friction. Thus, the best tribological performance was observed under the highest nitrogen pressure. Results from the tribometer test show that increasing the substrate bias voltage from the lowest to the highest level increases the coefficient of friction for the coated pins. Therefore, the coating which was deposited in the highest nitrogen pressure and the lowest bias voltage was observed to have the best tribological performance.

4.4 Effect of the chemical composition of coatings on their tribological performance

All coatings used in previous sections were hard nitride coatings with a high hardness and oxidation resistance at high temperatures. The nature of the bonds between elements in the ceramic coatings provided excellent resistance to wear and corrosion.

In this section, pure metal coatings were deposited to assess their tribological performance under a heavy-load and high-temperature condition. All the coatings were deposited in an Argon atmosphere and no Nitrogen was injected into the chamber. Three chemical compositions were selected for deposition on the pin: Pure titanium, Ti-Al (50:50) and Ti-Al (40:60). Deposition time for all the coatings was 30 minutes. The substrate bias voltage was 50 V and the pressure of the Argon gas in the chamber was 2.7 Pascal. The following table shows the coating code as well as their deposition parameters.

Table 4-7- Coating deposition parameters for metal coatings

Coating Code	Ti %	Al%	Deposition time	Bias voltage	Argon Pressure
TA 5530	50	50	30 minutes	50 V	2.7 Pa
TA4630	40	60	30 minutes	50 V	2.7 Pa
Ti30	100	0	30 minutes	50 V	2.7 Pa

Tribometer tests were performed to evaluate the frictional behaviour of the coatings. A load of 500 N was selected since the coatings have a lower hardness. Five different temperatures of 25, 150, 350, 600 and 750˚C were selected to perform the tests. The coefficient of friction of each test is reported in Figure **4-28**.

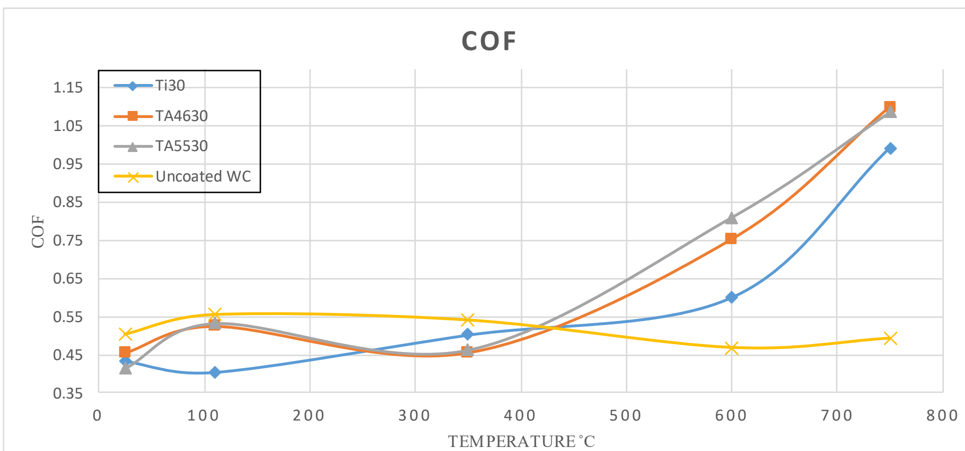

Figure 4-28- **Coefficient of friction for metal coatings.**

As can be seen in the graph, all coated samples had better performance than the uncoated pin till 350˚C. The pure Titanium coating had the best performance at the low temperatures, below 350˚C. Beyond that point, all coatings perform worse than an uncoated pin. To investigate the reason for this, SEM and EDS analysis were conducted on all the pins and imprints on the disks. The following figure shows the EDS analysis of the imprints after first tribometer tests at room temperature. SEM and EDS analysis was carried out on the pin tip after doing all the tests.

EDS analysis demonstrated that all of the coatings detached and adhered to the surface of the workpiece material. In Ti 30, the side imprint walls have a thick layer of Titanium. TA4630 had more Aluminum and Titanium on the outer diameter, but a certain amount of coating material adhered to the central parts of the imprint. TA5530 has a thick ring of Aluminum and Titanium on the side of the imprint.

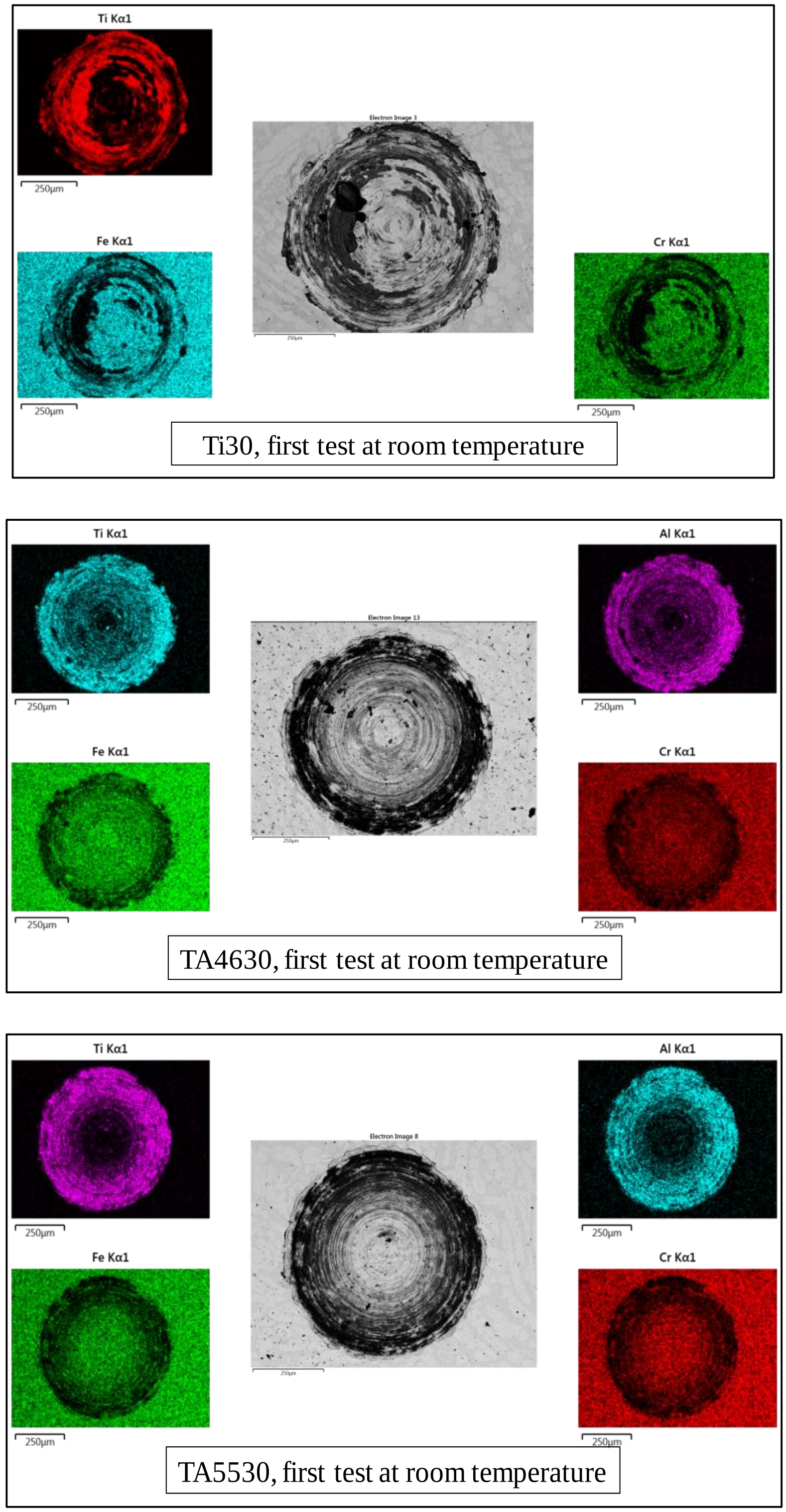

Figure 4-29- SEM and EDS analysis of imprint on the disks after the first test.

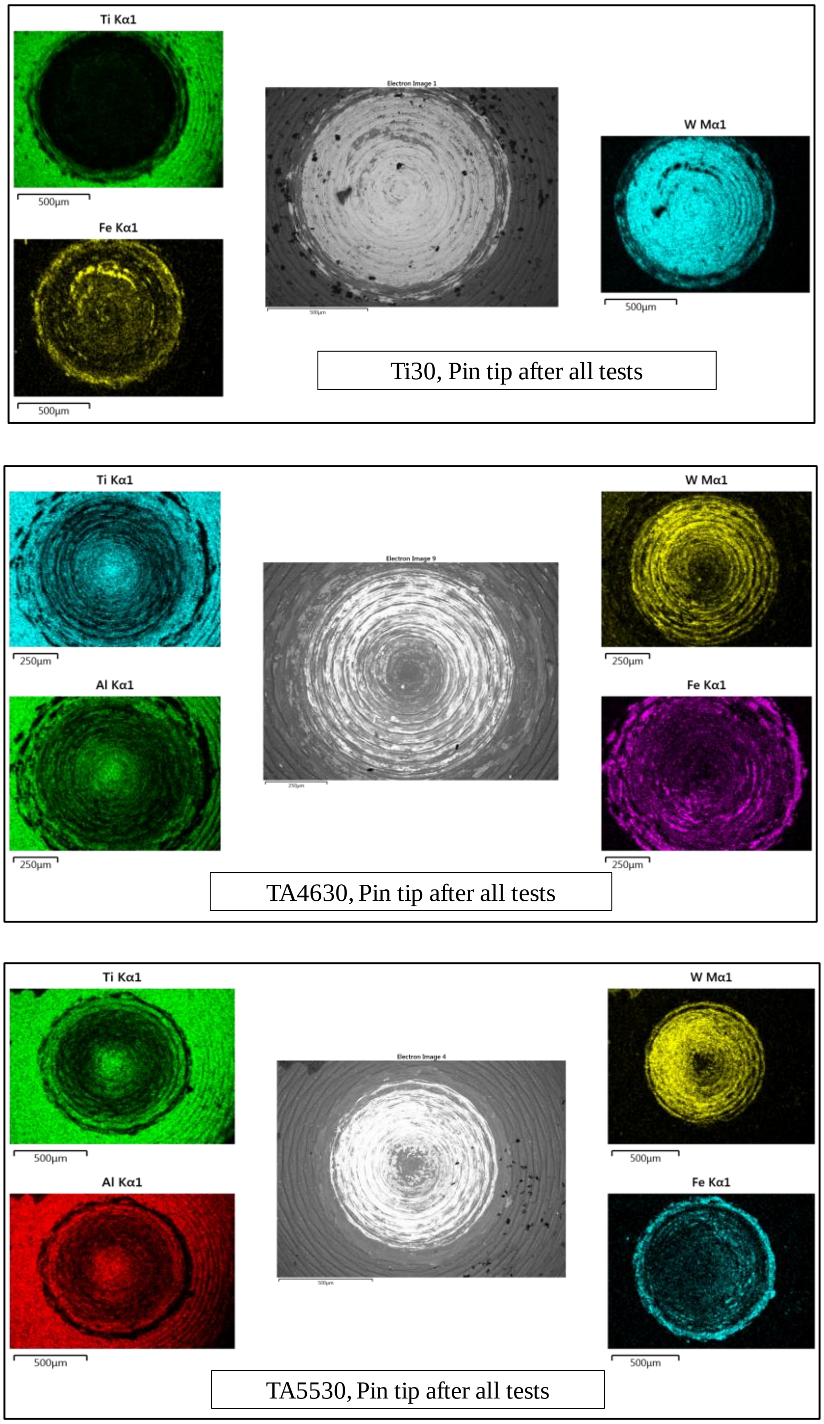

Figure 4-30- SEM images and EDS analysis of the pin tips.

In the Ti30 pin tip the entire coating was detached from the pin surface. WC and some adhered steel material was present on the surface of the pin. For the TA4630 pin some Aluminum and Titanium material was adhered to the center of the tip. WC signals showed that the substrate was exposed to air. TA5530 had a thin ring of Aluminum and Titanium on the surface. In this pin, a greater amount of WC was exposed to air.

As explained partial and complete coating detachment caused the non-uniform coating on the pin tip. As a result, direct contact between the pin and workpiece happened. In addition to that the non-uniform coating caused ploughing in the contact zone and increased the coefficient of friction significantly. This phenomenon plastically deformed the disk material and caused the high values measured for the coefficient of friction.

5 Machining experiments and correlations to Tribometer tests

5.1 Introduction

First, it was needed to ensure that the heavy-load high-temperature tribometer was functioning properly, by comparing the performance of the published data and conducting different tests on various PVD coatings.

If the tribometer results were to be related to coating performance, actual machining was required. In this section, the threading process of super duplex stainless steel was studied using three coatings. Forces were measured during machining and chip analysis was conducted. All results were compared with the tribometer findings and the tribological behaviour of the coatings was correlated to the tribometer results.

5.2 Cutting tools, coatings and workpiece properties

The threading process of super duplex stainless steel was conducted using a turning machine in this study. A cutting insert of Vallourec Group with the model of VAM TOP 1059 VM25S-125 was selected for use in this study. The rake angle of the insert was 5˚.

Three different coatings from two coating companies were deposited on the tools by a physical vapour deposition process. An AlTiN-based BALIQ ALTINOS coating was deposited on the surface of all three tools. The coating has very high wear resistance even under temperatures at which the tools have high thermal impact. This coating is a hard ceramic coating that exhibits high hardness at high temperatures [39].

A hard monolayer TiB_2 coating, a product of Kyocera Hard-coating Technologies with hardness of 4000 HV and thickness of 3 microns was deposited on top of BALIQ ALTINOS in one of the tools. TiB_2 is a self-lubricating coating which can reduce friction during machining via the formation of liquid B_2O_3 tribo-oxides [40].

BALINIT C from Blazers was deposited on BALIQ ALTINOS for the other tool. BALINIT C is a WC coating which is deposited in a carbon atmosphere. This coating can significantly reduce adhesive wear and the coefficient of friction. WC/C is a self-lubricating coating and the formation of solid W-O tribo-oxides such as WO_3 will make the coating a suitable choice for dry sliding conditions [40].

The following table shows the coatings which were deposited for the machining study:

Table 5-1- Tools which were used for threading

Tool Code	Coating Name	Composition
T-0	Uncoated	____
T-1	BALIQ ALTINOS	AlTiN Based
T-2	ALTINOS+ TiB_2	ALTINOS+ TiB_2
T-3	ALTINOS+ BALINIT C	ALTINOS+ WC/C

The same coatings were deposited on the surface of WC-6% Co pins in order to perform the heavy-load high-temperature tribometer test.

Highly alloyed stainless steels are widely being used in industry due to their excellent mechanical properties and high corrosion resistance. The presence of different alloying elements, with excellent mechanical properties and a dual phase microstructure, make them difficult to cut materials. In this study, SAF 2507 super duplex stainless (ASTM A459 S32750) was selected as the workpiece material. Cylindrical tubes of this material were prepared for the threading process. The high chromium content of this material (25%) makes it different from standard duplex stainless steels which have about 20% chromium. This alloy has an equal amount of austenite (50%) and ferrite (50%) [41]. Table 5-2 shows its chemical composition and mechanical properties [42]:

Table 5-2- Chemical composition and mechanical properties of S32750

Chemical composition										
Element	C	Si	Mn	P	S	Cr	Ni	Mo	N	Fe
Wt%	0.03	0.8	1.2	0.035	0.02	25	7	4	0.24	Remaining
Mechanical Properties										
Yield Strength (Mpa)			Ultimate tensile strength (Mpa)			Elongation			Hardness (HRC)	
550			800-1000			15			32	

5.3 Experimental set up for cutting and cutting parameters

A Nakamura-Tome SC-450 CNC lathe was used to perform threading tests. The spindle speed in this machine is between 25-2500RPM. Spindle torque can go up to 856Nm and the maximum spindle output is 30kW.

An OP.5.917 Fecial tool holder (left-hand tool) was selected to set up the tools. Figure 5-1 shows the dimensions of the tool holder used for the turning process.

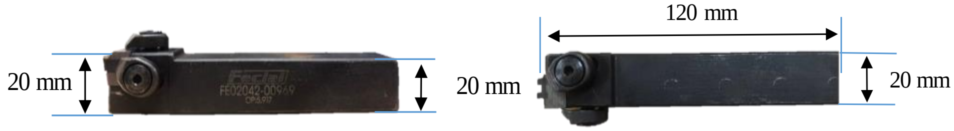

Figure 5-1- OP.5.917 Fecial tool holder.

A dynamometer was installed on the machine to measure the cutting forces. A type 9129AA Kistler dynamometer was used in this study. A LabAmp Type 5167A charge amplifier was utilized to amplify the measured force signals and all the data from the force measurement unit was analyzed using DynoWare Type 2825D-03 software. Figure 5-2 shows the dynamometer and the cutting setup in this study.

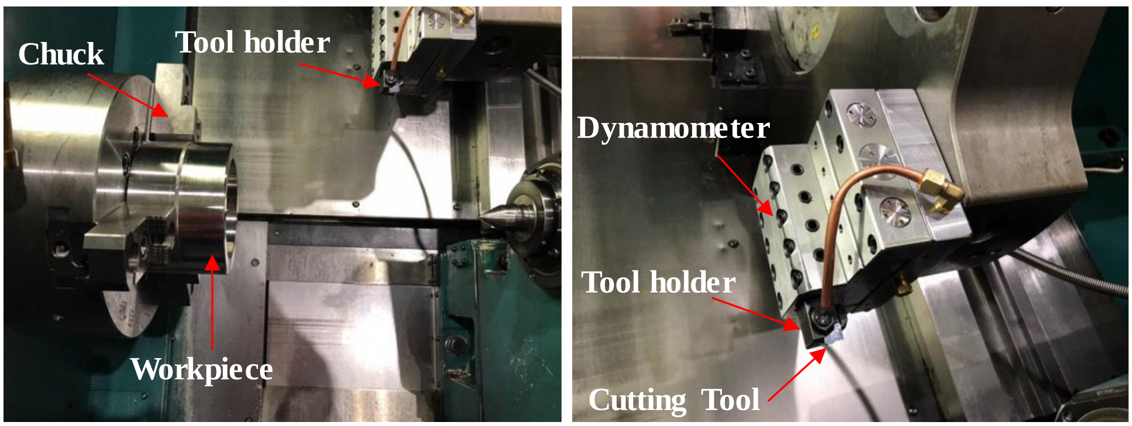

Figure 5-2- Cutting setup and dynamometer for threading.

In this study the cutting parameters were chosen to have low cutting speed, low depth of cut and high feed rate during the threading process. The maximum height for each thread was 1.78 mm. The threads were made in 10 passes. The cutting speed was 70 m/min and feed rate 5.08 mm/rev in all passes. Three different depths of cut were considered for the threading passes. The depth of cut for the first 7 steps was 0.237 mm. Step 8 has a depth of cut of 0.08 mm and the depth of cut for the last two steps (8 and 9) was 0.018 mm. The cutting parameters for the threading process are shown in the following table.

Table 5-3- Cutting parameters for threading of super duplex stainless steel

Pass Number	Cutting speed	Depth of Cutting	Feed rate
1 to 7	70 m/min	0.237 mm	5.08 mm/Rev
8	70 m/min	0.08 mm	5.08 mm/Rev
9 and 10	70 m/min	0.018 mm	5.08 mm/Rev

Forces were measured for all passes and a chip sample was collected after the first step of each test.

5.4 Coating Analysis

5.4.1 The thickness of the coatings and coating structure

All the inserts were cut and investigated using Scanning Electron microscopy to measure thickness and study the coating structure. A back-scattered image and secondary images were taken for this purpose. Coating chemical composition was analyzed with an EDS Map.

5.4.2 Nano hardness test

Hardness and elastic modulus of the coatings as well as the uncoated tools were evaluated with an instrumental indentation. An Anton Paar nano-indentation tester was used for the tests. This machine can apply loads ranging from 0.1 to 500mN. Depth of penetration is being controlled and measured during the tests and the final hardness value is being calculated based on the applied load and the imprint geometry.

All inserts glued in the sample holder. Tests were performed with a load of 50mN and with dwell time of 10 seconds. Each coating underwent 15 tests, with the mean value of the hardness and elastic modulus being recorded. This load was selected to make sure that the depth of penetration did not exceed 10% of the coating's thickness to avoid any influence of the sub-substrate on the coating's properties.

5.5 Tool analysis

5.5.1 Machining force measurement and tool wear analysis

Cutting forces were measured in all the passes with a Kistler type 9129AA dynamometer.

Images of the flank and rake faces of the tools were taken using a Keyence VHX Digital microscope, after 10 threading passes. Wear mechanisms and tribological performance of the coatings were evaluated using machining forces and wear analysis images.

5.5.2 SEM and EDS analysis of the tools

Scanning Electron microscopy was used to have a deeper understanding of tool wear mechanisms. Energy-dispersive X-ray spectroscopy (EDS) was also utilized to study adhered materials on the tool tip.

5.6 Chip analysis

5.6.1 The roughness of the chips

Alicona 3D measurement microscope was used to study the roughness of the chips after machining. Chips from the first machining pass were collected. After the first pass, other parameters such as a change in tool geometry or workpiece material microstructure can affect the tribological performance of the coatings.

Chips from four inserts were scanned and roughness was measured at 5 areas. Figure 5-3 shows the scanned surfaces and the roughness measurements of the chips.

Tool	3D image of threads	Chip roughness
Uncoated	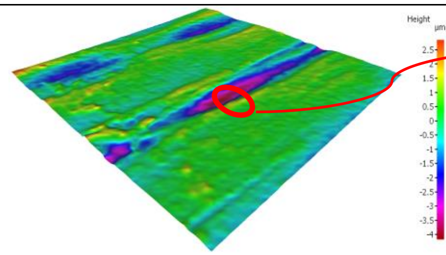	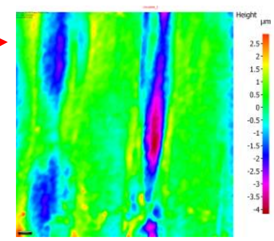
AlTiNOS	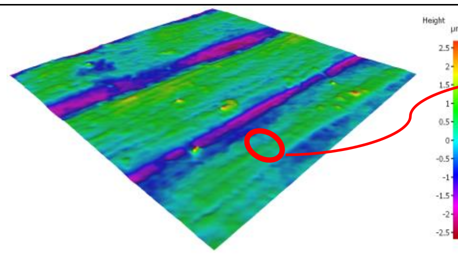	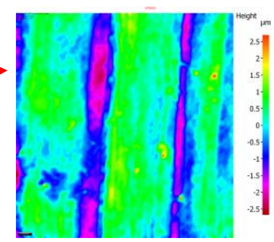
AlTiNOS + TiB2	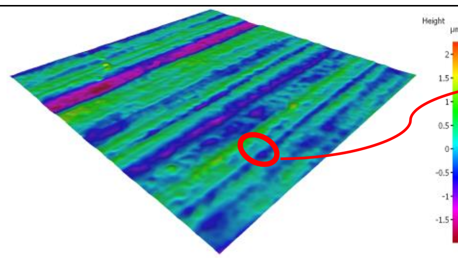	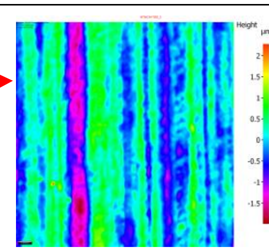
AlTiNOS + WC/C	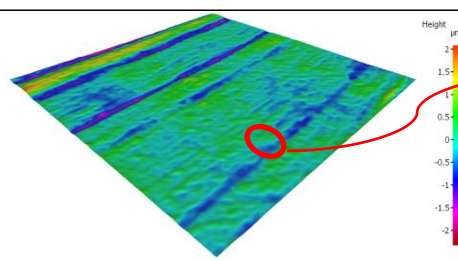	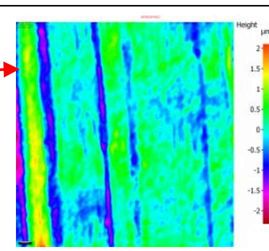

Figure 5-3- Scanned surface and roughness measurement of the chips.

5.6.2 Chip cross-section and chip thickness ratio analysis

A cross section of the chips was ground and polished with SiC sand papers to observe the structure. All samples were etched with a Beraha reagent. Images were taken using the Keyence High-Quality Digital Microscope model VHX-S660E.

The thickness of the chips was measured in 10 different areas and the average values were reported. The chip compression ratio was experimentally evaluated in the next step. These parameters give a clear understanding of the frictional behaviour of the tools during the cutting process.

Thickness of the chips was measured after machining to get the chip thickness ratio, which is the value of uncut chip thickness divided by chip thickness after the cut [5]:

$$r = \frac{t}{t_c} \qquad (5\text{-}1)$$

In this equation t_c is the thickness of the deformed chip and d is the depth of cut in the machining process. Chip thickness ratio is always less than 1 $(r < 1)$ due to deformation. A greater value of the chip thickness ratio indicates a higher shear angle, which means that less shear stress was required to plastically deform the material.

5.6.3 Shear angle, chip velocity and coefficient of friction on the chip

The chip thickness ratio (r) was used to calculate the chip shear angle (φ) from the following equation [5]:

$$\tan\varphi = \frac{r\ \cos(\alpha)}{1 - r\sin(\alpha)} \qquad (5\text{-}2)$$

In the equation 5-2, r is the chip thickness ratio and α is the tool's rake angle.

As explained earlier, a higher chip thickness ratio indicates the presence of plastic deformation on a smaller shear plane and less shear stress is needed to deform the chip.

Chip velocity can also be measured using the chip thickness ratio, given the following expression:

$$Vc = Vr \tag{5-3}$$

where Vc is the chip velocity, V is cutting velocity and r is the chip thickness ratio.

All the forces during machining were calculated using the dynamometer. The average value of the coefficient of friction can be calculated during machining using a ratio of the tangential load over the normal load on the chip. Merchant's model yields the coefficient of friction during machining [5].

$$\mu = tan\,\beta = \ tan\,(\frac{\pi}{2} + \alpha - 2\varphi) = \frac{F_c}{N_c} = \frac{F_Q \cos\alpha + \ F_p \sin\alpha}{F_p \cos\alpha - \ F_Q \sin\alpha} \tag{5-4}$$

Analysis of chip thickness ratio, shear angle and coefficient of friction can encapsulate the overall tribological performance of the coating during machining and evaluate the results from the tribometer.

5.6.4 SEM analysis of the chips

Chip curliness and under surface morphology was analyzed using Scanning Electron Microscopy JEOL6610LV. The chip undersurface morphology shows the chip flow and surface roughness. A smoother chip undersurface and a smaller stick-slip area indicates better tribological performance of the tools. Biksa et al. [43] reported that curlier chips exhibit less friction and wear during machining. Therefore, studying chip curliness and chip under surface can be a reasonable indication of the tribological behaviour of the coatings.

5.7 Friction Analysis using heavy load high-temperature tribometer

Coatings were deposited on four prepared WC-6% Co pins. Disks from the same workpiece materials were cut, ground and polished. A force of 200N was selected for tribometer tests, which were conducted at 25, 300, 500, 700 and 850˚C. Each test was repeated 3 times and the average value of torque, normal load and temperature was recorded. The diameter of imprints was measured with an Alicona 3D measurement microscope on a surface reference plane 3 times. The coefficient of friction was derived from the measured torque signal, normal load and the imprint size.

5.8 Results and discussion

5.8.1 Coating analysis

To interpret the tribological performance of the coatings, it is necessary to first characterize them. Coating thickness and hardness are two factors which directly affect their performance. Scanning electron microscopy and EDS Map analysis was used to measure coating thickness and observe their structure. Figure 5-4 shows the measured thickness and Map analysis for the coatings. The average thickness values of the coatings after three measurements are reported in Table 5-4.

Table 5-4- Average value of the coatings thickness

Coating Name	AlTiNOS	AlTiNOS+ WC/C		AlTiNOS+ TiB2	
	AlTiNOS	AlTiNOS	WC/C	AlTiNOS	TiB2
Thickness (μ)	4.656333	4.856	2.755	5.6665	3.0015

AlTiN

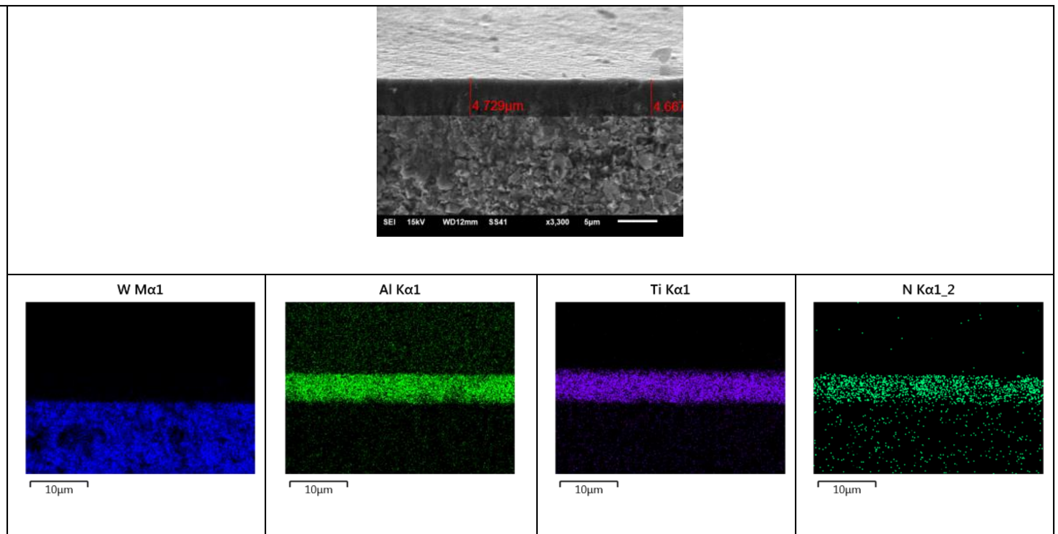

AlTiN

+

WCC

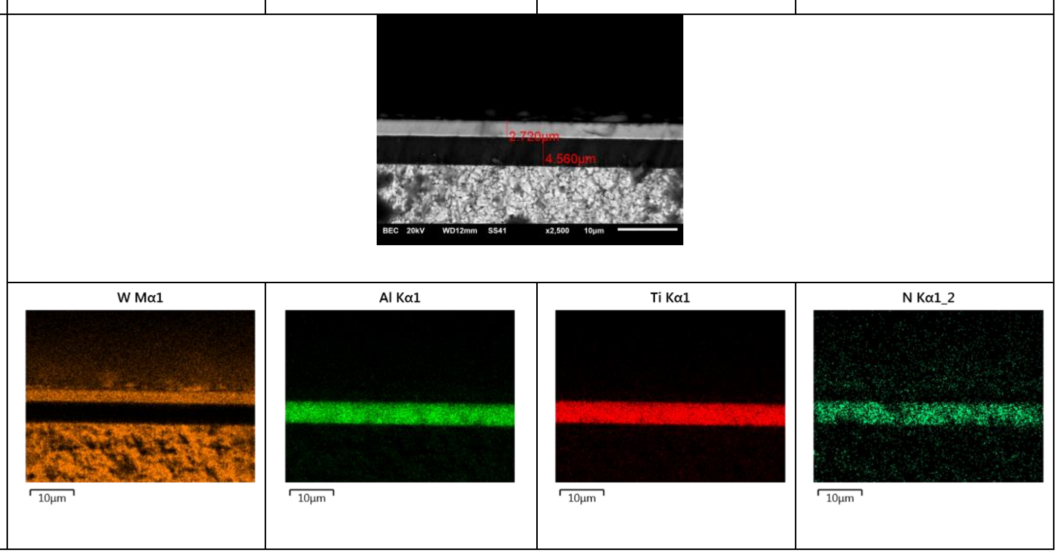

<table>
<tr><td rowspan="2">AlTiN
+
TiB2</td><td colspan="4">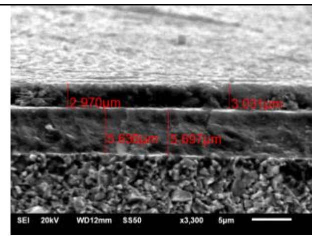</td></tr>
<tr><td>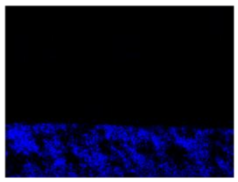</td><td>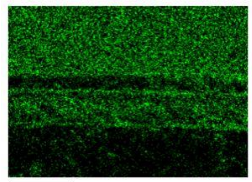</td><td></td><td></td></tr>
</table>

Figure 5-4- Thickness measurement and Map analysis of the coatings.

As can be seen in Figure 5-4 AlTiNOS has a thickness of about 5 microns. The thickness of WC/C and TiB2 on top of AlTiNOS is about 3 microns. The structure of AlTiNOS is columnar. However, WC/C has a less columnar structure. The structure of the coating is directly linked to its mechanical properties with a more columnar structure found to improve the mechanical properties of the coating.

Hardness and elastic modulus of the coatings are measured and reported. Figure 5-5 shows the hardness and elastic modulus values of the coatings.

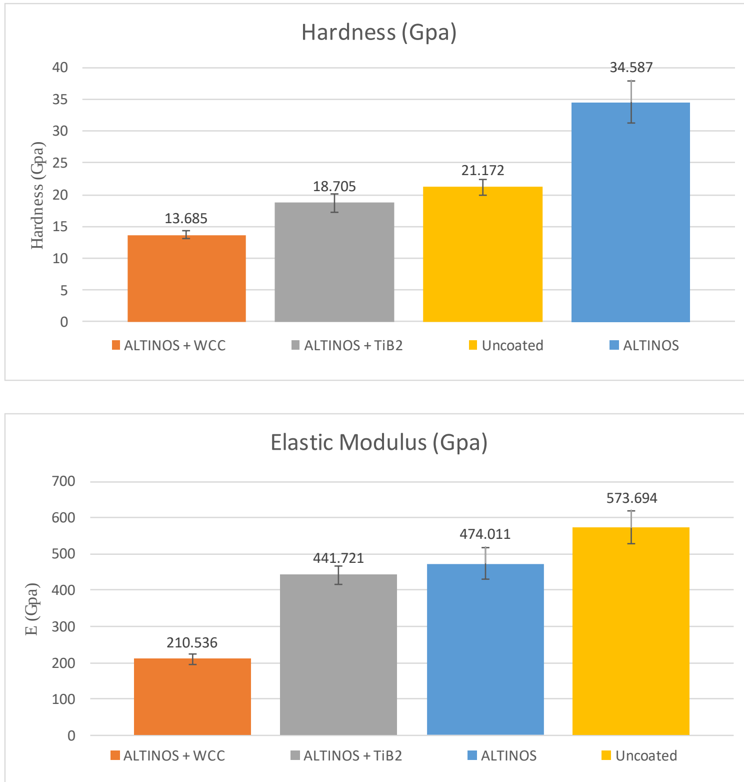

Figure 5-5- Hardness and elastic modulus values for the coatings.

As it can be seen in Figure 5-5 AlTiNOS had the maximum hardness value between the coatings. AlTiNOS+ TiB2 had the second-best hardness and AlTiNOS+ WC/C had the minimum hardness among the coatings. In conclusion, AlTiNOS is the hardest film with the highest elastic modulus. AlTiNOS+ TiB2 had a good combination of hardness and elastic modulus. The low hardness and elastic modulus of the WC/C coating can cause coating deformation and delamination.

5.8.2 Friction Analysis using a heavy-load high-temperature tribometer

A heavy-load high-temperature tribometer was used to analyze the tribological behaviour of the coatings. Coefficient of friction, normal and shear stresses of the coatings were studied in this section and wear mechanisms explained using Scanning Electron Microscopy and EDS analysis.

Figure 5-6 represents the coefficient of friction, normal and shear stresses for the coated and uncoated pins. Imprint diameters were taken to assess normal and shear stresses during the test. Figure 5-7 shows the imprints diameter measured after the tests.

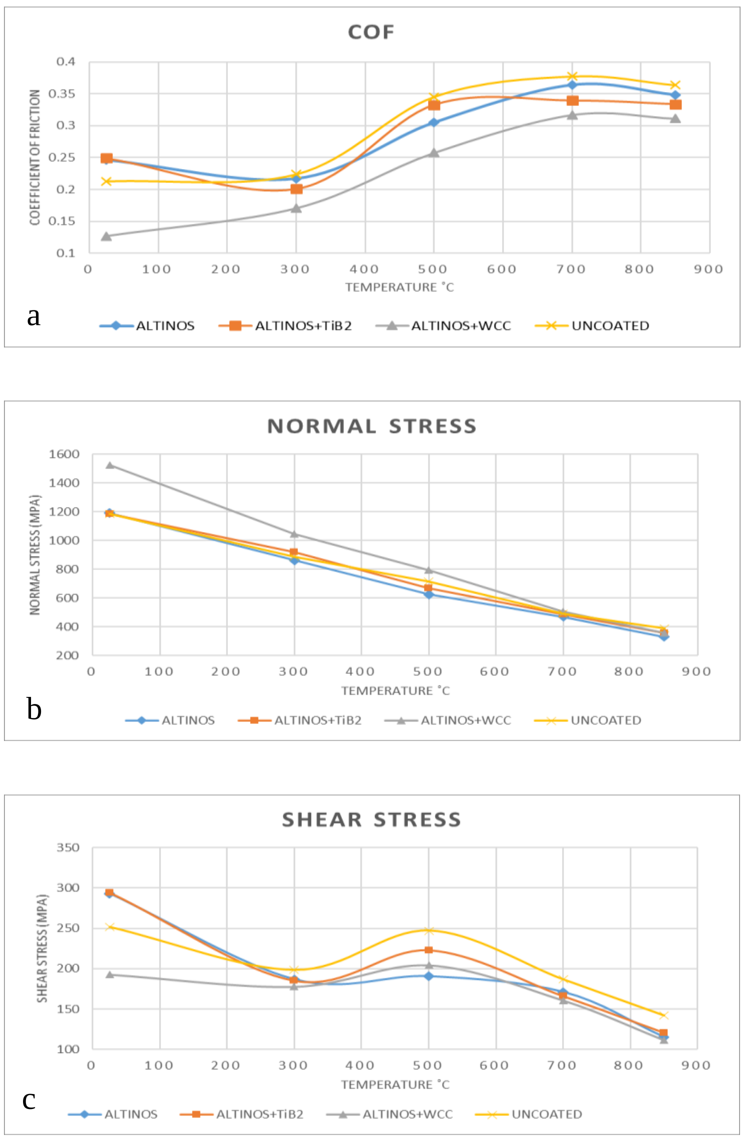

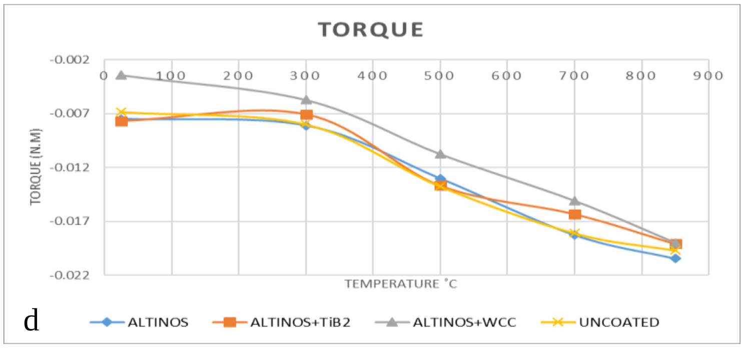

Figure 5-6- a) COF, b) normal, c) shear stresses and d)reaction torque for the coated and uncoated pins.

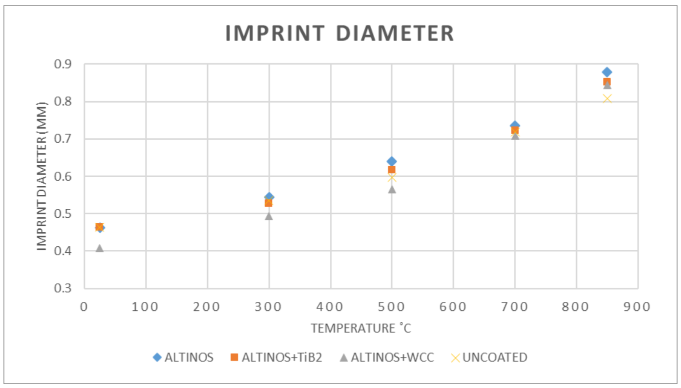

Figure 5-7-Imprints diameter of the coatings after each test.

The tests were conducted at five different temperatures. At room temperature, AlTiNOS + WCC showed the minimum coefficient of friction. At room temperature, the value of COF for AlTiNOS and AlTiNOS +TiB2 was higher than that of the uncoated and AlTiNOS + WC/C pins. As can be seen in Figure 5-7, the imprint diameter of AlTiNOS+ WC/C pin was lower than the other three pins at all temperatures except the last. Under the same normal stress, the lower hardness of this coating (Figure 5-5) caused higher plastic deformation on the surface of the film. Plastic deformation of the coating reduced the deformation of the workpiece material. As a result, a smaller imprint diameter was formed under the same normal load, which increased the normal stress on the surface of this coating. In addition to that, a lower shear stress resulted from the lubricity of the soft coating which reduced the coefficient of friction. In fact, a combination of a higher normal stress and lower shear stress caused a very low COF for this coating.

In tests at higher temperatures, the material will soften because of the heat generated in the contact zone. Therefore, at the same normal load, the imprint size will be larger, resulting in a lower normal stress. The normal stress of the tests for all the pins beginning from 1200MPa is about 2.5 times higher than the yield stress of the disk. Increasing the temperature will decrease the yield strength of the material, so that at higher temperatures, the normal stress on the contact zone would be higher than the yield stress of the material.

From Figure 5-6 (d) it can be seen that the reaction torque signal increased when going from the room temperature to the higher temperatures. However, from the room temperature to 300˚C the torque values are not increasing significantly but the imprints diameters were observed to increase. From Equation (3-15) it is known that the shear stress is a function of the third power of the imprint diameter. Therefore, the diameter size will have more effect on the shear stress value and the shear stress will decrease at 300˚C. The absolute value of the torque at 500˚C increased significantly while the imprint diameter increased with the same rate. The much higher torque value caused higher shear stress.

For temperatures higher than 500˚C the formation of liquid B_2O_3 tribofilm [40] decreased the shear stress for AlTiNOS+TiB_2 film. This phenomenon avoids any rise in the coefficient of friction. Shear stress of the uncoated pin was decreased which could be explained by material softening of the disk. However, the shear stress of the coated pins was lower than the uncoated pin at temperatures more than 500˚C.

In the AlTiNOS coating, the formation of Al_2O_3 protects the pin surface from further oxidation and slightly decreased the shear stress and coefficient of friction as compared to the uncoated pin [37].

SEM images and EDS Map analysis were conducted to further investigate coating performance under the tribometer test. Table 5-5 shows the general view of the pins and EDS analysis on the contact area after the last test at 850˚C.

Table 5-5- SEM and EDS analysis of the pins.

Uncoated	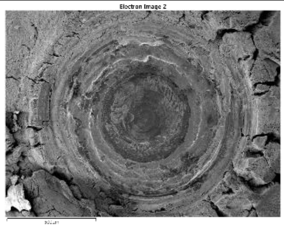	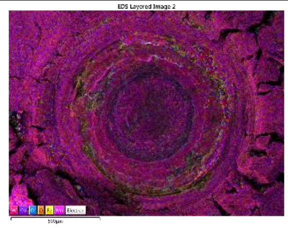		
W Mα1 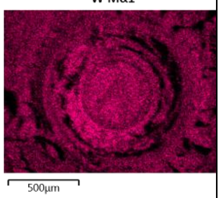	O Kα1 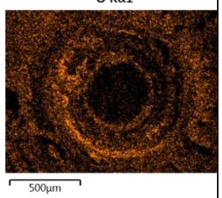	Fe Kα1 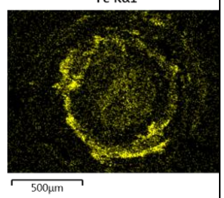	Cr Kα1 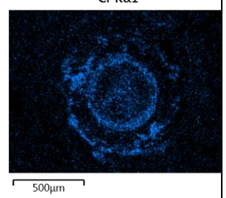	
AlTiNOS	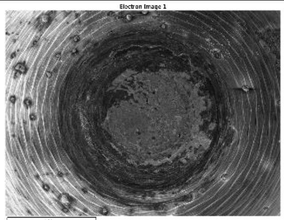	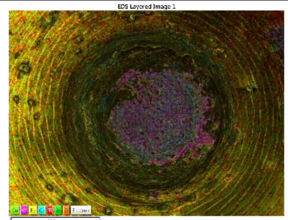		
W Mα1 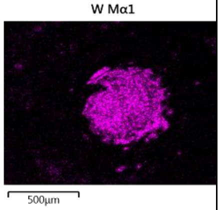	O Kα1 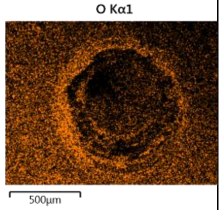	Fe Kα1 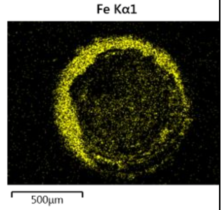	Al Kα1 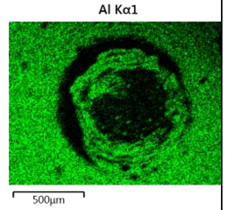	Ti Kα1 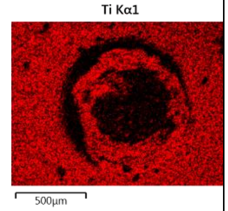
AlTiNOS + WC/C	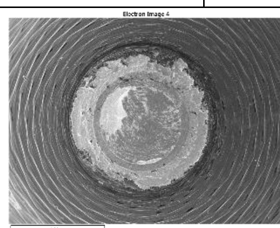	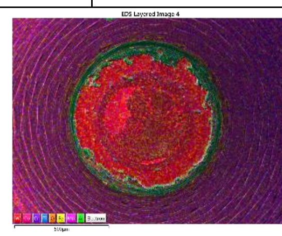		

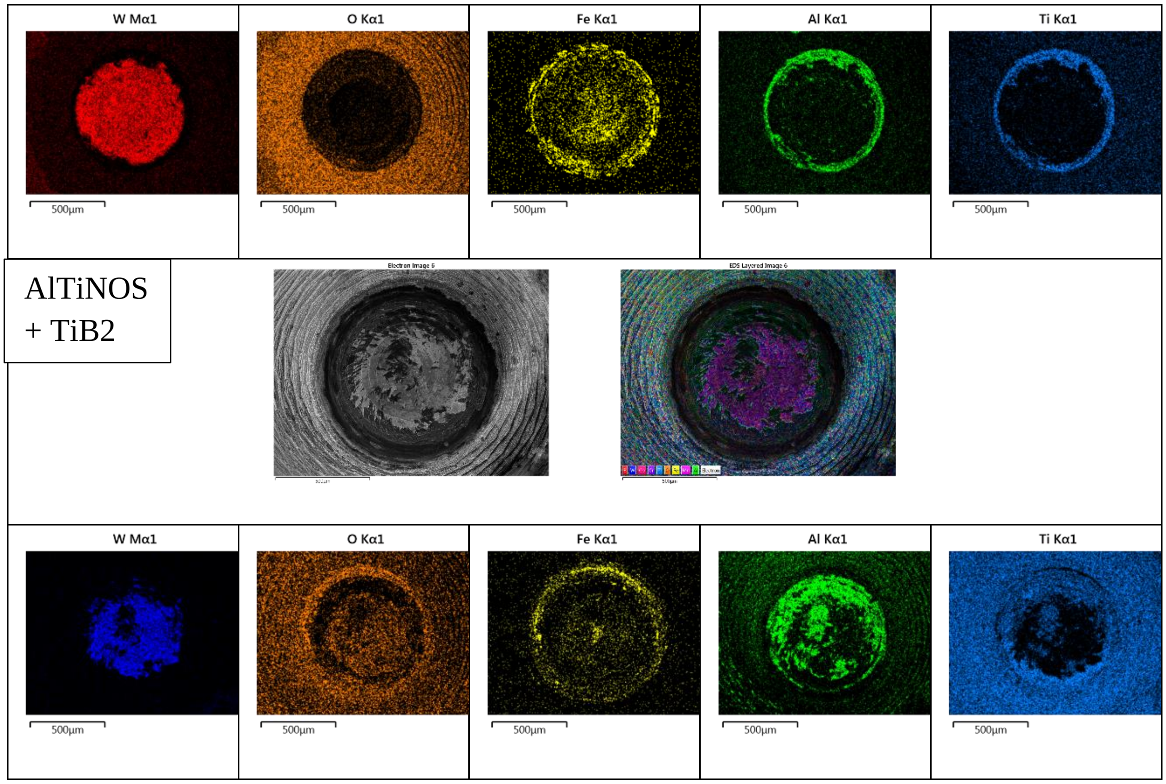

A small layer of workpiece material in the uncoated pin was observed to be adhered to the central part. More abrasion can be seen in the middle of the pin. From the center of the pin to the edges, there is a thicker layer of Chromium from the steel material that adhered to the surface. Iron signals indicate the presence of workpiece material on the surface.

The **AlTiNOS** coating was partially removed from the pin center. Aluminum and Titanium signals show the presence of the coating in most of the areas. At a distance from the centre, a layer of Iron adhered to the surface. The amount of adhered material was less than that for the uncoated pin and the Oxygen signals indicate oxidation of the adhered material on the surface. There was less adhesion in general and the coating protected the surface from abrasion.

Images for **AlTiNOS + WC/C** show that the WC/C layer was completely detached from the surface. In addition, AlTiNOS was removed but a small ring-shaped area of this coating remained on the surface. This image and EDS analysis were done after the last test at 850˚C. No images were taken after the tests performed at the lower temperatures. However, SEM images of the surface show less damage on the surface and less abrasion. There the layer of adhered material on the surface is less compared with AlTiNOS and the uncoated pin.

The **AlTiNOS + TiB2** images show far better wear performance. Less tungsten (W) on the surface was exposed to air. The AlTiNOS coating mostly remains on the pin tip and TiB2 removed only from the center of the pin. There was a very thin ring of adhered material indicating a better performance of this coating compared to other pins. Higher hardness of this coating than AlTiNOS+WC/C caused less damage to the surface and protected the surface from severe wear mechanisms.

According to the results of the coefficient of friction and SEM & EDS analysis, the following conclusions are drawn:

- AlTiNOS+ WC/C had the best tribological performance in terms of coefficient of friction. However, SEM and EDS results demonstrated coating detachment from the surface and a higher amount of adhered material than AlTiNOS+ TiB2.
- AlTiNOS+ TiB2 had the second best coefficient of friction at high temperatures. Out of all the coatings, this one showed superior wear resistance due to its higher hardness, elastic modulus and adhesion to the substrate.

- Between all the pins AlTiNOS+ TiB2 had the proper combination of lubricity and wear resistance. This coating is recommended for harsh machining conditions.

5.8.3 Machining force measurement and tool wear analysis

The tribological behaviour of three coatings during threading of super duplex stainless steel was compared that of the uncoated insert earlier in this study. The “running-in” stage has a significant role on the tribological performance of the insert. Therefore, machining forces were recorded during the first pass. After the first pass, other parameters such as a change in tool geometry and workpiece material properties can affect a tools performance. To evaluate the tool wear between pass two and ten, forces were measured and supported with microscope and SEM images. The following table shows the average of the forces for the first pass.

Table 5-6- Forces of machining after the first pass

Tools & Coaings	Pass 1 Forcess	
	Fx - Radial (N)	Fy - Tangential (N)
Uncoated	-657.8	1014
ALTINOS	-543	806
ALTINOS + WCC	-435.4	555.3
ALTINOS +TiB2	-526	635

As it can be seen in the table, forces generally reduced in the coated samples. Both radial and tangential forces dropped following the application of a coating. From a tribological viewpoint, the tangential force had a more important role in friction mechanisms. AlTiNOS+ WC/C coating has a minimum force of 555N for the SDSS threading process. This coating is relatively soft and can generate self-lubricating W-O tribo-oxides. The WC/C coating consists of WC grains in the matrix of amorphous carbon.

The lamellar structure of WC smoothens the surface in the contact zone [44]. The aforementioned structure and formation of W-O tribofilms reduce tangential force by approximately 55%.

The AlTiNoS+ TiB2 coating has the second lowest tangential and radial force. A force reduction of about 40% is seen in this coating. Due to high-temperature generation during stainless steel machining, the elements in the coating composition can oxidize and form tribo-oxides on the contact surface. As was mentioned before, B_2O_3 is a lubricious tribofilm which has a melting point of 450˚C. During the machining of Super Duplex stainless steel, the temperature greatly exceeds this amount. Therefore, the B_2O_3 tribo-oxide enters a liquid state and acts as a liquid lubricant to reduce the friction [45].

AlTiNOS also reduced the cutting forces because of the formation of solid lubricants of Al_2O_3 and TiO_2[37]. Al_2O_3 forms at a relatively high temperature. This tribo-oxide has a higher friction than B_2O_3 and WO_3 tribofilms. Therefore, less reduction of force was observed in AlTiNOS machining. However, this coating has good wear resistance especially against oxidation and diffusion due to the formation of alumina [37].

A coating's performance can change during machining from the running-in stage to the last pass. The coating behavior is illustrated by forces from pass 2 to 10 in Table 5-8. Table 5-7 shows the average values of the forces from pass 2 to 10 and also the overall forces for the threading process.

Table 5-7- Average values of forces from pass 2 to 10 and overall 10 passes

Tools & Coatings	Passes (2 to 10)		Overall 10 Passes	
	Fx - Radial	Fy - Tangential	Fx - Radial	Fy - Tangential
Uncoated	-822.67	1146.00	-740.23	1080.00
ALTINOS	-707.67	1129.44	-625.33	967.72
ALTINOS + WCC	-744.22	1147.56	-589.81	851.43
ALTINOS +TiB2	-665.89	1009.89	-595.94	822.44

As can be seen from the table 5-7, the average values of ALTINOS +TiB2 tangential forces after 10 passes have the minimum value. AlTiNOS slightly reduced the overall tangential and the average forces for ALTINOS +WC/C insert are approximately 20% lower than the uncoated one. However, the average value of the forces in pass 2 to 10 shows that the cutting force of the uncoated and AlTiNOS + WCC insert are almost the same. The reduction of force in the average value of 10 passes is due to the excellent tribological performance of this coating during the first machining pass. To be able to investigate the forces in detail, force signals for pass two to ten are being represented in Table 5-8.

Table 5-8- Machining forces from pass 2 to 10

Uncoated	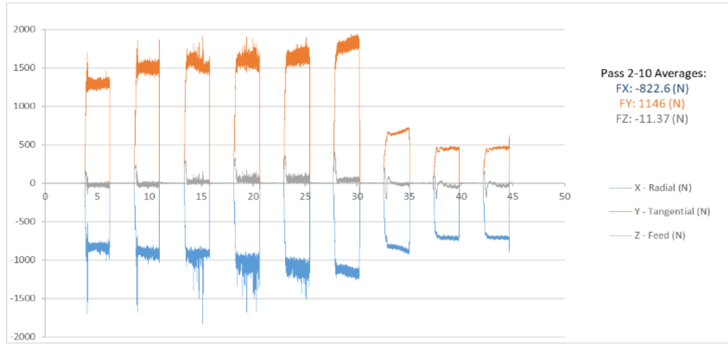
AlTiNOS	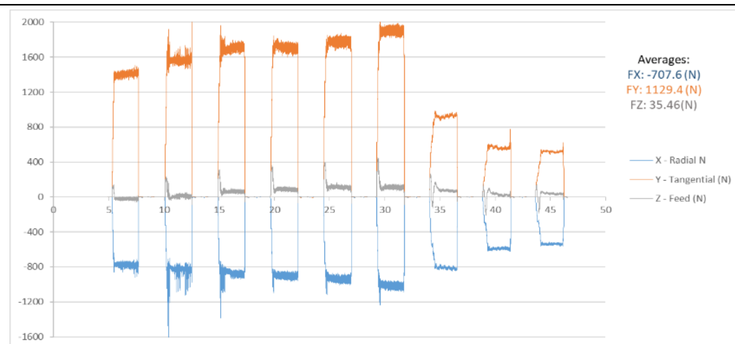
AlTiNOS + WCC	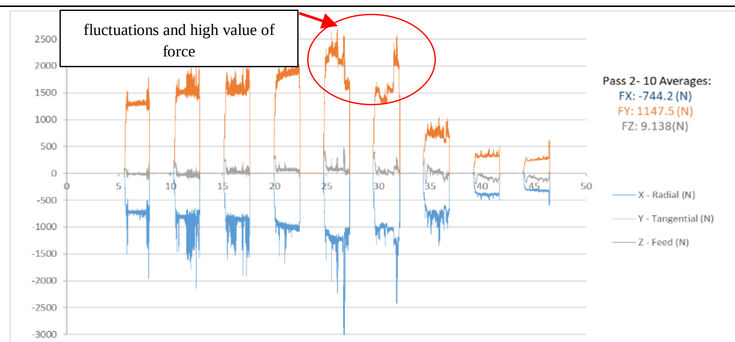
AlTiNOS + TiB2	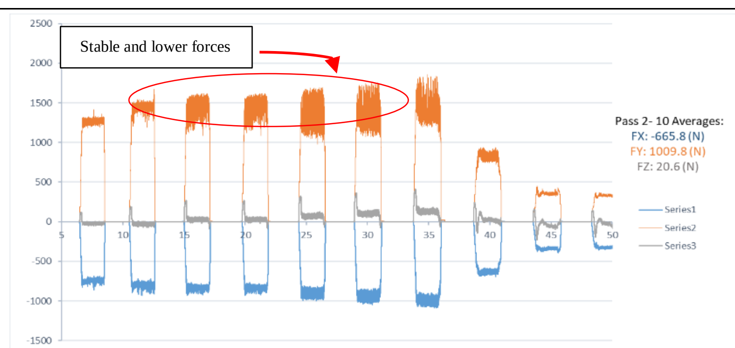

This Figure shows that from the second pass the tangential force for WC/C coating increased until it reached the force of the uncoated insert. From pass 2 to pass 4, the coated insert performed almost the same as the uncoated one. From pass 5 on, the tangential force of AlTiNOS + WCC exceeded the force of the uncoated tool. In pass 6 and 7, the coating force was very unstable exhibiting considerable fluctuation. In conclusion, this coating didn't perform better than the uncoated tool after the second pass and the excellent performance it had in the first pass contributed to the overall reduced 10 pass average of forces. In fact, all of the coating was removed from the surface of the insert after the first pass and caused damage on the surface. This happened because of the low hardness of the WC/C coating and its poor adhesion to the AlTiNOS. Depositing an interlayer between AlTiNOS and WC/C is suggested to increase the adhesion or otherwise use other depositing techniques such as High-power impulse magnetron sputtering (HIPIMS) to obtain a harder, denser and better adhering coating layer.

AlTiNOS+ TiB2 showed lower cutting forces than other inserts for all the passes. This coating has a good combination of hardness, thickness and lubricity. The high hardness of the TiB2 increased its resistance to mechanical wear mechanisms such as abrasion. In addition to that, the formation of TiO_2 oxides caused by the presence of titanium in the coating will mitigate oxidation and diffusion wear on the WC tool. The main reason for the force reduction in the running-in stage and the rest of the test is that B_2O_3 tribo-oxides were formed during machining and because the temperature passed the melting point of the B_2O_3, liquid lubrication occurred. Due to the aforementioned reasons, this coating showed stable and lower forces in Table 5-8. There is a big jump from pass 1 to pass 2 for this coating as well as all other inserts. This can be attributed to the work-hardened layer of the workpiece material which was formed after the first pass.

AlTiNOS also reduced the average forces in all stages of machining, but the reduction was not noticeable. This hard coating contains Aluminum and Titanium. High hardness and good adhesion of the coating to the substrate make this coating a good option to reduce mechanical wear. In addition, the formation of Al_2O_3 and TiO_2 at higher temperatures protect the cutting surface from oxidation and other types of flank wear. However, this coating doesn't possess any lubricity and can't decrease the shear force in the contact zone. As a result, the machining process showed no significant reduction in the cutting forces.

The next step of assessing the tribological performance of the coatings, was to conduct wear analysis and compare the results with the machining forces. Wear analysis was performed for all the inserts on the rake and flank face of the tools. Table 5-9 and Table 5-10 show the tools wear on the flank and rake faces.

Table 5-9- Optical images of Flank wear for all the inserts after 10 passes

Tool	Image (A)	Image (B)
Uncoated	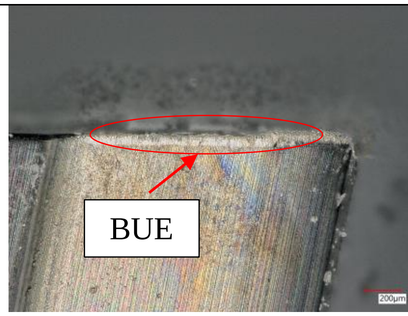	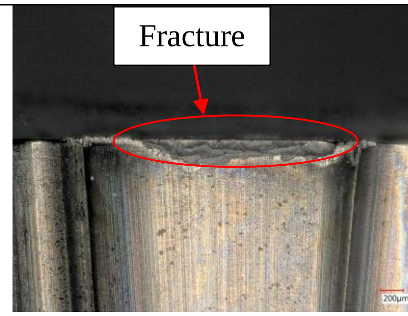
AlTiNOS	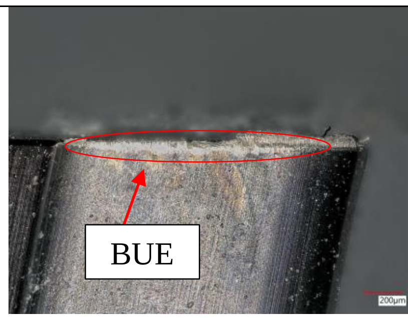	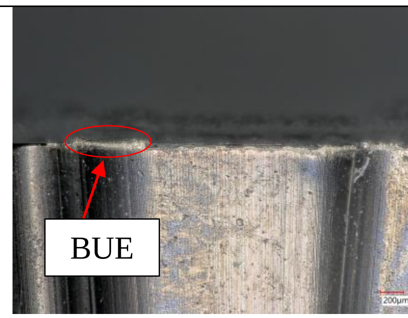
AlTiNOS + WCC	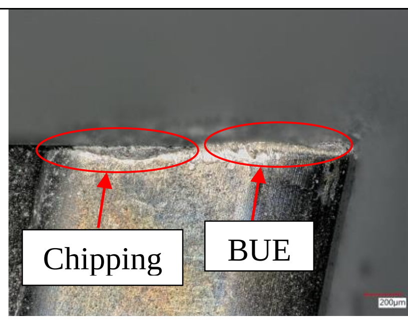	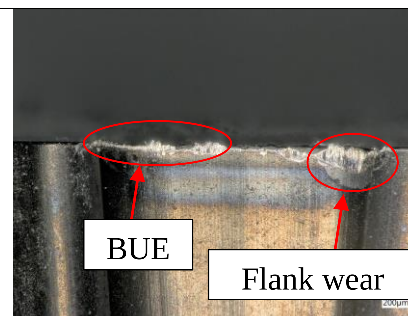
AlTiNOS + TiB2	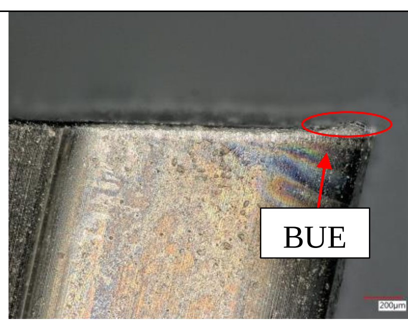	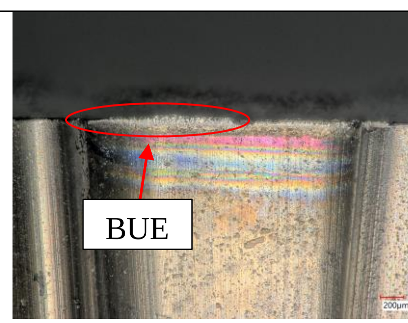

Table 5-10- Optical images of rake wear after 10 passes

<table>
<tr><th>Tool</th><th>Rake Face</th></tr>
<tr><td>Uncoated</td><td>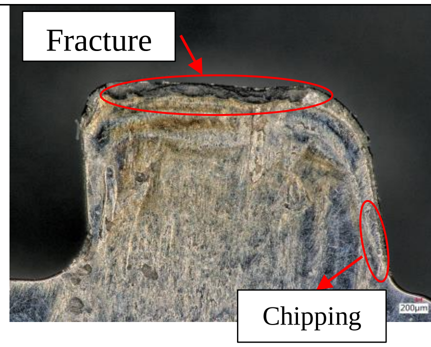
</td></tr>
<tr><td>AlTiNOS</td><td>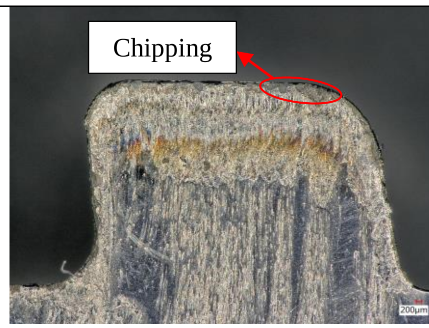
</td></tr>
<tr><td>AlTiNOS+ WCC</td><td>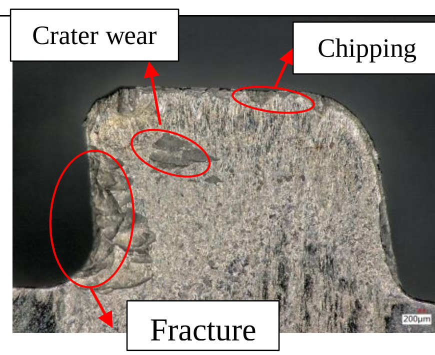
</td></tr>
<tr><td>AlTiNOS+ TiB2</td><td>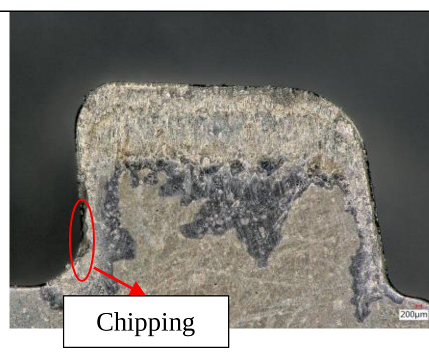
</td></tr>
</table>

As it can be seen in Table 5-9 the uncoated insert has a layer of adhered workpiece material on the flank face. Image B for the uncoated insert shows a relatively big part of tool tip detached under the severe machining condition. The image of the flank face also confirms the fracture wear on the tool tip. Chipping was the other wear mechanism which can be seen on the uncoated insert. SEM and EDS analysis of the tool surface also confirmed all the aforementioned wear mechanisms. Figure 5-8 shows SE image and Map analysis of the tool tip.

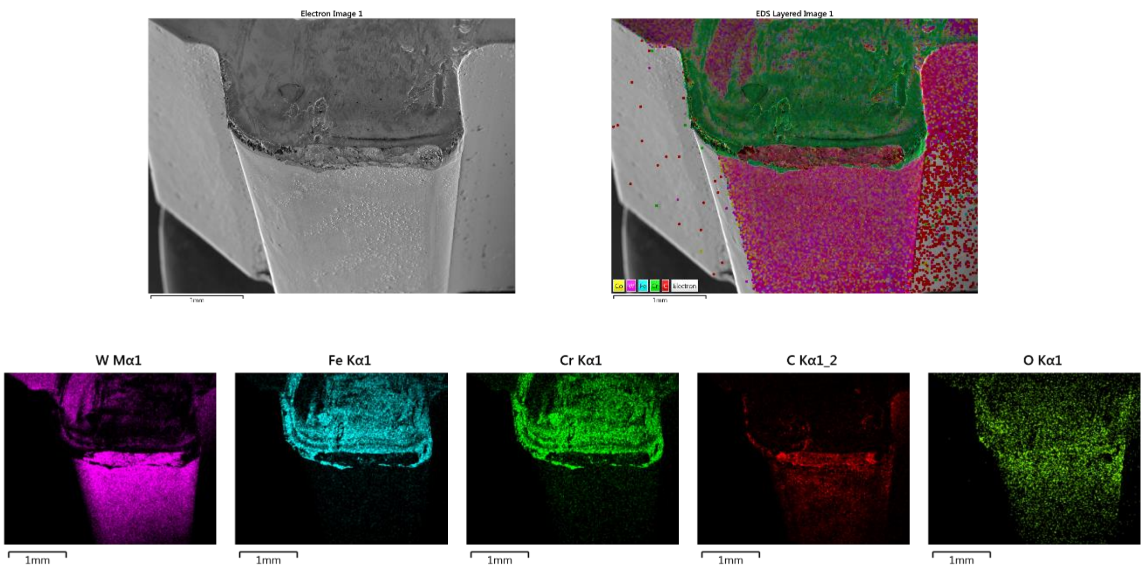

Figure 5-8- SEM image and Map analysis of the uncoated tool.

The adhered layer of Iron (Fe) and Chromium (Cr) from the workpiece material were observed to be all along the surface of the insert. The fractured part of the tip reflects strong signals of Tungsten (W) and there was no adhered layer of steel in the area. All the aforementioned wear mechanisms contribute to the particular fracture on the tool tip caused by the higher cutting forces of the uncoated tool compared to the other coated inserts.

From Table 5-9, the flank face of AlTiNOS showed less build-up edge. There was no fracture area on the tool tip. However, small chipped areas were seen on the rake face. A lower amount of the build-up edge on the surface and less wear were also supported by the machining forces. The cutting forces of this tool after the first pass and after 10 passes were less than the uncoated insert's, which means that the AlTiNOS coating improved the tribological performance of the tool. However, this is a hard coating with low lubricity in the cutting zone. While the forces didn't significantly drop, the tool surface was protected from severe wear mechanisms. Figure 5-9 illustrates the SEM image and EDS Map analysis of the surface of the tool.

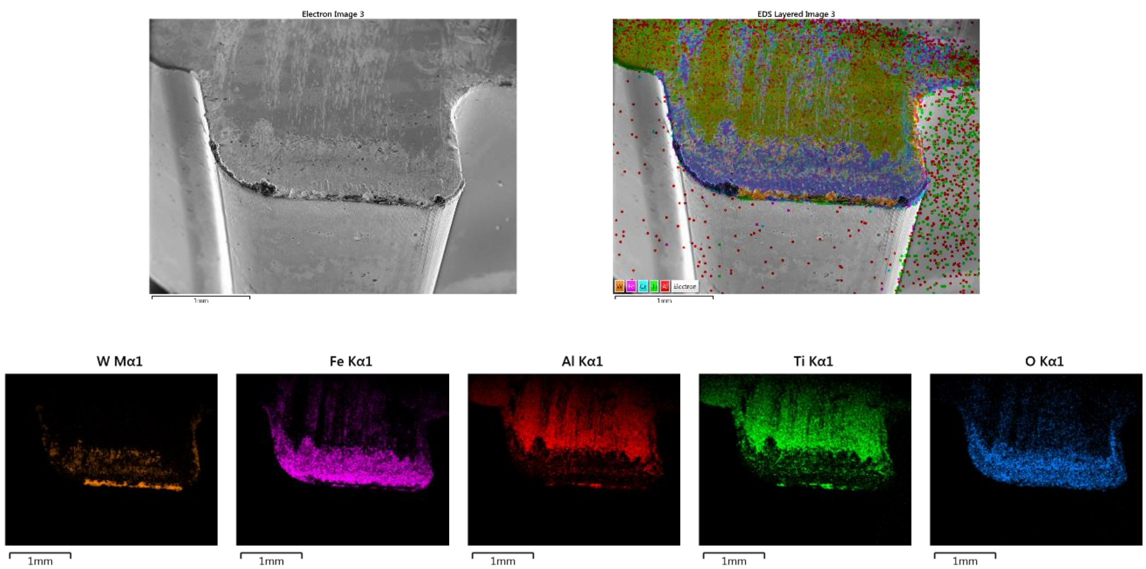

Figure 5-9- SEM image and Map analysis of the AlTiNOS tool.

Map analysis shows that the total length of the adhered workpiece material decreased when compared with the uncoated insert. Aluminum and Titanium of the coating are partially detached from the tool tip. A very small part of the tungsten (W) from the tool became exposed to air and a small amount of chipping can be seen in that area. Generally, the insert experienced fewer severe wear mechanisms like fracture and performed better.

As mentioned earlier in the cutting force section, AlTiNOS + WCC have excellent running-in tribological performance. The forces grew after the second pass and this coating began to show worse performance than the uncoated one. Table 5-9 shows the flank wear of this tool. It can be clearly seen that the amount of BUE increased in the tool in comparison with uncoated and AlTiNOS inserts. In addition, more flank wear, abrasion and chipping can be seen. The image of the rake face in Table 5-10 also demonstrates this coating's inferior performance compared to AlTiNOS. A big fractured area and crater wear can be detected on the surface due to the high temperature on the tool tip. Figure 5-10 shows the SEM image and EDS Map of the AlTiNOS +WCC tool.

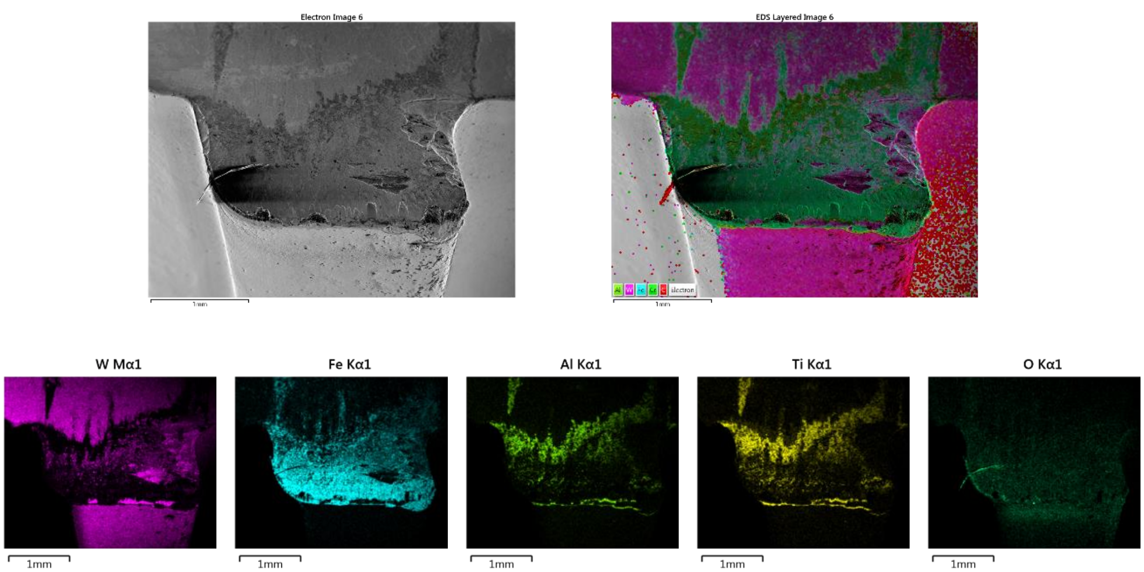

Figure 5-10- SEM image and Map analysis of the AlTiNOS + WCC tool.

The length of the adhered layer of Iron (Fe) was much more than that of the AlTiNOS and was slightly less than the adhered layer of the uncoated insert. In some areas on the tool tip, both AlTiNOS and WC/C layers were removed from the surface. Tungsten (W) from the substrate material became exposed to the air. In some areas on the insert the layer of WC/C coating removed and signals of Aluminum and Titanium can be detected. Since WC/C is a soft coating with high lubricity and low hardness, it can be easily plastically deformed and removed under a harsh machining condition. The cutting forces show that this coating can perform well in the first pass when the forces and temperature are lower. More force was needed after the first pass to deform and cut the layer of work-hardened material forming just below the surface. Also, a high degree of shear in the primary shear zone generated higher temperatures. Therefore, after the second pass, the tool will experience higher forces and temperatures and soft coatings such as WC/C will be easily removed from the insert surface. Delamination of the coating from the surface will cause a more unstable load and as a result, a greater amount of fracture and chipping on the surface. In conclusion, forces and wear images revealed that the coating didn't improve the tribological performance of the tool during the threading process. However, it outperformed all other inserts in the first pass.

Table 5-9 represents the flank wear for AlTiNOS + TiB2. As can be seen, there is no fracture or chipping on the flank face of the tool. The build up edge reduced significantly and there was just a small amount of BUE on the flank face. The rake face of the tool also confirmed the better performance of this coating. Images in Table 5-10 shows a small amount of chipping on the left side of the rake face. Abrasion wear can be seen on the tool face. It seems there was a coating delamination on the surface of the tool so SEM and EDS Map analysis is needed to further investigate the surface.

As can be seen in Figure 5-11 there was a much lower amount of adhered steel on the tool face. TiB2 film was removed from the areas close to the tip, where Aluminum signals can be also noticed. In the areas far from the tip coating, TiB2 coating was present on the surface. However, there still remains a small amount of tungsten exposed to the air.

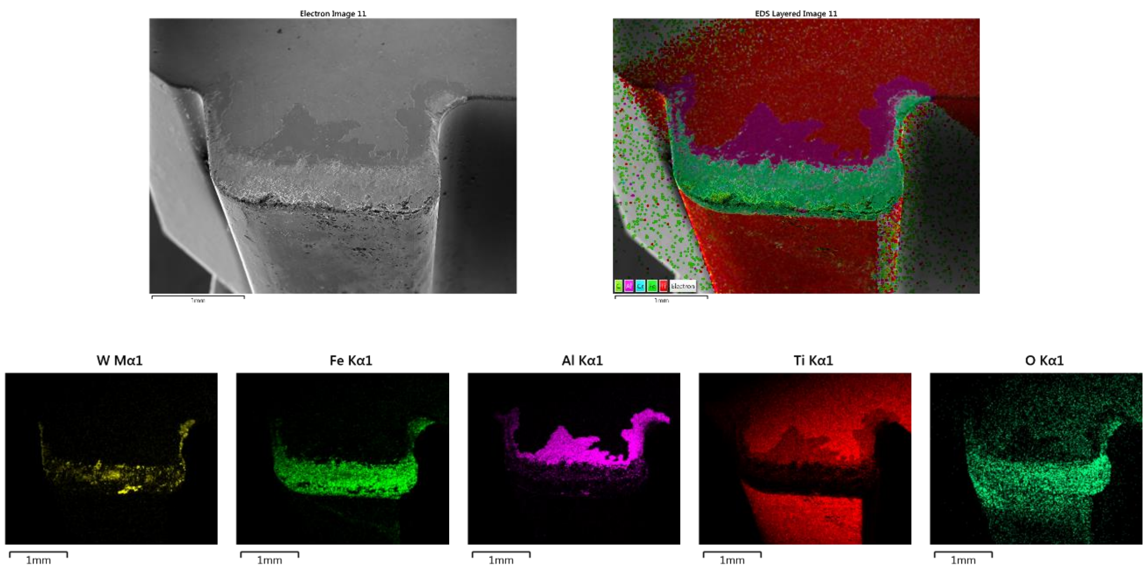

Figure 5-11- SEM image and Map analysis of the AlTiNOS + TiB2 tool.

In conclusion, AlTiNOS + TiB2 had the best performance in all stages of threading. Due to a solid combination of hardness, lubricity and ability to form the liquid B_2O_3 tribo-oxides at high temperatures, this coating can simultaneously reduce the cutting forces and protect the tool face from mechanical and thermal wear.

5.8.4 Chip analysis

The following table presents the chip roughness values for the uncoated and coated inserts.

Table 5-11- Chip roughness from uncoated and coated inserts

Chips from	R_a (μm)	R_q (μm)	R_Z (μm)	Sa (μm)
Uncoated	0.8570	0.999	2.0181	0.7002
AlTiNOS	0.5378	0.7000	1.7278	0.5673
AlTiNOS + TiB2	0.4377	0.5403	1.5935	0.374
AlTiNOS + WC/C	0.3198	0.4290	1.4543	0.3178

It can be seen that AlTiNOS+ WC/C had the minimum value of roughness in the running-in stage. R_a is the roughness of surface measured in a line and Sa is the surface texture measured on the scanned surface. The uncoated tool produced a rougher surface which showed greater friction during the cutting process. Less friction in the case of AlTiNOS + WC/C produced a smoother surface.

To investigate the effect of friction on the chip formation, chip undersurface and the morphology were studied under a SEM. The following are SEM images of the chips.

Table 5-12- SEM images of the chips undersurface

Tool	SEM image of the chip	Chip roughness
Uncoated	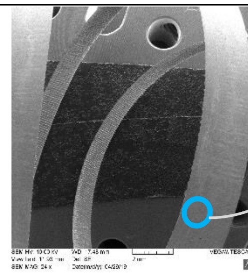	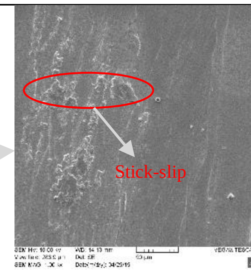
AlTiNOS	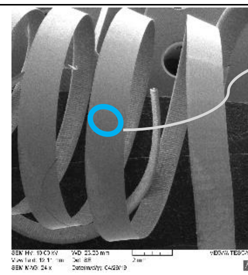	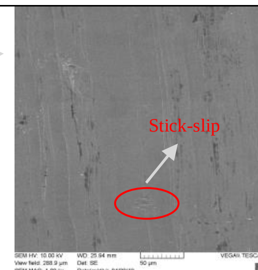
AlTiNOS + TiB2	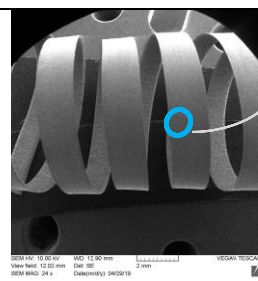	
AlTiNOS + WC/C	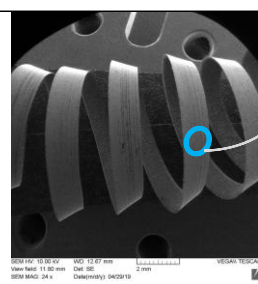	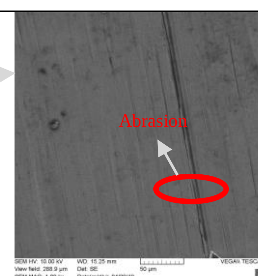

The chip under-surface type and morphology can be a good indication of the friction between the tool and chip. Basically, curlier and smoother chips are generated because of less friction in the contact zone. As it can be seen in Table 5-12, AlTiNOS+WCC had curlier chips and a smoother surface in comparison to AlTiNOS and the uncoated tool. There was no sign of stick-slip on the chip surface. However, the chip characteristics of AlTiNOS+WC/C were very close to the chips from the AlTiNOS+TiB2 tool. Both of them were curly and had a smooth surface. Their tribological behaviour during the running-in stage of machining was also similar, though AlTiNOS+WC/C was slightly better.

A chips cross-section was prepared to measure the chip thickness and the chip thickness ratio. After the chips were mounted and polished, a measurement of their thickness was taken using a Keyence optical microscope. Table 5-13 showed the chip thickness on the chip cross-section. Thickness values were measured with the average values and standard deviations being reported.

Table 5-13-Chips thickness measurement

Chip from the tool	Thickness measurement
Uncoated	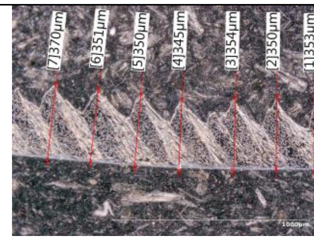
AlTiNOS	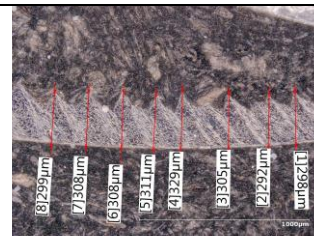
AlTiNOS+TiB2	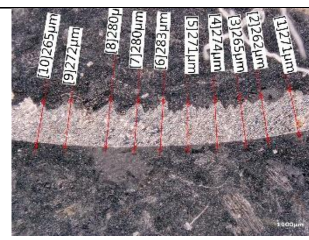
AlTiNOS+WC/C	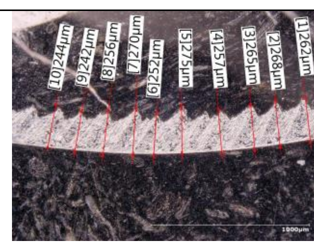

Other chip characteristics were also measured to convey a clear picture of the coatings' performance. Equation (**5-1**) was used to calculate the chip thickness ratio. The shear plane angle, chip velocity and friction between the chips and tools are calculated using equations (5-2), (5-3) and (5-5). All the values are reported in Table 5-14.

Tool	Chip Thickness (mm)	Chip thickness Ratio	Φ - Shear Angle (°)	Chip Velocity (m/min)	Theoretical COF(μ)
Uncaoted	0.3532± 0.0073	0.671	35.367	46.959	0.451
AlTiNOS	0.306±0.0104	0.774	39.580	54.171	0.284
AlTiNOS+ TiB2	0.271±0.0066	0.873	43.272	61.118	0.149
AlTiNOS+WC/C	0.259±0.0104	0.915	44.717	64.029	0.097

Table 5-14- Chip thickness ratio, shear angle, chip velocity and theoretical COF values

From Table 5-14 it can be seen that the chip thickness for the coated tools was lower than the uncoated insert. AlTiNOS+WC/C produced the minimum chip thickness. The lower chip thickness created a larger shear angle, which means that the shear occurred at a smaller shear plane with lower forces and a smaller coefficient of friction. Lower cutting forces from the previous section and lower coefficient of friction values in Table 5-14 confirm this phenomenon.

WC/C is categorized as a soft coating which has lower hardness and elastic modulus in comparison with the other coatings in this study. This coating can easily shear under the cutting condition and decrease the forces and COF in the contact zone. In addition, the formation of a WO2 tribo-oxide can act as a solid lubricant and cause a smoother cutting process [40]. Lower chip surface roughness and curlier chip also support the WC/C coating's better tribological performance compared to the other three inserts. However, this coating is soft and won't be able to tolerate harsh cutting conditions after the running-in stage.

AlTiNOS+TiB2 had a lower chip thickness ratio than the WC/C coating. This coating was harder and more wear resistant. However, the formation of B2O3 liquid tribo-oxides will decrease the shear in the interface and reduce chip thickness and coefficient of friction.

Lower chip roughness and cutting forces show that the Tib2 coating improved the cutting process to a greater degree than the uncoated and AlTiNOS coating. AlTiNOS has lower chip thickness than the uncoated tool. A higher shear angle compared to the uncoated tool, improves cutting. Lower forces and coefficient of friction also confirm that AlTiNOS had better tribological performance than the uncoated insert. It should be mentioned that this is a hard coating with low lubricity. Therefore, the coating can protect the tool surface from different mechanical and thermal wear mechanisms but wais unable to substantially reduce the coefficient of friction significantly.

An uncoated insert with the highest chip thickness resulted in the lowest shear angle. Higher chip thickness means that more plastic deformation occurred in the shear plane which required higher forces, as indicated by higher measured force and coefficient of friction. The SEM image of the chips from the uncoated insert showed a very rough surface with a stick-slip area caused by machining seizure.

In summary, the following conclusion can be mentioned regarding machining tests and analysis:

- First, it should be mentioned that machining results were in good agreement with the tribometer tests. The cutting force and chip analysis of the running-in stage of machining showed that AlTiNOS+ TiB2 had the second best performance after AlTiNOS+WC/C. However, wear resistance of AlTiNOS+TiB2 was far better than AlTiNOS+WC/C after 10 threading passes.
- Although AlTiNOS+WC/C had a lower coefficient of friction and cutting forces, it is not a good candidate for the threading process. Therefore, AlTiNOS+TiB2 with

less lubricity but higher wear resistance is suggested for threading super duplex stainless steel.

6 Conclusion

A Heavy-load high-temperature tribometer was designed to quantify the coefficient of friction during cutting. This bench scale test set up is based on a modified Brinell hardness test. The aim of the test was to avoid plastic flow within the workpiece material while measuring the coefficient of adhesion between the two surfaces under extreme conditions. To avoid seizure, the normal load should be selected in a range where only external friction can happen. The suggested external friction threshold (ζ) ensures that all the tests are performed in the external friction condition. To find the right value for the normal load and avoid seizure, it's suggested to perform three preliminary tests prior to the real test. The selected load should generate a normal stress about two times the yield stress of the disk and not cause shear in the bulk material at the applied temperatures.

A large number of tests with different coatings and workpiece materials were performed to evaluate the tribometer performance. To compare the performance to the published data on the tribometer, uncoated tungsten carbide pins loaded against Ti6Al4V, the effect of the pin tip diameter, heating dwell time and testing order on the reaction torque signal were studied. Results showed that the conditions produced by the pin with a 6 mm pin diameter had the closest results to the benchmark test. The tests also showed that a lower heating dwell time and changes in test order (rotating before heating) did not affect the torque signal and plastic deformation of the bulk material occurring at the high temperature.

In another study, tribometer tests were performed to investigate the effect of coatings deposition parameters and a coatings chemical composition on the measured coefficient of friction. Results showed that coating thickness has no effect on the coefficient of friction. Increasing the substrate bias voltage increases the coefficient of friction and increasing Nitrogen pressure in the chamber will reduce the coefficient of friction. Additionally, pure metal coatings didn't show any wear resistance and were thus removed right after the first test. Using these coatings at high temperatures caused seizure and high computed values of coefficient of friction.

In the last study, three commercial coatings were tested on super duplex stainless steel. A threading process was carried out on super duplex stainless steel tubes to validate the tribometer results. Cutting forces, chip thickness ratio, theoretical coefficient of friction and tool's wear analysis showed that AlTiNOS+ WC/C has a very good tribological performance during the running-in stage. However, lower hardness and elastic modulus of this coating resulted in coating detachment over time. Machining results showed a good agreement between the performance predicted by the tribometer data and performance data collected during the machining tests.

7 Recommendations for future work

The physics and mechanics of the MMRI tribometer were investigated in this study and several different coatings were tested to evaluate the tribometer's performance. However, there remain several areas of interest in need of future clarification. The following is a list of recommendations of how the tribometer could be further improved:

- Pin alignment has significant effects on the COF results and reaction torque signal values. In the current set up, the pin is being aligned using screws in the collet. It's highly suggested to replace the current pin alignment method with a new design which can align the pin more precisely in less time.
- Plastic deformation of the bulk material can easily happen in tests. This occurs in cases where there is a negative gradient of mechanical properties on the surface. This means that material flows in the bulk while the pin and disk are welded on the interface. It's suggested to study the effect of material flow stress at higher temperatures to see how the bulk material flow can be avoided.
- To follow up on the previous suggestion, a new heating system can be developed that can generate heat only on the surface, potentially resolving the bulk material's shear problem. In the resistance heating system, the current passes along with the pin and disk and heats up the bulk material as well as the interface. A heating system which can generate the heat just on the interface would be able to avoid material softening and shear within the bulk material.

- In the current set up, the temperature is being measured at about 1 mm higher than the contact point on the pin. Finding a more precise technique to measure or calculate the temperature right in the interface might prove useful.
- The temperature gradient in the disk cross-section and especially on the contact point can provide valuable information about heat generation and distribution along the workpiece material. Having less heat generated and transferred to the bulk will reduce the shear in bulk material and help to obtain pure external friction during the test.
- A FEM model of the test can be developed to carefully observe the stress distribution and plastic deformation of the workpiece material. The localized coefficient of friction values within the contact zone can be modeled using a FEA model based on the torque and imprint information coming from the tribometer. This information can then be used to improve the design of the tribometer.

8 References

[1] J. M. Paiva *et al.*, “Tribological andWear Performance of Carbide Tools with TiB2 PVD Coating under Varying Machining Conditions of TiAl6V4 Aerospace Alloy,” *Coatings*, vol. 7, p. 187, 2017.

[2] S. Kashem, R. Nagarajah, and M. Ektesabi, *Friction and Wear Methodologies for Design and Control*. 2015.

[3] V. L. Popov, *Contact mechanics and friction*, Second Edi. 2000.

[4] E. Rabinowicz, *Friction and Wear of Materials*. 1965.

[5] M. Shaw, *Metal Cutting Principles*, Second Edi. 2005.

[6] D. T. Frank Philip Bowden, *The friction and lubrication of solids*. Oxford, 1950.

[7] I. V. KRAGELSKY, *Friction and Wear*. London: Butterworths, 1965.

[8] V. D. Kuznetsov, “Mechanism of external friction from the surface energy poin of view,” *Conf. Russ. Phys. Moscow*, p. p.30, 1926.

[9] H. Ernst and M. E. Merchant, “A Basic Factor in the Metal Cutting Process,” in *Friction and Surface Finish*, 1940, p. 76.

[10] K. Holmberg and A. Matthews, *Coatings Tribology*. Amsterdam: ELSEVIER, 1994.

[11] A. p. Green, “Friction between unlubricated metals: a theoretical analysis of the junction model,” *Proceeding R. Soc. A*, vol. 228A, p. 191, 1955.

[12] C. M. Edwards and J. Halling, “An analysis of the plastic interaction of surface asperities and its relevance to the value of the coefficient of friction,” *J. Mech. Eng. Sci.*, vol. 10, no. 2, pp. 101–110, 1968.

[13] P. Heilmann and D. A. Rigney, “An energy-based model of friction and its application to coated systems,” *Wear*, vol. 72, no. 2, pp. 195–217, Oct. 1981.

[14] E. m. Lifshiz, “Dokl. Akad. Nauk SSSR,” p. 90, 1953.

[15] N. Zorev, *Metal cutting mechanics*. New York: Oxford, 1966.

[16] S. N. Melkote *et al.*, “Advances in material and friction data for modelling of metal machining,” *CIRP Ann. - Manuf. Technol.*, vol. 66, no. 2, pp. 731–754, 2017.

[17] E. M. Trent, “Metal Cutting and the Tribology of Seizure:I Seizure in Metal Cutting,” *Wear*, vol. 128, no. 1, pp. 29–45, 1983.

[18] E. M. Trent, “Metal cutting and the tribology of seizure: II movement of work material over the tool in metal cutting,” *Wear*, vol. 128, no. 1, pp. 47–64, 1988.

[19] E. M. Trent, “Metal cutting and the tribology of seizure: III temperatures in metal cutting,” *Wear*, vol. 128, no. 1, pp. 65–81, 1988.

[20] E. M. Trent, “Metal Cutting and the Tribology of Seizure:I Seizure in Metal Cutting,” *Wear*, vol. 128, pp. 29–45, 1983.

[21] S. T. and U. E, “Friction Characteristics on Tool Face in Metal Machining,” *J. Japanese Soc. Precis. Eng.*, vol. 39, pp. 966–972, 1976.

[22] J. Artozoul, C. Lescalier, and D. Dudzinski, “Experimental and analytical combined thermal approach for local tribological understanding in metal cutting,” *Appl. Therm. Eng.*, 2015.

[23] W. Grzesik, “Experimental investigation of the influence of adhesion on the frictional conditions in the cutting process,” *Tribol. Int.*, vol. 32, no. 1, pp. 15–23, 1999.

[24] F. Zhou, “A new analytical tool-chip friction model in dry cutting,” *Int. J. Adv. Manuf. Technol.*, vol. 70, no. 1–4, pp. 309–319, 2014.

[25] M. Olsson, S. Söderberg, S. Jacobson, and S. Hogmark, “Simulation of cutting tool wear by a modified pin-on-disc test,” *Int. J. Mach. Tools Manuf.*, vol. 29, no. 3, pp. 377–390, 1989.

[26] A. D. and P. K. F. Zemzemi1, 2 , W. Bensalem1 , J. Rech2, *,†, “New tribometer designed for the characterisation of the friction properties at the tool/chip/workpiece interfaces in machining,” *Tribotest*, vol. 14, no. January, pp. 147–158, 2008.

[27] C. Claudin, A. Mondelin, J. Rech, and G. Fromentin, “Effects of a straight oil on friction at the tool–workmaterial interface in machining,” *Int. J. Mach. Tools Manuf.*, vol. 50, no. 8, pp. 681–688, Aug. 2010.

[28] A. Biksa, J. Boyd, and S. C. Veldhuis, “Tribological Characterization of Surface Engineered Tooling for Metal Cutting Applications,” pp. 0–5, 2000.

[29] J. Boyd, “Tribometer-Based Quantifying of Friction in Metal Cutting,” *Thesis*, p. 89, 2012.

[30] M. C. Shaw, A. Ber, and P. A. Mamin, “Friction Characteristics of Sliding Surfaces Undergoing Subsurface Plastic Flow,” *J. Basic Eng.*, vol. 82, no. 2, pp. 342–345, 1960.

[31] G. S. Fox-rabinovich, L. S. Shuster, B. D. Beake, and S. C. Veldhuis, “Self-Organization During Friction,” pp. 121–148, 2006.

[32] “ASTM B265: Standard Specification for Titanium and Titanium Alloy Strip,

Sheet, and Plate," *American Society for Testing and Materials (ASTM)*. [Online]. Available: https://compass.astm.org/EDIT/html_annot.cgi?B265+15#s00058.

[33] M. Abdous, "CANRIMT Report," Hamilton, 2019.

[34] G. P. Zhang *et al.*, "Influence of pulsed substrate bias on the structure and properties of Ti-Al-N films deposited by cathodic vacuum arc," *Appl. Surf. Sci.*, vol. 258, no. 19, pp. 7274–7279, 2012.

[35] A. Raveh, M. Weiss, M. Pinkas, D. Z. Rosen, and G. Kimmel, "Graded Al-AlN, TiN, and TiAlN multilayers deposited by radio-frequency reactive magnetron sputtering," *Surf. Coatings Technol.*, vol. 114, no. 2–3, pp. 269–277, 1999.

[36] L. S. Wen, C. Dong, C. Sun, M. D. Huang, Y. P. Lee, and G. Q. Lin, "Preparation of TiN films by arc ion plating using dc and pulsed biases," *J. Vac. Sci. Technol. A Vacuum, Surfaces, Film.*, vol. 22, no. 2, pp. 250–254, 2004.

[37] J. Bujak, J. Walkowicz, and J. Kusiński, "Influence of the nitrogen pressure on the structure and properties of (Ti,Al)N coatings deposited by cathodic vacuum arc PVD process," *Surf. Coatings Technol.*, vol. 180–181, pp. 150–157, 2004.

[38] S. PalDey and S. . Deevi, "Single layer and multilayer wear resistant coatings of (Ti,Al)N: a review," *Mater. Sci. Eng. A*, vol. 342, no. 1–2, pp. 58–79, Feb. 2003.

[39] O. Balzers, "BALIQ INSERT ALTINOS." [Online]. Available: https://www.oerlikon.com/balzers/com/en/portfolio/balzers-surface-solutions/pvd-and-pacvd-based-coatings/baliq/baliq-insert-altinos/.

[40] Mohammad Shariful Islam Chowdhury, "WEAR BEHAVIOUR OF COATED CARBIDE TOOLS DURING MACHINING OF Ti6Al4V AEROSPACE

ALLOY," McMaster University, 2016.

[41] J. Rajaguru and N. Arunachalam, "Coated tool Performance in Dry Turning of Super Duplex Stainless Steel," *Procedia Manuf.*, vol. 10, pp. 601–611, 2017.

[42] Y. Seid Ahmed, J. Paiva Mario, D. Covelli, and S. Clarence Veldhuis, "Investigation of Coated Cutting Tool Performance during Machining of Super Duplex Stainless Steels through 3DWear Evaluations," *Coatings*, vol. 7, p. 127, 2017.

[43] A. Biksa *et al.*, "Wear behavior of adaptive nano-multilayered AlTiN/MexN PVD coatings during machining of aerospace alloys," *Tribol. Int.*, vol. 43, no. 8, pp. 1491–1499, Aug. 2010.

[44] V. Derflinger, H. Brändle, and H. Zimmermann, "New hard/lubricant coating for dry machining," *Surf. Coatings Technol.*, vol. 113, no. 3, pp. 286–292, Mar. 1999.

[45] K. Holmberg and A. Erdemir, "Influence of tribology on global energy consumption, costs and emissions," *Friction*, vol. 5, no. 3, pp. 263–284, 2017.